

DTIC FILE COPY

(2)

AFOSR-ER-89-0730

AD-A208 686

Final Report

ACOUSTOOPTIC PROCESSING OF  
TWO DIMENSIONAL SIGNALS USING  
TEMPORAL AND SPATIAL INTEGRATION

Demetri Psaltis, John Hong, Scott Hudson, Jeff Yu  
Fai Mok, Mark Neifeld, and Nabeel Riza, Dave Brady

AFOSR-ER-89-0730

and is  
90-12

page

California Institute of Technology

CALIFORNIA INSTITUTE OF TECHNOLOGY

DTIC  
SELECTED  
JUN 07 1989  
S D

DISTRIBUTION STATEMENT A  
Approved for public release  
Distribution Unlimited

89 6 06 022

2

Final Report

**ACOUSTOOPTIC PROCESSING OF  
TWO DIMENSIONAL SIGNALS USING  
TEMPORAL AND SPATIAL INTEGRATION**

Demetri Psaltis, John Hong, Scott Hudson, Jeff Yu  
Fai Mok, Mark Neifeld, and Nabeel Riza, Dave Brady

Grant AFOSR-85-0332

Submitted to:  
Dr. Lee Giles  
Air Force Office of Scientific Research  
Bolling Air Force Base  
Washington, DC

Principal Investigator

Demetri Psaltis  
Department of Electrical Engineering  
California Institute of Technology  
Pasadena, CA, 91125

**DTIC**  
**S** ELECTE  
JUN 07 1989  
**D** *CS*

DISTRIBUTION STATEMENT A

Approved for public release;  
Distribution Unlimited

1a. REPORT SECURITY CLASSIFICATION <b>UNCLASSIFIED</b>		1b. RESTRICTIVE MARKINGS		
2a. SECURITY CLASSIFICATION AUTHORITY		3. DISTRIBUTION / AVAILABILITY OF REPORT Approved for public release, distribution unlimited		
2b. DECLASSIFICATION / DOWNGRADING SCHEDULE				
4. PERFORMING ORGANIZATION REPORT NUMBER(S) <del>AFOSR - 85 - 0332</del>		5. MONITORING ORGANIZATION REPORT NUMBER(S) <b>AFOSR-TR- 89 - 0730</b>		
6a. NAME OF PERFORMING ORGANIZATION California Institute of Technology	6b. OFFICE SYMBOL (If applicable)	7a. NAME OF MONITORING ORGANIZATION <b>AFOSR/NE</b>		
6c. ADDRESS (City, State, and ZIP Code) Dept. of Electrical Engineering MS116-81 Pasadena, CA 91125		7b. ADDRESS (City, State, and ZIP Code) <b>Bldg. 410</b> <b>POLLING AFB, DC 20332</b>		
8a. NAME OF FUNDING / SPONSORING ORGANIZATION <b>AFOSR</b>	8b. OFFICE SYMBOL (If applicable) <b>NE</b>	9. PROCUREMENT INSTRUMENT IDENTIFICATION NUMBER <b>AFOSR-85-0332</b>		
8c. ADDRESS (City, State, and ZIP Code) <b>SAME AS 7b</b>		10. SOURCE OF FUNDING NUMBERS		
		PROGRAM ELEMENT NO. <b>161102F</b>	PROJECT NO. <b>2305</b>	
		TASK NO. <b>61</b>	WORK UNIT ACCESSION NO.	
11. TITLE (Include Security Classification)				
12. PERSONAL AUTHOR(S) <b>Demetri Psaltis</b>				
13a. TYPE OF REPORT <b>Final</b>	13b. TIME COVERED FROM <b>01 MAY 88</b> TO <b>28 FEB 89</b>	14. DATE OF REPORT (Year, Month, Day) <b>5/12/89</b>	15. PAGE COUNT <b>120</b>	
16. SUPPLEMENTARY NOTATION				
17. COSATI CODES		18. SUBJECT TERMS (Continue on reverse if necessary and identify by block number)		
FIELD	GROUP			SUB-GROUP
19. ABSTRACT (Continue on reverse if necessary and identify by block number)				
<p>Acoustoptic signal processing architectures and methods are developed for a variety of 2-D problems. A formulation of the universe synthetic aperture radar problem as an energy minimization procedure is reported. Acoustoptic systems for multiple target detection and 2-D spectrum analysis are experimentally demonstrated. The application of acoustoptics to the adaptive beam-forming for broadband antenna arrays is described.</p>				
20. DISTRIBUTION / AVAILABILITY OF ABSTRACT <input checked="" type="checkbox"/> UNCLASSIFIED/UNLIMITED <input type="checkbox"/> SAME AS RPT. <input type="checkbox"/> DTIC USERS		21. ABSTRACT SECURITY CLASSIFICATION <b>UNCLASSIFIED</b>		
22a. NAME OF RESPONSIBLE INDIVIDUAL <b>CELES</b>		22b. TELEPHONE (Include Area Code) <b>(202) 767-4431</b>	22c. OFFICE SYMBOL <b>NE</b>	

# TABLE OF CONTENTS

<b>I</b>	<b>INTRODUCTION</b>	1
<b>II</b>	<b>ISAR IMAGING</b>	3
II.0	Introduction	3
II.1	SAR Imaging Fundamentals	3
II.2	Two-Dimensional Imaging	4
II.3	State Space Statistics	6
II.4	Energy Functions	8
II.5	Simulation Results	9
II.6	Optical Processing	9
<b>III</b>	<b>LED BIPOLAR CORRELATOR</b>	15
III.0	Introduction	15
III.1	Bipolar Correlators	15
III.2	Bipolar Rotation Invariant Filters	16
III.3	Generalized Bipolar Filters	17
III.4	Optical System Implementation	20
III.5	Correlation Results	21
III.6	Bias Considerations	21
III.7	Implementation of a Linear Discriminant Function	22
III.8	Conclusion	22
<b>V</b>	<b>MULTIPLICATIVE TIME AND SPACE INTEGRATING ACOUSTOOPTIC SPECTRUM ANALYZER</b>	38
IV	Introduction	38
IV	Principles of TSI Processing	38

Accession For	
NTIS GRA&I	<input checked="" type="checkbox"/>
DTIC TAB	<input type="checkbox"/>
Unannounced	<input type="checkbox"/>
Justification	
By	
Distribution	
Availability Codes	
Dist	Avail and/or Special
A-1	



IV	Space Integrating Spectrum Analyzer	39
IV	Time Integrating Spectrum Analyzer Experiment	41
IV	Architectures for TSI Spectrum Analysis	42
IV	Bias Removal Techniques	44
IV	Processor Performance Issues	45
<b>V</b>	<b>ADAPTIVE BROADBAND ARRAY PROCESSING</b>	<b>58</b>
V	Introduction	58
V	Narrowband Processors in Broadband Environments	58
V	Optimum Broadband Systems	64
V	Directional Cancellation of a Single Broadband Interference	66
V	Adaptive Array Processor	68
V	Optical Implementation	71
V	Adaptive Array Processor with Variable Look Direction	77
<b>VI</b>	<b>INVERSE SYNTHETIC APERTURE RADAR : IMAGING METHOD AND OPTICAL IMPLEMENTATION</b>	<b>87</b>
VI	Introduction	87
VI	Fundamentals of Radar Imaging	87
VI	Motion Compensation	88
VI	ISAR Imaging in Two Dimensions	89
VI	Effects of Neglecting Aspect Compensation	91
VI	Learning Aspect Compensation	92
VI	Optical Implementation	94
<b>VII</b>	<b>CAPACITY OF OPTICAL CORRELATORS</b>	<b>98</b>
VII	Introduction	98
VII	Capacity of Linear Filters	98

VII	Capacity of Shift Invariant Filters	99
VII	Capacity of Binary Filters	101
VII	Capacity of the Volume VanderLugt Correlator	101
VII	Conclusion	103

## **VIII PHOTOREFRACTIVE INTEGRATED OPTICAL**

	<b>VECTOR MATRIX MULTIPLIER</b>	110
VIII	Introduction	110
VIII	Matrix Implementation via Integrated Volume Holograms	110
VIII	Recording the Matrix	113
VIII	Experimental Results and Discussion	115
VIII	Conclusion	116

## I INTRODUCTION

The goal of this project is the development of optical signal processing architectures and techniques that are suitable for processing information in two dimensions. We have applied our methods to synthetic aperture radar (SAR), image recognition, two dimensional spectrum analysis of one dimensional signals and adaptive phased arrays. In previous years we have developed several specific acoustooptic architectures for each application area and we have experimentally demonstrated at least one architecture in each category. In this report we describe our recent results in the areas of radar imaging, two dimensional spectrum analysis of one dimensional signals, adaptive phased arrays, image correlation, and integrated optical signal processing.

In the field of radar imaging we have begun to investigate methods for performing inverse synthetic aperture radar (ISAR) imaging. In normal synthetic aperture radar, radar platform motion is used to create a long synthetic aperture that allows high azimuth resolution to be achieved. If there is any target motion during the synthesizing of the aperture the resulting image will be degraded. Consequently SAR imaging is only applicable to stationary targets. ISAR, however, exploits target motion to create a synthetic aperture without the need for radar platform motion. Unfortunately the data recorded by the synthetic aperture is determined not only by the nature of the target but also by the target's motion. The effects of the target's motion on the recorded data must be compensated for if a faithful image of the target is to be produced. Currently ISAR imaging techniques make restrictive assumptions about the target's motion. We have developed an iterative approach which is applicable to more general kinds of target motion than current techniques. We discuss our approach to ISAR imaging in sections II and VI.

We have completed the experimental demonstration of the programmable acoustooptic image correlator. In this system an input image is detected by a TV camera and applied to the optical system as a video signal through an acoustooptic device. The reference is stored in a digital memory and entered into the system through a one dimensional array of LEDs. In section III we show that if the reference is stored with only one bit of accuracy, the the performance degrades only marginally. The capacity of the correlator is reduced by a factor of only  $\pi/2$ . In addition the traditional training algorithms that exist for programming the correlator can be readily modified to accommodate the binary format of the reference. In section III we present a binary version of the perceptron algorithm. the significance of the above results is that the design of the electronic portion of the optical correlator is simplified drastically. The experimental demonstration of the acoustooptic correlator performing multiple targ

Two different acoustooptic architectures for performing two dimensional spectrum analysis were demonstrated. The first is a Mach-Zender interferometer with two orthogonally oriented acoustooptic devices in each of its arms. The two arms of the interferometer interfere on a two dimensional CCD where the 2-D Fourier transform accumulates through temporal integration. The description of the system and its experimental demonstration

has been published as a paper (reference 2 in section IV). The second architecture is a multiplicative one. This architecture is described in section IV and it is more insensitive to mechanical vibrations than the interferometric approach. The interferometer however has its own advantageous features which are better light efficiency and simpler demodulation requirements at the output to separate the signal from the bias terms.

Section V reports our progress in the area of adaptive filters. In previous years we have demonstrated single channel acoustooptic filters that utilized a combination of temporal and spatial integration. This year we concentrated on broadband phased arrays. In this case jammers may be present anywhere within a bandwidth as high as one gigahertz. The adaptive processor must then place nulls in both the temporal frequency domain and the direction of arrival of the jammer to effectively cancel the interference. Again this is a problem that is extremely demanding computationally and analog optics provides a uniquely effective solution.

VanderLugt correlators have been used for a long time for optical pattern recognition. Recently there has been a great deal of interest in using VanderLugt correlators in pattern classification systems. These systems determine whether an input image is a member of one of two classes, with each class being composed of many images. Typically a reference filter is formed from a linear combination of these images. When an image is input to this filter the presence or absence of a correlation peak determines which of the two classes the image belongs to. The capacity of a correlator is the maximum number of images that can be stored in the reference filter without the system misclassifying an image. In section VII we examine the capacity of VanderLugt correlators using both planar and volume optical recording media. In addition we examine the capacity when the filter is binarized.

Vector-matrix multipliers are fundamental components of many signal processing systems such as neural networks and any system which must perform general linear transformations. Implementing vector-matrix multipliers with bulk optics has proven quite successful, especially where computational speed and low power consumption are of prime importance. Despite this success integrated optical implementations offer certain advantages over bulk systems such as smaller size, lighter weight, and ease of mass fabrication. Additionally integrated optical vector-matrix multipliers are planar devices which allow use of the third dimension for optical programming of the matrix. In section VIII we present an architecture for an integrated optical vector matrix multiplier using a photorefractive medium for the matrix. We also discuss techniques for writing the matrix using unguided light from out of the plane of the device.



## II ISAR IMAGING

### II.0 Introduction

The theory and technology of producing synthetic aperture radar images of stationary targets from moving platforms have been well developed and utilized<sup>1</sup>. As SAR imaging requires precise knowledge of the relative motion between radar and target it is not possible to directly produce SAR images of targets which themselves move beyond the control of the imaging system. Inverse synthetic aperture radar (ISAR) is an attempt to overcome this difficulty<sup>2,3</sup>.

### II.1 SAR Imaging Fundamentals

Consider a three-dimensional rigid target whose reflectivity at any point in space is given, in a coordinate system fixed on the target, by  $f(\vec{r})$  (That  $f(\vec{r})$  does not depend on time is a statement of the constraint that the target is a rigid body). Any relative motion between this target and an imaging radar will be described as seen in the target's coordinate system; that is the radar moves along a trajectory,  $\vec{R}(t)$ , while the target remains fixed. It will be assumed that the change in  $\vec{R}(t)$  over the duration of a single pulse can be neglected

If the radar transmits a pure tone,  $g(t) = e^{j2\pi\nu_0 t}$ , and the target consists of a small volume  $d^3r$  centered on  $\vec{r}$  with reflectivity  $f(\vec{r})$  the received signal will be given by

$$s(t) = d^3r f(\vec{r}) e^{j2\pi\nu_0(t - 2|\vec{r} - \vec{R}|/c)}.$$

If the target consists of a collection of such volumes, and if multiple reflections and shadowing effects are neglected, then the received signal will be given by

$$s(t) = \int d^3r f(\vec{r}) e^{j2\pi\nu_0(t - 2|\vec{r} - \vec{R}|/c)}.$$

If  $R \gg r$  then the far-field approximation gives  $|\vec{r} - \vec{R}| \approx R - \vec{e}_R \cdot \vec{r}$  where  $\vec{e}_R$  is the unit vector in the  $\vec{R}$  direction. Consequently the received signal is given by

$$\begin{aligned} s(t) &= e^{j2\pi\nu_0(t - 2R/c)} \int d^3r f(\vec{r}) e^{j2\pi[\frac{2\nu_0}{c} \vec{e}_R \cdot \vec{r}]} \\ &= e^{j2\pi\nu_0(t - 2R/c)} F\left(\frac{2\nu_0}{c} \vec{e}_R\right). \end{aligned}$$

In other words the radar receives the (spatial) Fourier transform of the object, at spatial frequency  $\frac{2\nu_0}{c} = \frac{2}{\lambda}$  along the ray in Fourier space defined by  $\vec{e}_R$ , on a temporal carrier.

If the radar instead transmits a signal with a finite bandwidth,

$$g(t) = \int_{-B/2}^{B/2} d\nu G(\nu) e^{j2\pi(\nu + \nu_0)t},$$

it follows that the received signal will be given by

$$s(t) = e^{j2\pi\nu_0(t-2R/c)} \int_{-B/2}^{B/2} d\nu [G(\nu) e^{-j2\pi\nu 2R/c} F(\frac{2(\nu + \nu_0)}{c} \vec{e}_R)] e^{j2\pi\nu t}.$$

Mixing  $s(t)$  with  $e^{-j2\pi\nu_0(t-2R/c)}$ , Fourier transforming and multiplying the result by

$$H(\nu) = \begin{cases} \frac{G(\nu)}{|G(\nu)|^2} e^{j2\pi\nu 2R/c}, & -B/2 \leq \nu \leq B/2; \\ 0, & \text{otherwise} \end{cases}$$

will produce

$$W(\nu) = F(\frac{2(\nu + \nu_0)}{c} \vec{e}_R) \text{rect}(\frac{\nu}{B}).$$

If the radar does this for  $N$  different rays,  $\vec{e}_R^k$ ,  $0 \leq k \leq N-1$ , it will produce samples of the target's Fourier transform over some volume of Fourier space. These can then be inverse transformed producing the function  $f(\vec{r})$  to within the resolution permitted by the finite size of the volume. This is the basic principle of synthetic aperture radar.

## II.2 Two-Dimensional Imaging

The special case of a two-dimensional geometry is considered in this paper because 1) It has important practical applications; almost all work in the literature deals with this case, and 2) it greatly reduces the complexity of the problem for analysis and computer simulation, yet the results readily generalize to three-dimensions. For a two-dimensional geometry  $\vec{e}_R^k = [\cos \theta_k, \sin \theta_k]$ . Consequently a two-dimensional target,  $f(x, y)$ , gives rise to a sequence of  $N$  Fourier samples described by

$$\begin{aligned} & F(\frac{2(\nu + \nu_0)}{c} [\cos \theta_k, \sin \theta_k]) \text{rect}(\nu/B) \\ &= \text{rect}(\nu/B) \int dx \int dy f(x, y) e^{j2\pi \frac{2(\nu + \nu_0)}{c} (x \cos \theta_k + y \sin \theta_k)}, \quad 0 \leq k \leq N-1. \end{aligned}$$

A very important class of problems results when the small angle conditions,

$$\cos \theta_k \approx 1, \quad \sin \theta_k \approx \theta_k, \quad (\frac{2\nu}{c} y \theta)_{\max} = B y_{\max} \theta_{\max} / c \ll 1$$

hold. Then the Fourier samples "decouple" into a cascade of one dimensional transforms

$$F(\frac{2(\nu + \nu_0)}{c} [1, \theta_k]) = \int dy e^{j2\pi \frac{2\nu_0}{c} y \theta_k} \int dx \text{rect}(\nu/B) e^{j2\pi \frac{2(\nu + \nu_0)}{c} x} f(x, y), \quad 0 \leq k \leq N-1.$$

Resolution in  $x$  is achieved via "range compression" —

$$\int_{-B/2}^{B/2} d\nu e^{-j2\pi \frac{2(\nu+\nu_0)}{c} x} \int d\xi e^{j2\pi \frac{2(\nu+\nu_0)}{c} \xi} f(\xi, y) = f(x, y) * B \operatorname{sinc}\left(\frac{x}{c/2B}\right).$$

What is left are the samples

$$F_k(x) = \int dy e^{j2\pi \frac{2\nu_0}{c} y \theta_k} f(x, y) * B \operatorname{sinc}\left(\frac{x}{c/2B}\right).$$

The quantity  $c/2B = \Delta x$ , the  $x$  resolution, defines the width of a "range bin". The rest of the discussion will center on achieving  $y$  resolution within any given range bin (fixed  $x$ ). For clarity, therefore, explicit dependence on  $x$  will no longer be shown.

Resolution in  $y$  is thus achieved by inverting

$$F_k = \int dy f(y) e^{j \frac{2\pi}{\lambda/2} y \theta_k}, \quad 0 \leq k \leq N-1,$$

which is done by simply inverse transforming via

$$\hat{f}(y) = \frac{1}{N} \sum_k F_k e^{-j \frac{2\pi}{\lambda/2} y \theta_k} \quad (11.2.1)$$

$$\int d\eta f(\eta) \left[ \frac{1}{N} \sum_k e^{j \frac{2\pi}{\lambda/2} (\eta - y) \theta_k} \right].$$

If the problem is well posed (if it is at all possible to form an image) then the quantity in brackets will be a sinc-like function with some main lobe width  $\Delta y$ . Since the actual function depends on the  $\theta_k$  in a very complicated way, the following approximation will be employed

$$\frac{1}{N} \sum_k e^{j \frac{2\pi}{\lambda/2} (\eta - y) \theta_k} \approx \delta(\eta - y). \quad (11.2.2)$$

It should always be remembered that this is a "delta" function only on a scale larger than  $\Delta y$  (it really has a finite width). In view of (11.2.2) it follows that to within the finite resolution  $\Delta y$ ,  $\hat{f}(y) \approx f(y)$ .

Notice the implicit assumption that  $R$  for each pulse —  $R_k$  — (needed for mixing and filtering) and the  $\theta_k$  are known. This is the case in SAR imaging. For ISAR imaging, however, the trajectory is unknown a priori. What one has instead are estimates —  $\hat{R}_k, \hat{\theta}_k$ . Since radar is a range measuring device, accurate "gross-range" estimates,  $\hat{R}_k$ , are much more straight forward to obtain than are the "aspect" angles,  $\hat{\theta}_k$ , through techniques such as point-target referencing or echo correlating. Therefore discussion below is confined to estimating the aspect angles.

The  $N$  aspect angle estimates,  $\hat{\vec{\theta}} = (\hat{\theta}_0, \dots, \hat{\theta}_{N-1})$ , define an  $N$  dimensional state space. With each point in state space is associated an image —

$$\hat{f}(y; \hat{\vec{\theta}}) = \int d\eta f(\eta) \left[ \frac{1}{N} \sum_k e^{j \frac{2\pi}{\lambda/2} (\eta \hat{\theta}_k - y \hat{\theta}_k)} \right] = \int d\eta f(\eta) h(y, \eta; \hat{\vec{\theta}}).$$

For  $\hat{\vec{\theta}} \neq \vec{\theta}$ ,  $h$  is in general not a “delta” function, and consequently  $\hat{f}(y) \neq f(y)$ . In its most general form, then, the ISAR problem is to search state space for the point corresponding to the “true” image. (Notice that, because of the small angle assumptions,  $h$  has a form which is invariant under  $y \rightarrow y/a, \hat{\vec{\theta}} \rightarrow a\hat{\vec{\theta}}$ . Consequently all images associated with a given ray in state space are scaled (in  $y$  only) versions of a single image. This fact is what makes ISAR as it is currently described in the literature<sup>2,3</sup> possible. One merely assumes that  $\theta_k \propto k$ ; the actual constant of proportionality is not needed. Hence there is no need for parameter estimation and the problem reduces to an inverse Fourier transform. However this approach only works for trajectories consistent with this assumption.)

### II.3 State Space Statistics

Assume the range bin consists of  $N$  point-targets located at positions  $y_n = n\Delta y$ , i.e.

$$f(y) = \sum_{n=0}^{N-1} f_n e^{j\psi_n} \delta(y - n\Delta y) \quad (II.3.1)$$

where  $f$  and  $\psi$  are the magnitude and phase of the reflectance. Then the returns are given by

$$F_k = \sum_m f_m e^{j \frac{2\pi}{\lambda/2} m \Delta y \theta_k} e^{j\psi_m} = \sum_m f_m e^{j\psi_m} e^{jm\phi_k}$$

where  $\phi_k = \frac{2\pi \Delta y}{\lambda/2} \theta_k$ . If the target is reconstructed using trajectory estimates  $\hat{\phi}_k = \phi_k + \epsilon_k$  then the image pixels are given by

$$\hat{f}_n = \frac{1}{N} \sum_m f_m e^{j\psi_m} \sum_k e^{j(m\phi_k - n\hat{\phi}_k)} = \frac{1}{N} \sum_m f_m e^{j\psi_m} \sum_k e^{j(m-n)\phi_k} e^{-jn\epsilon_k}$$

and hence

$$|\hat{f}_n|^2 = \frac{1}{N^2} \sum_m \sum_p f_m f_p e^{j(\psi_m - \psi_p)} \sum_k \sum_l e^{j(m-n)\phi_k} e^{-j(p-n)\phi_l} e^{-jn(\epsilon_k - \epsilon_l)}.$$

If the  $\epsilon_k$  are treated as independent, identically distributed, random variables with density  $p(\epsilon)$  then the expected value of  $|\hat{f}_n|^2$  can be computed as

$$E[|\hat{f}_n|^2] = \frac{1}{N^2} \sum_m \sum_p f_m f_p e^{j(\psi_m - \psi_p)} \sum_k \sum_l e^{j(m-n)\phi_k} e^{-j(p-n)\phi_l} E[e^{-jn(\epsilon_k - \epsilon_l)}]. \quad (II.3.2)$$

The expected value of the random term is

$$E[e^{-jn(\epsilon_k - \epsilon_l)}] = \begin{cases} |\int d\epsilon p(\epsilon) e^{-jn\epsilon}|^2 = |P(n)|^2, & \text{if } k \neq l \\ 1, & \text{if } k = l \end{cases}$$

or more compactly

$$E[e^{-jn(\epsilon_k - \epsilon_l)}] = |P(n)|^2 + \delta_{kl}(1 - |P(n)|^2). \quad (4)$$

Substituting (4) into (II.3.2) it follows that

$$\begin{aligned} E[|\hat{f}_n|^2] &= \frac{|P(n)|^2}{N^2} \sum_m \sum_p f_n f_p e^{j(\psi_m - \psi_p)} \sum_k \sum_l e^{j(m-n)\phi_k} e^{-j(p-n)\phi_l} \\ &\quad + \frac{(1 - |P(n)|^2)}{N^2} \sum_m \sum_p e^{j(\psi_m - \psi_p)} \sum_k e^{j(m-p)\phi_k} \end{aligned} \quad (II.3.4)$$

By (II.2.2),

$$\sum_k e^{j(m-p)\phi_k} \approx N\delta_{mp} \Rightarrow \sum_k \sum_l e^{j(m-n)\phi_k} e^{j(p-n)\phi_l} \approx N^2 \delta_{mn} \delta_{pn}.$$

Using this in equation (II.3.4) gives the final result —

$$E[|\hat{f}_n|^2] = f_n^2 |P(n)|^2 + \frac{(1 - |P(n)|^2)}{N} \sum_m f_m^2. \quad (II.3.5)$$

Equation (II.3.5) says two things — errors in the trajectory estimate: 1) degrade the image pixels from an intensity of  $f_n^2$  to  $f_n^2 |P(n)|^2$  (the first term), and 2) give rise to a noise floor (the second term). As an example let

$$p(\epsilon) = \frac{1}{\sqrt{2\pi}\sigma} e^{-\frac{1}{2}(\frac{\epsilon}{\sigma})^2},$$

then

$$P(n) = e^{-\frac{1}{2}(n\sigma)^2}$$

and (II.3.5) becomes

$$E[|\hat{f}_n|^2] = f_n^2 e^{-(n\sigma)^2} + \frac{1 - e^{-(n\sigma)^2}}{N} \sum_m f_m^2. \quad (II.3.5a)$$

The pixels farthest from the  $y = 0$  axis ( $n$  large) have on average both a higher noise level and a lower reconstruction intensity. Thus the image deteriorates from the extremities

inward. This is as expected since a small error in aspect angle causes a phase error which grows proportional to  $y$ . To make this statement quantitative a signal to noise ratio can be defined as the ratio of the first term in (II.3.5) to the second —

$$SNR(n) = \frac{f_n^2}{E_{av}} \frac{|P(n)|^2}{1 - |P(n)|^2} \quad (II.3.6)$$

where

$$E_{av} = \frac{1}{N} \sum_m f_m^2.$$

For the  $p(\epsilon)$  used in the above example (II.3.6) becomes

$$SNR(n) = \frac{f_n^2}{E_{av}} \frac{1}{e^{(n\sigma)^2} - 1} \quad (II.3.6a)$$

which clearly displays the pixel deterioration relative to the noise floor with increasing  $n$ . Figures II.1 and II.2 show computer simulation verification of (II.3.5a) with  $N = 16$ ,  $\sigma = 0.5$ , for a range bin with point-targets at pixels 0 and 7.

#### II.4 Energy Functions

ISAR imaging can be treated as an optimization problem with respect to the state space parameters  $\hat{\phi}_k$ . The central task then becomes the formulation of an "energy" function describing the quality of the reconstruction. Without some a priori assumptions about the nature of the image to be reconstructed it is impossible to say whether a given reconstruction is "good" or "bad" since all images are equally likely. Thus image reconstruction schemes generally contain a substantial amount of a priori assumptions as to the form of the original image. The more specific the assumptions the more discerning an energy function that can be constructed.

Our research has so far concentrated on energy functions for an important class of targets namely binary-random-phase targets. These targets have the property that  $f_n$  is 0 or 1 while  $\psi_n$  is arbitrary. Such a target model should be well suited to ISAR imaging of aircraft in flight and ships at sea since such targets consist of a nearly uniform, highly reflective object (metal) against a poorly reflective background (air or water). It can then be stated a priori that a good reconstruction will have  $|\hat{f}_n|^2$  very nearly 1 or 0 with no other values allowed. An energy function making use of this knowledge is

$$E = \frac{1}{N} \sum_{n=0}^{N-1} E_n \quad \text{where} \quad E_n = \begin{cases} \left( \frac{1 - |\hat{f}_n|^2}{1 - \alpha} \right)^p, & \text{if } |\hat{f}_n|^2 > \alpha; \\ \left( \frac{|\hat{f}_n|^2}{\alpha} \right)^p, & \text{if } |\hat{f}_n|^2 \leq \alpha \end{cases} \quad (II.4.1)$$

where  $\alpha$  and  $p$  are constants to be chosen. Clearly  $E$  is non-negative and assumes its global minimum value of 0 when the binary image is faithfully reconstructed.  $E$  assumes

the value 1 when all pixel energies assume the value  $\alpha$ . The normalization factors in the denominators insure that  $E$  is continuous as  $|\hat{f}_n|^2$  moves across the threshold.

Using (II.3.5a), choosing  $\alpha$  to be  $E_{av}$ , and then substituting into (II.4.1) gives  $E_n = (1 - e^{-(n\sigma)^2})^p$  and hence

$$E = \frac{1}{N} \sum_{n=0}^{N-1} (1 - e^{-(n\sigma)^2})^p$$

for the energy of the mean image. This function is monotonically increasing in  $\sigma$ , and hence has no local minima. It is also independent of the distribution of binary point-targets, depending only on their total number through  $E_{av}$ .

## II.5 Simulation Results

We have run computer simulations using the range bin model given in (II.3.1) with  $N = 16$ . Starting with some trajectory,  $\tilde{\theta}$ , we added noise to produce an initial estimate,  $\hat{\theta}_0$ , then computed the corresponding initial image and its energy as given by (II.4.1). From there an optimization algorithm (having no knowledge of the true trajectory) was used to search state space for progressively "better" images. Figure II.3 shows a range bin consisting of 8 point targets. Figure II.4 is the image corresponding to an initial trajectory estimate while the image in figure II.5 corresponds to a point in state space eventually reached by the algorithm.

While the above approach is completely general, it requires a search over a space with  $N$  degrees of freedom. For large  $N$  this may not be practical. At the expense of generality we can reduce the degrees of freedom by parameterizing the trajectory (e.g.  $\theta_k = a_1 k + a_2 k^2 + \dots$ ) with  $M$  parameters where  $M \ll N$ . Our goal is then to obtain faithful estimates —  $\hat{a}_1, \hat{a}_2 \dots \hat{a}_M$ . Figures II.6 and II.7 show results for the case  $N = 16, M = 2$ , where the target is that in figure II.3; figure II.6 corresponding to the initial parameter estimates and figure II.7 corresponding to the improved estimates obtained by the optimization algorithm.

## II.6 Optical Processing

The optical implementation of the matched filtering process described in equation II.2.1 is straight forward. All we must do is to place the samples in the front focal plane of a Fourier transforming lens such that the transverse position of  $F_k$  is proportional to  $\theta_k$ . That is we must produce a transmittance in this plane given by

$$T(x) = \sum_k F_k \delta(x - a\theta_k)$$

where  $a$  is some constant. Due to the Fourier transforming property of the lens we get in its back focal plane a field ( $x$  and  $y$  are the transverse coordinates in the front and back

focal planes respectively)

$$\hat{f}(y) = \int dx T(x) e^{-j2\pi y(x/\lambda_o f)} = \sum_k F_k e^{-j2\pi y \hat{\theta}_k (a/\lambda_o f)},$$

where  $\lambda_o$  is the optical wavelength and  $f$  is the focal length of the lens. Comparing this expression to the right hand side of equation II.2.1 we see that they are identical except for a different scale factor in the exponent. As we have already seen this merely scales the image produced accordingly.

The transmittance  $T(x)$  can be produced by putting the samples on a carrier and then feeding them into an acoustooptic device with sample  $F_k$  entering the device at a time proportional to  $\hat{\theta}_k$  which is our best current estimate of  $\theta_k$ . When all the samples have entered the device a short laser diode pulse effectively freezes the position of the samples and produces the image  $\hat{f}(y)$ .

If we let the image fall on a photodetector array we can read out the pixel intensities serially, computing the energy  $E_n$  in equation II.4.1 as each pixel emerges and by keeping a running sum we will have computed the total energy  $E$  when the last pixel emerges. This energy value is then feed back to the circuitry which determines when the samples will be feed into the acoustooptic device at the next iteration.



## References

- [1] Ulaby, F.T., et. al., *Microwave Remote Sensing*, Vol 1, Ch 8.
- [2] Chen, C.C and Andrews, H.C., *Target-Motion-Induced Radar Imaging*, *IEEE Trans. Aero. and Elect. Sys.*, AES-16, 2, (1980).
- [3] Prickett, M.J. and Chen, C.C., *Principles of Inverse Synthetic Aperture Radar (ISAR) Imaging*, *IEEE EASCON*, Arlington, Va., Sep 29 — Oct 1, 1980.

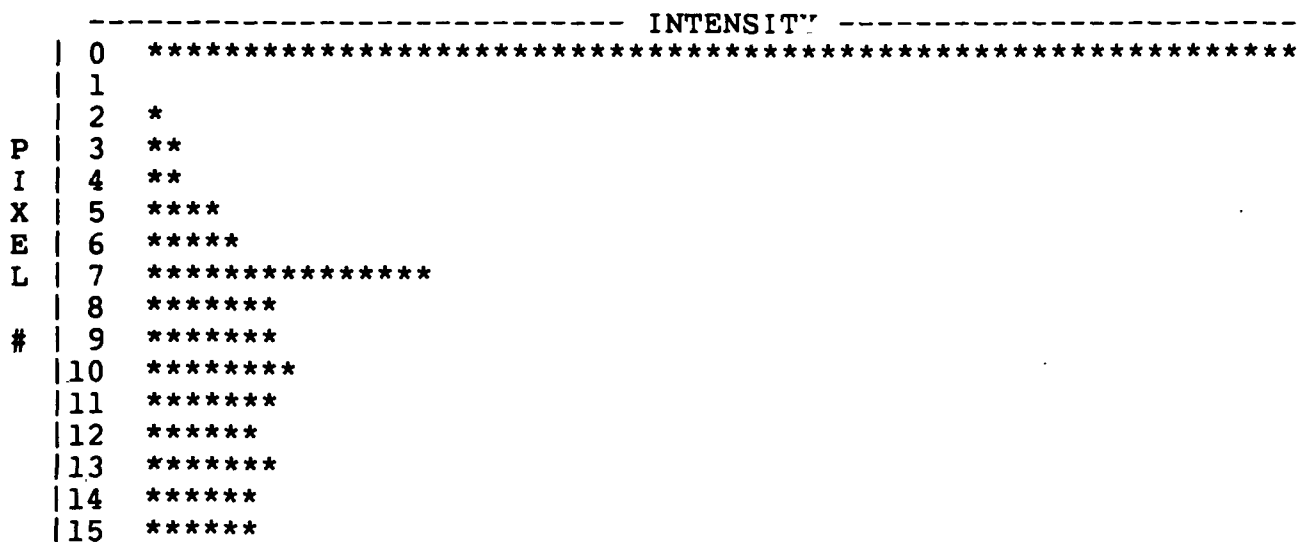


figure II.1 - mean of 100 images made with sigma=0.5

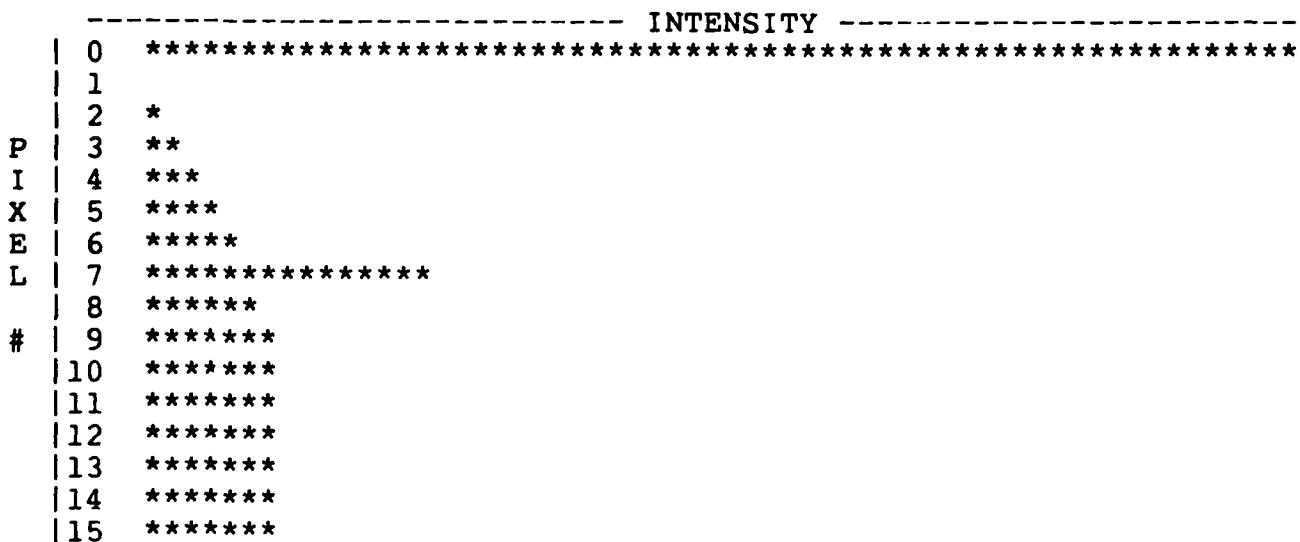


figure II.2 - equation II.3.5a with sigma=0.5

```

----- INTENSITY -----
P | 0 *****
I | 1 *****
X | 2 *****
E | 3 *****
L | 4 *****
# | 5 *****
  | 6 *****
  | 7 *****
  | 8 *****
  | 9 *****
  |10 *****
  |11 *****
  |12
  |13
  |14
  |15

```

figure II.3 - target (single range bin)

```

----- INTENSITY -----
P | 0 *****
I | 1 *****
X | 2 *****
E | 3 *****
L | 4 ****
# | 5 *
  | 6 ****
  | 7 *****
  | 9 *****
  | 9 *****
  |10 *****
  |11 *****
  |12 *****
  |13 *****
  |14 *****
  |15 *****

```

figure II.4 - initial image

```

----- INTENSITY -----
P | 0 *****
I | 1 *****
X | 2 *****
E | 3 *****
L | 4
# | 5 *
  | 6 *****
  | 7 *****
  | 8 *****
  | 9 *****
  |10 *****
  |11 *****
  |12 *****
  |13 *
  |14
  |15 *****

```

figure II.5 - "optimized" image

```

----- INTENSITY -----
P 0 *****
I 1 *****
X 2 *****
E 3 *****
L 4 *****
# 5 *****
  6 *****
  7 *****
  8 *****
  9 *****
10 *****
11 *
12 *****
13 **
14 *****
15 *****

```

figure II.6 - initial image (2 parameter case)

```

----- INTENSITY -----
P 0 *****
I 1 *****
X 2 *****
E 3 *****
L 4
# 5
  6
  7 *****
  8 *****
  9 *****
10 *****
11
12
13
14
15

```

figure II.7 - "optimized image"

### III LED BIPOLAR CORRELATOR

#### III.0 Introduction

Ever since Vander Lugt demonstrated optical matched filtering in 1964<sup>1</sup>, the main stream of optical pattern recognition has been correlation type image recognition. In addition to the ease of implementation by optics, matched filtering type correlator is also insensitive to any shift in position of the input pattern. Besides using a Fourier transform filter, matched filtering can also be implemented by using a correlation plane filter. The success of either scheme, however, is limited by the availability of linear spatial light modulators with sufficient dynamic range and accuracy. Subsequently, we resort to the use of a bipolar spatial light modulator. In this report, we address the issues of the feasibility of using an image plane bipolar filter for correlation and the performance of bipolar filters versus linear filters in terms of output signal to noise ratio. We also investigate the possibility of using a single bipolar filter for multiple patterns recognition; some algorithms of so doing; and the storage capacity of the bipolar filters corresponding to those algorithms. In the last four sections, we describe an optical system designed to implement the linear perceptron classification procedure using a bipolar filter.

#### III.1 Bipolar correlators

We begin our investigation by first analysing the performance of thresholding the input image<sup>2</sup>. The performance that we adopt here is  $SNR$ , the signal (correlation peak) to noise (additive noise and side-lobe) ratio. Let  $f(i, j)$  be the image to be recognized. Assume  $f(i, j)$  to be a discrete sequence of independent, identically distributed Gaussian random variables with zero mean and variance  $\sigma_f^2$ . The input image to the correlator is the sum of  $f(i, j)$ , the image to be recognized, and  $n(i, j)$ , an additive noise image. Here, we also assume  $n(i, j)$  to be an independent, discrete sequence of Gaussian random variables with zero mean and variance  $\sigma_n^2$ . The thresholded image is defined as

$$\hat{f}(i, j) = \begin{cases} 1, & \text{if } f(i, j) + n(i, j) \geq 0; \\ -1, & \text{if otherwise.} \end{cases} \quad (III.1.1)$$

The reference image  $h(i, j)$  is obtained by thresholding  $f(i, j)$ :

$$h(i, j) = \begin{cases} 1, & \text{if } f(i, j) \geq 0; \\ -1, & \text{otherwise.} \end{cases} \quad (III.1.2)$$

The correlation between the thresholded input and reference images is then given by

$$g(i', j') = \sum_i^N \sum_j^N \hat{f}(i, j) h(i + i', j + j') \quad (III.1.3)$$

The signal to noise ratio, defined as

$$SNR' = \frac{E^2[g(0,0)]}{var[g(i',j')],} \quad i', j' \neq 0 \quad (III.1.4)$$

can be shown to be

$$SNR' = N^2 \left[ \frac{1}{2} + \frac{1}{\pi} \tan^{-1}(SNR_{in}) \right]^2 \quad \text{where } SNR_{in} = \frac{\sigma_f}{\sigma_n}. \quad (III.1.5)$$

In order to see the effect of thresholding the input image, we compare  $SNR'$  with the signal to noise ratio that is obtained if the input image is not thresholded. It can be shown that in this case

$$SNR = \frac{N^2 SNR_{in}^2}{1 + SNR^2}. \quad (III.1.6)$$

The two  $SNRs$  are plotted in Figure III.1.1 as a function of  $SNR_{in}^2$ . As can readily be observed from the plot, the correlator with input image thresholded is only marginally degraded for high input  $SNR$ .

### III.2 Bipolar rotation invariant filters

Mathematically, any pattern  $f(r, \theta)$  can be decomposed into an infinite sum of its circular harmonics<sup>3</sup>,

$$f(r, \theta) = \sum_{n=-\infty}^{\infty} f_n(r) e^{-jn\theta}, \quad (III.2.1a)$$

where

$$f_n(r) = \int f(r, \theta) e^{jn\theta} d\theta. \quad (III.2.1b)$$

Thus, if the pattern is correlated with any component of its circular harmonics  $f_n(r) e^{-jn\theta}$ , the magnitude of the output is rotation invariant. Furthermore, if any component of circular harmonics is recorded on a Fourier transform hologram, the resulting filter is also shift invariant.

Computer generated bipolar filters were generated from the first two orders of circular harmonics of the letter A using the algorithm described by eq.(III.2.1). Numerical correlations of the letters A,B,C,and D and the binary CGHs were evaluated. The result is presented in Figure III.2.1. The intra-class recognition using the zeroth order circular harmonics is remarkable. However, the inter-class discrimination performance is barely satisfactory. In order to obtain good discrimination performance, cross correlations using bipolar filters generated from different circular harmonics have to be evaluated. A compromise between the inter- and intra- class discrimination performance will determine which bipolar filter to be used.

### III.3 Generalized bipolar filters

In this section, we examine the possibility of designing linear bipolar filters for recognizing multiple objects. One immediate extension of such a design, if it can be done, is to incorporate information corresponding to multiple versions of a certain object in a filter to achieve invariance (e.g. rotation and/or scale). We investigate two schemes that may accomplish this goal.

The first scheme is a derivative of the well known 2-category perceptron invented in the 60's<sup>4</sup>. Basically, a 2-category linear perceptron is a machine consisting of a weight pattern  $\underline{w}$  trained by a certain algorithm utilizing the set of all input patterns  $\{\underline{f}_m\}$  such that the output

$$g = \text{sgn} \left[ \sum_{i,j}^{N^2} w(i,j) f_m(i,j) \right] = \begin{cases} +1 & \text{if } f_m \text{ belongs to } \Psi; \\ -1 & \text{otherwise.} \end{cases} \quad (III.3.1)$$

We confine our attention to one of the simplest perceptron training algorithm, which is as follows: The set of input patterns is arranged as a repetitive sequence of patterns, i.e.  $\{\underline{f}^1, \underline{f}^2, \dots, \underline{f}^M, \underline{f}^1, \dots\}$ . The weight vector is trained by the elements from the sequence one at each time,

$$\underline{w}^{k+1} = \underline{w}^k + \alpha^k \underline{f}^k; \quad \underline{w}^1 = \text{some initial vector}, \quad (III.3.2a)$$

where

$$\alpha^k = \begin{cases} +1 & \text{if } g^k = \text{sgn}[\underline{w}^k \cdot \underline{f}^k] = -1 \text{ and } \underline{f}^k \in \Psi; \\ -1 & \text{if } g^k = +1 \text{ and } \underline{f}^k \notin \Psi; \\ 0 & \text{otherwise.} \end{cases} \quad (III.3.2b)$$

The algorithm has converged when the correct response is obtained for each input vector.

A bipolar perceptron can be defined by modifying the linear perceptron simply by replacing  $\underline{w}$  by a bipolar weight pattern. The training algorithm can also be modified to

$$\underline{w}^{k+1} = \text{sgn}[\underline{w}^k + \alpha^k \underline{f}^k] \quad (III.3.3)$$

The result of the rate of convergence of a bipolar perceptron trained using the above algorithm is shown in Figure III.3.1. An ordinate reading of  $10^4$  iterations means the binary perceptron did not converge within  $10^4$  steps. Even though a convergence proof does not exist, preliminary computer simulations do indicate a bipolar solution weight pattern can be obtained provided the dimensionality  $N$  is high enough. The statistical capacity with  $N = 16$  is shown in Figure III.3.2. Note that the capacity curve starts to roll off at approximately  $M$ , the number of stored vectors, equals to  $2N/3$ , whereas the capacity curve of a linear perceptron (not shown) does not roll off until  $M = N$ . This can be explained by the fact that the solution region of a linear perceptron may not contain a bipolar point. In such case, a bipolar vector does not exist which classifies all input vectors correctly.

The second scheme that can be used to recognize multiple patterns is described below. For ease of comparison, we first analyse the ordinary (non- bipolar) linear filter of the second scheme designed for the desired purpose. Consider the following algorithm: the operation to be performed is given as

$$g = \text{sgn} \left[ \sum_{i,j}^{N^2} h(i,j) f_m(i,j) \right] = \begin{cases} +1 & \text{if } f_m \text{ belongs to } \Psi; \\ -1 & \text{otherwise,} \end{cases} \quad (III.3.4)$$

where  $\Psi$  is the class of objects to be recognized. The filter  $h(i,j)$  is generated by forming a weighted sum of all the input patterns, i.e.

$$h(i,j) = \sum_{m'}^M \alpha_{m'} f_{m'}(i,j), \quad (III.3.5a)$$

where

$$\alpha_{m'} = \begin{cases} +1 & \text{if } f_{m'} \text{ belongs to } \Psi; \\ -1 & \text{otherwise.} \end{cases} \quad (III.3.5b)$$

To see that the above scheme is capable of recognizing multiple objects, rewrite equation (III.3.4) as

$$g = \text{sgn} \left[ \alpha_m N^2 f_m^2(i,j) + \sum_{i,j}^{N^2} \sum_{m' \neq m}^M \alpha_{m'} f_m(i,j) f_{m'}(i,j) \right]. \quad (III.3.6)$$

The RHS of the above equation is composed of two terms, namely, the signal (first) term and the noise (second) term. Provided that the signal term is sufficiently large comparing to the noise term, the correct response is expected.

Our next task is to obtain a theoretical estimate of the capacity of the filter. We define the capacity to be the number of vectors  $M_c$  that can be stored in a filter with vanishingly small probability of error for sufficiently large dimensionality  $N$ . Assuming  $f_m(i,j)$  to be a discrete sequence of bipolar-valued independent random variable, i.e.

$$\begin{cases} P[f_m(i,j) = 1] = P[f_m(i,j) = -1] = 1/2; \\ P[f_m(i,j) | f_{m'}(i',j')] = P[f_m(i,j)], \end{cases} \quad (III.3.7)$$

it can be shown that

$$M_c \simeq \frac{N^2}{8 \ln N}. \quad (III.3.8)$$

Shift invariance can be incorporated into this system by modifying the operation to be

$$g(i',j') = \text{sgn} \left[ \sum_{i,j}^{N^2} h(i,j) f_m(i+i',j+j') \right] = \begin{cases} +1 & \text{if } f_m \text{ belongs to } \Psi; \\ -1 & \text{otherwise.} \end{cases} \quad (III.3.9)$$



In such case, the capacity  $M_c$  can be shown to be

$$M_c \simeq \frac{N^2}{16 \ln N}. \quad (III.3.10)$$

The digitally computed correlations of random sequences (statistics given by eq.(III.3.7)) and the linear weighed-sum filter with different number of vectors stored are shown in Figure III.3.3. It can be seen from the simulated results that as the number of vectors stored in a filter increases, so do the magnitudes of the sidelobes. This phenomenon accounts for the limit of the number of vectors that can be stored in a weighed sum filter. The histogram of capacity with dimensionality  $N$  equals 128 is also shown in Figure III.3.4. The mean of the histogram agrees with the theoretical result.

For the bipolar analog of the above scheme, consider the same operation given by equation (III.3.4). In this case, the filter is generated by bipolarizing the filter given by equation (III.3.5). It is given as follows,

$$h(i, j) = \text{sgn} \left[ \sum_{m'}^M \alpha_{m'} f_{m'}(i, j) \right]. \quad (III.3.11)$$

Using the same statistics for the stored vectors, it can be shown that the capacity of a bipolar weighted sum filter is only reduced by a factor of  $\pi/2$ . Thus

$$M_b \simeq \frac{2}{\pi} \frac{N^2}{16 \ln N}, \quad (III.3.12)$$

for filters with shift invariance incorporated, and

$$M_b \simeq \frac{2}{\pi} \frac{N^2}{8 \ln N}, \quad (III.3.13)$$

for filters without. Computer simulated correlations of random vectors and the bipolar filter formed by the above algorithm are shown in Figure III.3.5. Note that the magnitude of the peak decays as the number of vectors stored increases in this case. This phenomenon is understandable, since as  $M$  increases, the relative information of each vector stored in the filter decreases. The histogram of capacity of the corresponding bipolar filter is also shown in Figure III.3.6. The mean of the histogram agrees with the theoretical result.

### III.4 Optical System Implementation

Elsewhere we have described a two-dimensional incoherent acousto-optic image correlator<sup>5</sup> and have discussed various advantages associated with this form of processing. Here we will describe the implementation of bipolar correlations using such a system. The basic system architecture is shown in figure (III.4.1) and consists of a 16 element vertical LED array in the reference plane, an acousto - optic device (AOD) in the input plane, and a CCD camera in the output plane. An IBM PC is used to load reference image data into the electronic memory shown. The data is read out to the LEDs, 32 bits at a time in such a way as to modulate the intensity of the  $i^{th}$  LED with consecutive pixel values of the  $i^{th}$  reference image line. A 2 bit D-A converter preceeding each LED allows for representation of up to 4 distinct intensity levels per pixel. In the applications reported here, three of these levels are used to represent an unbiased bipolar signal (-1,0,1) as a biased unipolar signal (0,1,2). The imaging optics and signal timings are such that the TDI output of the CCD is proportional to the correlation between the bipolar input and reference images plus some bias term. The  $i^{th}$  LED is intensity modulated by the current :

$$A_i(t) = [1 + a_i(t)]\text{rect}(t/T_1)$$

where  $a_i(t)$  represents the bipolar signal associated with the  $i^{th}$  line of the reference image, and  $T_1$  is the reference image width. The  $j^{th}$  line of the input image results in an intensity modulation of the diffracted light after the AOD (assuming uniform incident intensity) that is given by :

$$B_j(t - x/v) = [1 + b_j(t - x/v)]^2 \text{rect}\left(\frac{t - x/v}{T_2}\right)$$

where  $b_j(t)$  is the bipolar signal associated with the  $j^{th}$  line of the input image, and  $T_2$  is the TV horizontal line time plus blanking interval. Using this we obtain the  $n^{th}$  line of the CCD output as :

$$\begin{aligned} C_n(x) &= \sum_{n'=n-M+1}^{n'=n} \int_{-\infty}^{\infty} A_{n'+M-n}(t) B_{n'}(t + x/v) dt \\ &= \sum_{n'=n-M+1}^{n'=n} \int_{-T}^T [1 + a_{n'+M-n}(t)] [1 + b_{n'}(t + x/v)]^2 dt \quad (III.4.1) \\ &= T_n(x) + 2 \sum_{n'=n-M+1}^{n'=n} \int_{-T}^T a_{n'+M-n}(t) b_{n'}(t + x/v) dt \end{aligned}$$

where  $T_n(x)$  is the bias signal on the  $n^{th}$  output line, M is the number of CCD lines and the correlation time  $T$  is given by :  $T = T_1 + T_2$ .

In order to obtain the true correlation  $a(x, n) * b(x, n)$  we clearly must remove the bias term from equation (III.4.1). It is important to note that under the condition :

$$\langle a_i(t) \rangle = \langle b_j(t) \rangle = 0 \quad \forall \quad i, j \quad (III.4.2)$$

where the symbol  $\langle \rangle$  represents the expectation or average value, the bias signal  $T_n(x)$  is independent of the input and reference signals.

### III.5 Correlation Results

We have implemented the above system and have obtained correlation results as shown in figure (III.5.1). In our experiments, the three images shown in figure (III.5.1a) were presented to the TV camera as the input scene. The input scene signal was first passed through a DC block in order to remove any bias. After also removing the horizontal and vertical sync pulses the signal was amplified and a constant level was added. This level was adjusted so as to insure that the input signal was strictly positive. For a bipolar input scene then, this unipolar signal is simply the  $[1 + b(t)]$  described earlier. This modified signal was used to amplitude modulate a 50 MHz RF carrier which was then applied to the AOD.

Various reference images were generated using an IBM PC. Each reference image was 16 lines high by 32 pixels wide however, by virtue of the bipolar encoding scheme employed, a data array of 32 bits by 32 bits was necessary to represent one image. At the beginning of each input image horizontal line time, the 32 lines of reference data were read out to the LEDs. Preceding each LED was a 2 bit resistive ladder network used to convert two bits of digital data into one of the 3 appropriate analog levels. The output correlations are shown in figures (III.5.1b,c,d) for various reference images. As can be seen from the figures, the system exhibits good cross correlation suppression and strong autocorrelation peaks.

### III.6 Bias Considerations

In order to represent a bipolar signal in light intensity, a constant bias is added to the signal before modulation. The presence of this bias term in  $A(t)$  and  $B(t)$  results in the bias term  $T_n(x)$  in the system output. Removal of  $T_n(x)$  is therefore required before the true correlation may be observed. Shown in figure (III.6.1) is a typical line of the bias signal  $T_n(x)$ . As expected, the bias signal is approximately triangular, characteristic of the correlation between the two rectangular functions associated with  $A(t)$  and  $B(t)$ .

Removal of the bias function  $T_n(x)$  is achieved by first generating a bias reference image and a bias input image. A recording of the 2-D output correlation of these two images is exactly  $T_n(x)$  assuming the conditions of eq. [III.4.2]. Thereafter, in order to retrieve the true correlation from the system output,  $T_n(x)$  may be subtracted from  $C_n(x)$  on a pixel by pixel basis. This will yield the desired signal :

$$a(x, n) * b(x, n) = C_n(x) - T_n(x)$$

If the condition of eq. [III.4.2] is not satisfied then the bias term  $T_n(x)$  becomes signal dependent. In general, it is easily shown that the bias signal is given by :

$$T_n(x) = \sum_{n'=n-M+1}^{n'=n} \int_{-T}^T 2 + 2[a_{n'+M-n}(t) + b_{n'}(t - x/v)] \text{rect}(t/T_1) \text{rect}\left(\frac{t - x/v}{T_2}\right) dt \quad (III.6.1)$$

We see that the first term is the typical triangular bias ; however, the second term is in fact signal dependent. Various schemes for removing the second term from eq. [III.6.1] may be envisioned. One particularly straightforward method would be to simply record the two signals :

$$signal1 = \sum_{n'=n-M+1}^{n'=n} \int_{-T}^T a_{n'+M-n}(t) rect(t/T_1) rect(\frac{t-x/v}{T_2}) dt$$

$$signal2 = \sum_{n'=n-M+1}^{n'=n} \int_{-T}^T b_{n'}(t-x/v) rect(t/T_1) rect(\frac{t-x/v}{T_2}) dt$$

and perform a pixel by pixel subtraction off line as we did with the signal independent term. It is important to note that if the quantity of interest is the inner product of two images rather than the entire 2-D correlation, then the condition of eq. [III.4.2] may be relaxed somewhat. In this case it is necessary only to have equal numbers of 1s and -1s over the entire image to insure signal independent bias.

### III.7 Implementation of a Linear Discriminant Function

The above system has been utilized in a pattern recognition scenario. Taking advantage of the flexibility afforded by the computer generated reference images, it is possible to form arbitrary linear combinations of these images to generate more powerful filters. A LDF based on three images was generated using a bipolar perceptron type algorithm as described in section III.3. In our experiments the algorithm was initialized with the filter :

$$w^1 = \sum_{i \text{ in } \Psi_1} IMG_i - \sum_{i \text{ in } \Psi_2} IMG_i$$

where  $\Psi_1$  and  $\Psi_2$  are the two classes and  $IMG_i$  is one of the three images to be classified. Since only three levels may be represented in our system, a threshold arithmetic must be implemented. That is, when executing the above algorithm we have that  $1 + 1 = 1$  and that  $-1 - 1 = -1$ . Although there is no guarantee of convergence in the bipolar case, we observed convergence for all three dichotomies. The LDF as found above was used as the reference image while the three seed images were placed in the input plane. The results for three different class assignments are shown in figure (III.7.1). We see that successful classification was achieved for all three of the nontrivial dichotomies possible.

### III.8 Conclusion

We have shown that the performance, in terms of output  $SNR$  and storage capacity, of bipolar correlation filters does not severely degrade when compared to conventional correlation filters. As a matter of fact, bipolar SLMs are free of the problems of limited

dynamic range and non-linearity. We have also presented experimental results pertaining to an incoherent acousto-optic correlation architecture. The particular system we describe implements bipolar correlations between a TV scene and a computer generated reference image. Good correlation results have been obtained. We have also successfully implemented a two class decision machine using this correlator. Many issues still remain to be researched. For instance, how a bipolar filter is optimized is one of them. How a bipolar perceptron is trained to recognize multiple objects is another example. For a certain set of data, a bipolar filter which will make the right decision in recognition may not exist at all. It is, nevertheless, the authors' belief that the probability of having such a bipolar filter approaches one for sufficiently high dimensionality.

## References

- [1] A. Vander Lugt, IEEE Trans. Inf. Theory IT-10,2 (1964).
- [2] D. Psaltis, E.G. Paek, and S.S. Vankatesh, Opt. Eng. 23(6), 698(1981).
- [3] Y.N. Hsu, H.H. Arsenault, and G. April, Appl. Opt. 21,4012 (1982).
- [4] N.J. Nilson, Learning Machines: foundations of trainable pattern-classifying systems, McGraw-Hill Book Company, 1965.
- [5] D. Psaltis, Appl. Opt. 21, 491 (1982)
- [6] D. Psaltis, Opt. Eng. 23,1 (1984)

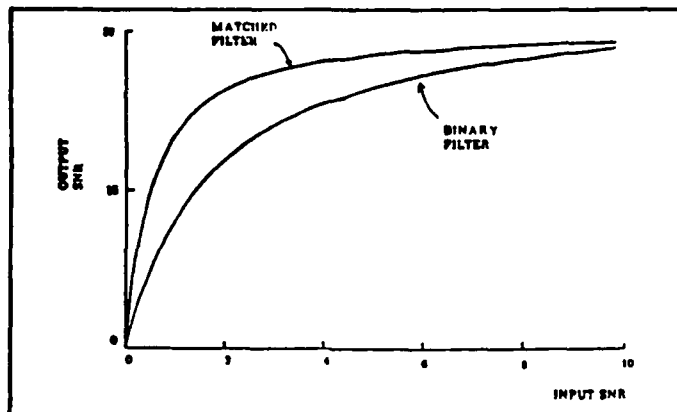


Figure III.1.1. Output vs input SNRs for the binary and conventional correlators.

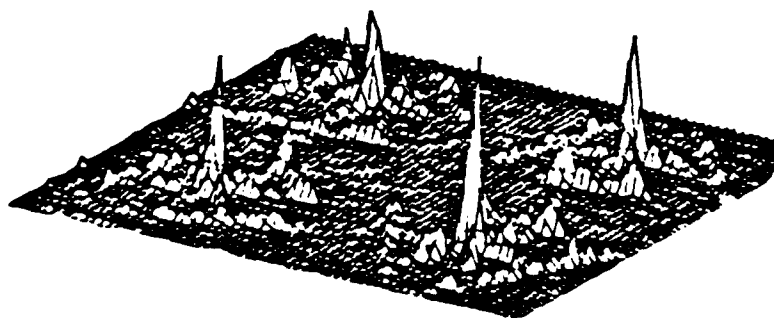
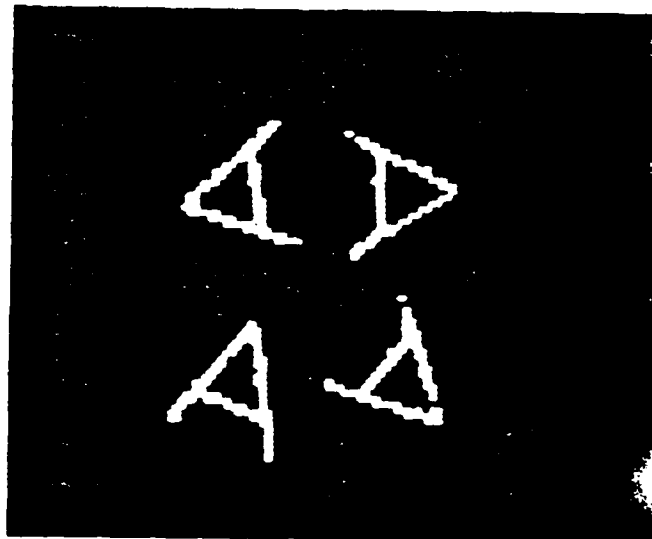
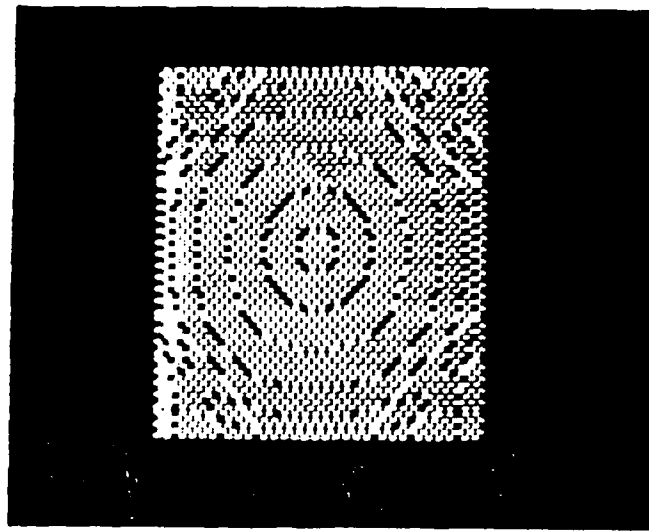


Figure III.2.1. (a) Zeroth order circular harmonic binary CGH. (b) Image of 4 A's of different orientations. (c) Computer simulated correlation result of (a) and (b).



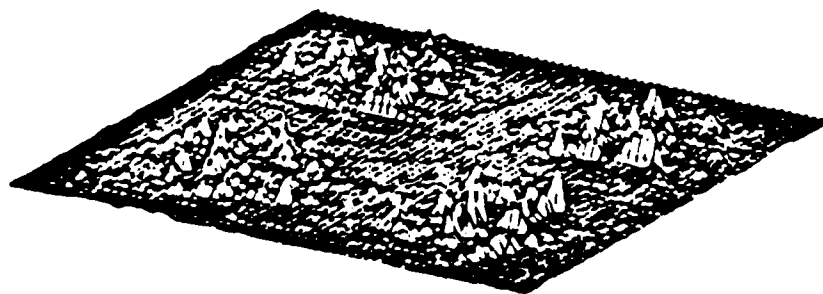
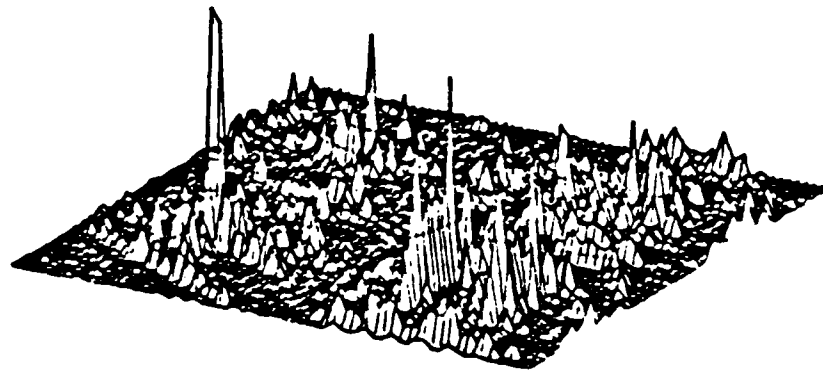
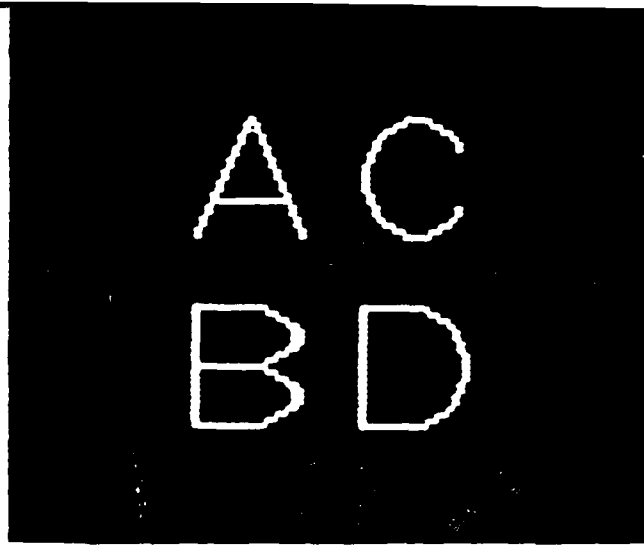


Figure III 2.1. (d) Image of of the letters A,B,C and D. (e) Computer simulated correlation result of (a) and (d).

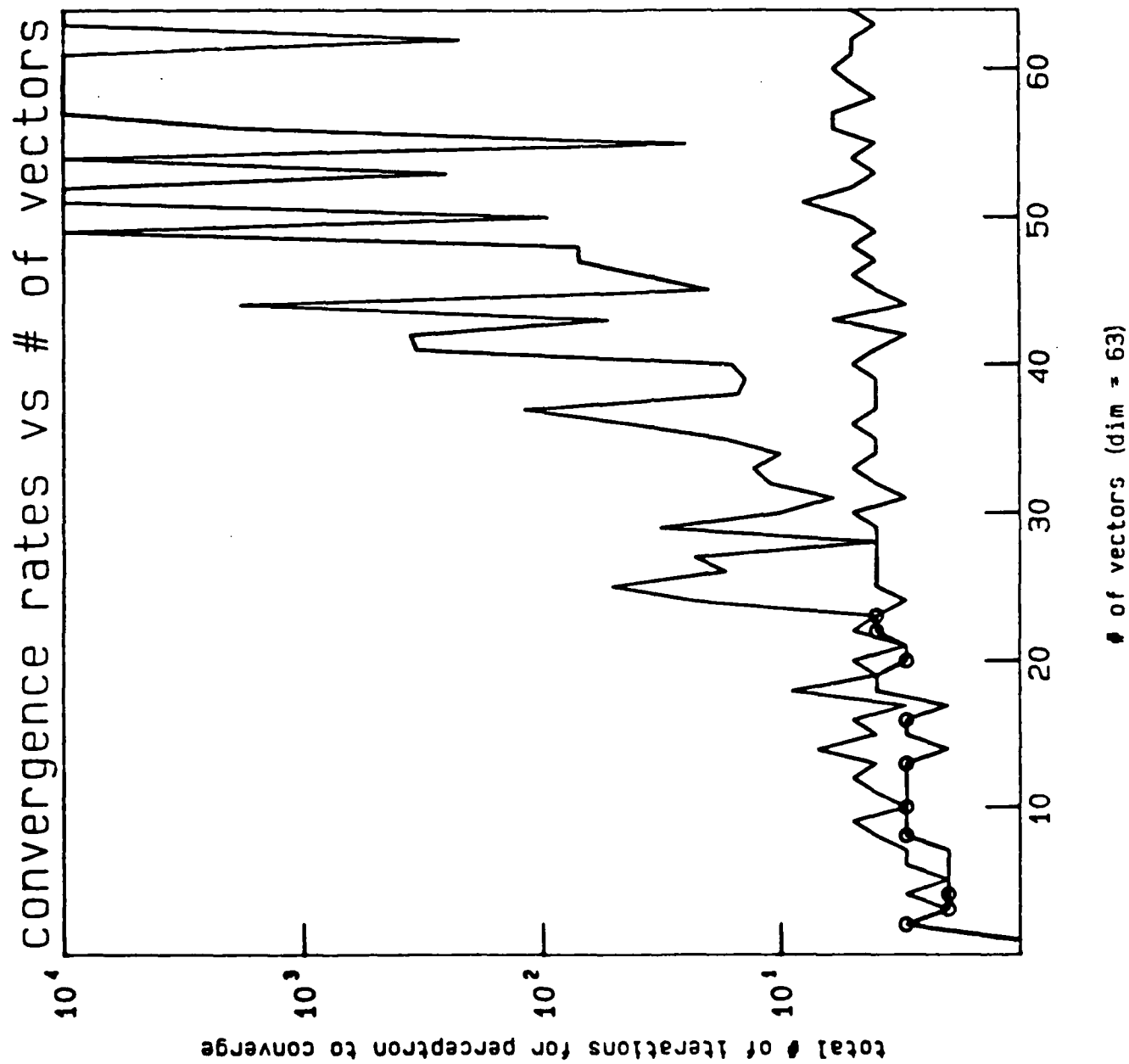


Figure III.3.1. The rate of convergence of a bipolar perceptron. The rate of convergence of an ordinary perceptron of the same data set is also plotted for comparison. The circles on the plot are the bipolar vectors generated by taking the  $\text{sgn}||$  of the ordinary perceptron that dichotomize the data set correctly.

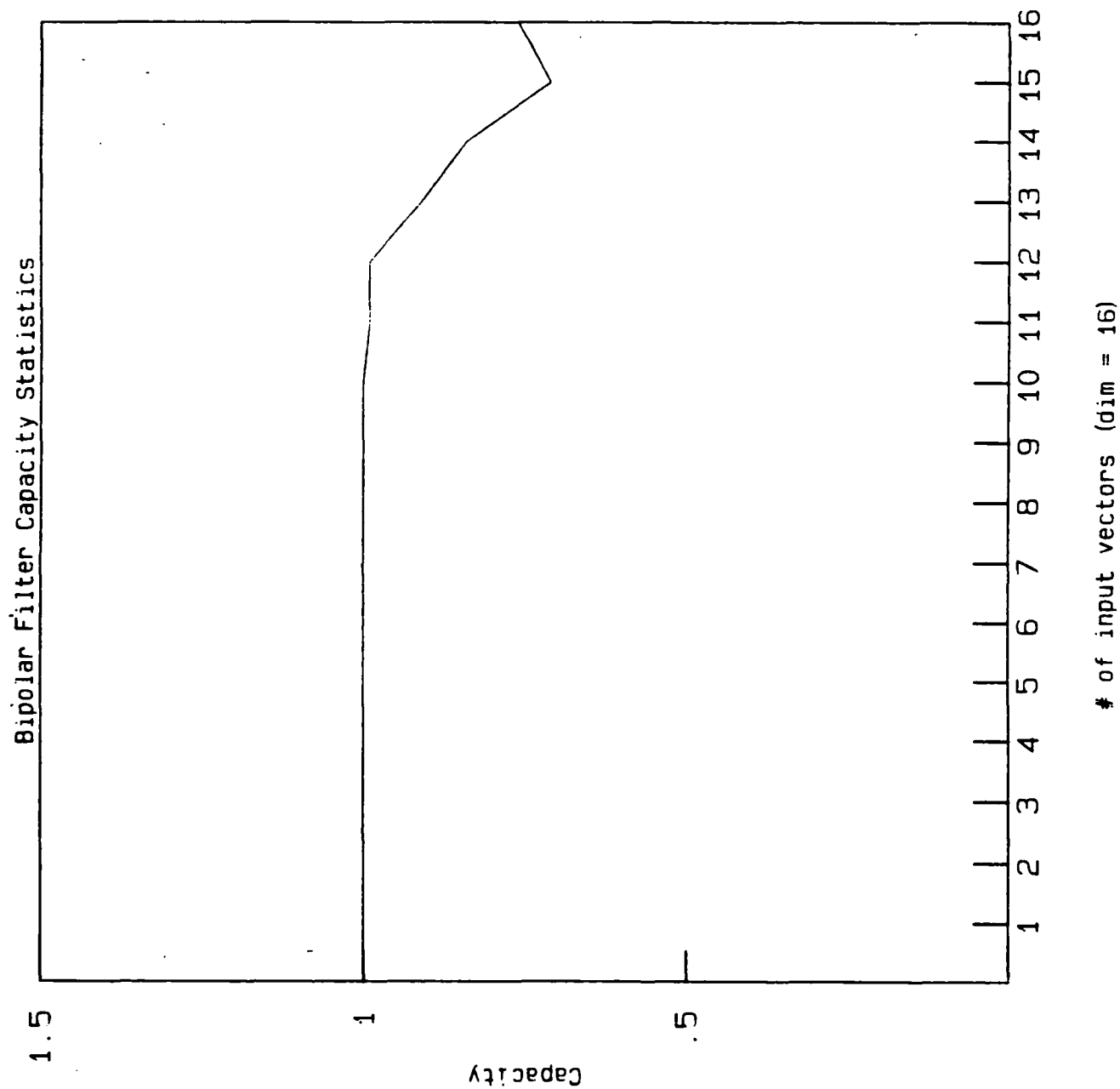


Figure III.3.2. The statistical capacity of a bipolar filter with non-zero threshold and number of weight components equal 16.

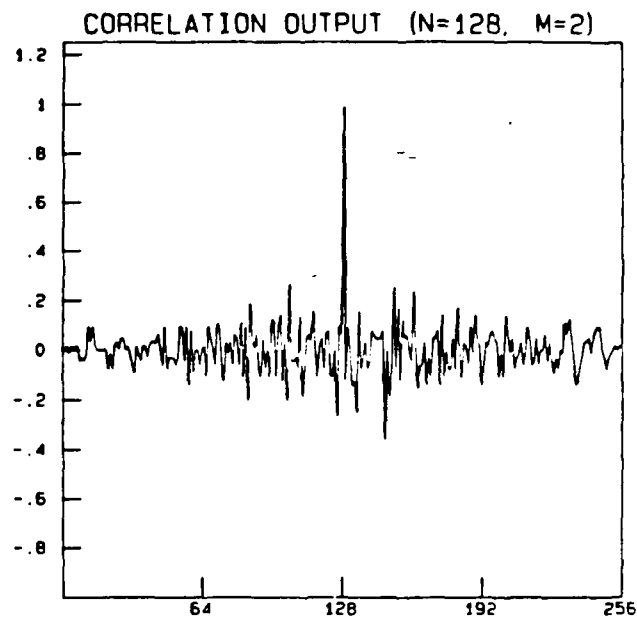
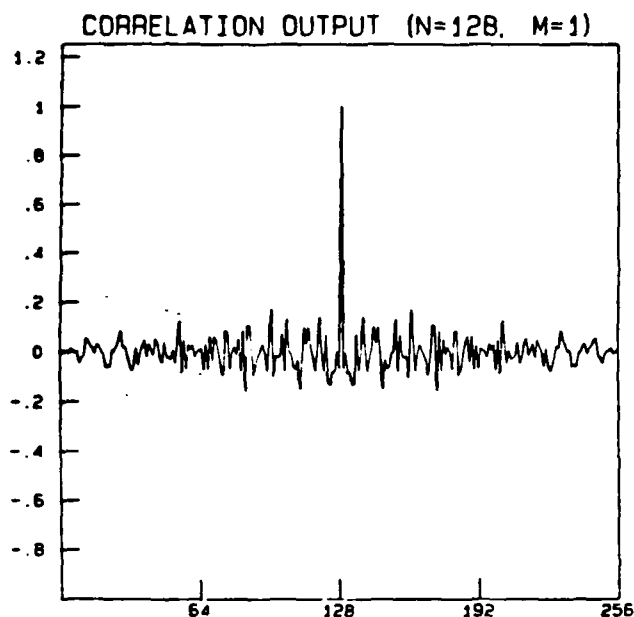
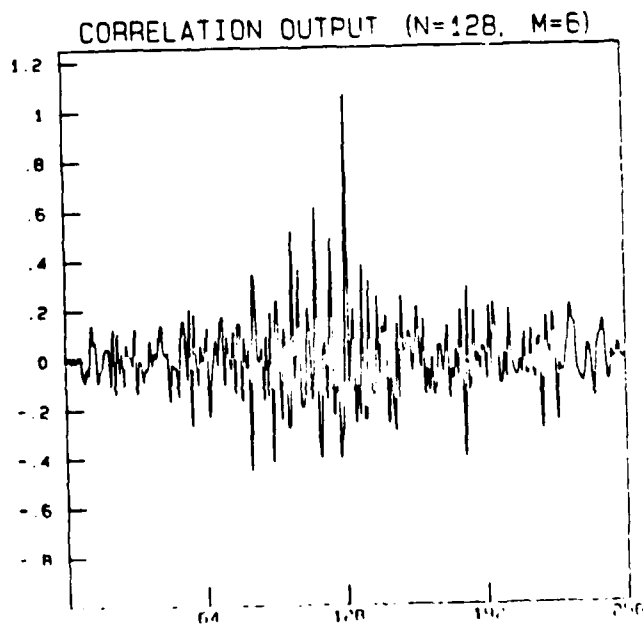
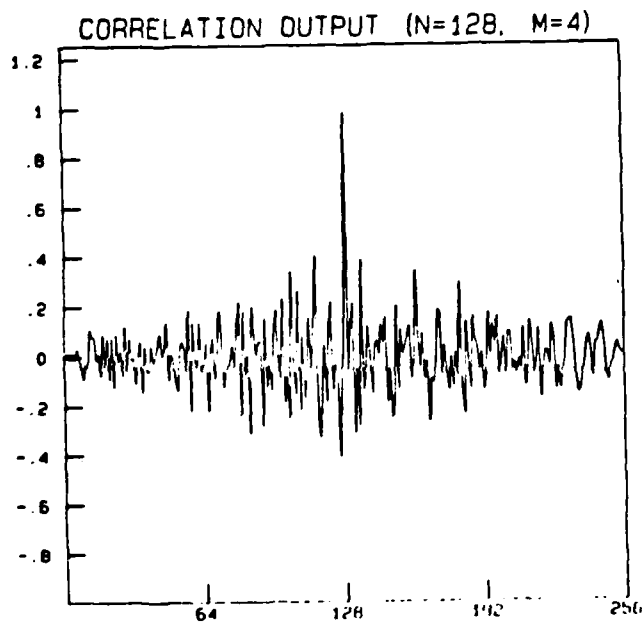


Figure III.3.3. The simulated correlations of the linear weighed-sum filters of different number of stored vectors and some of their stored vectors. The threshold level for recognition is one half of the energy of each vector.



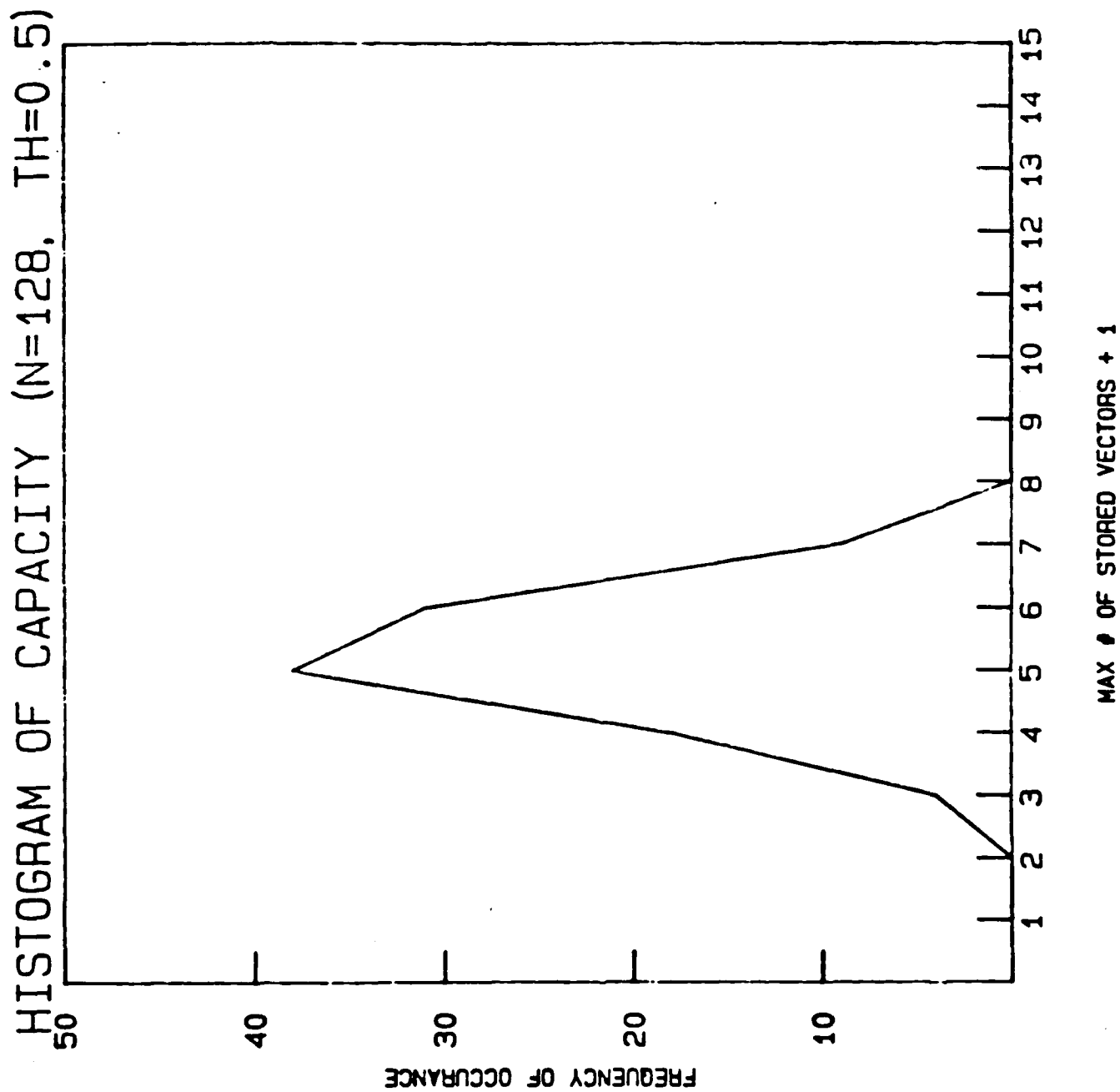


Figure III.3.4. The histogram of storage capacity based on 100 trials.

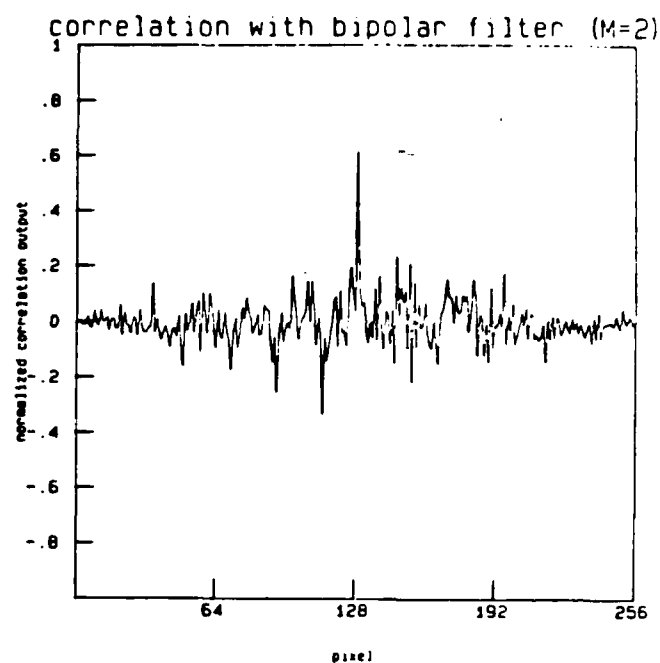
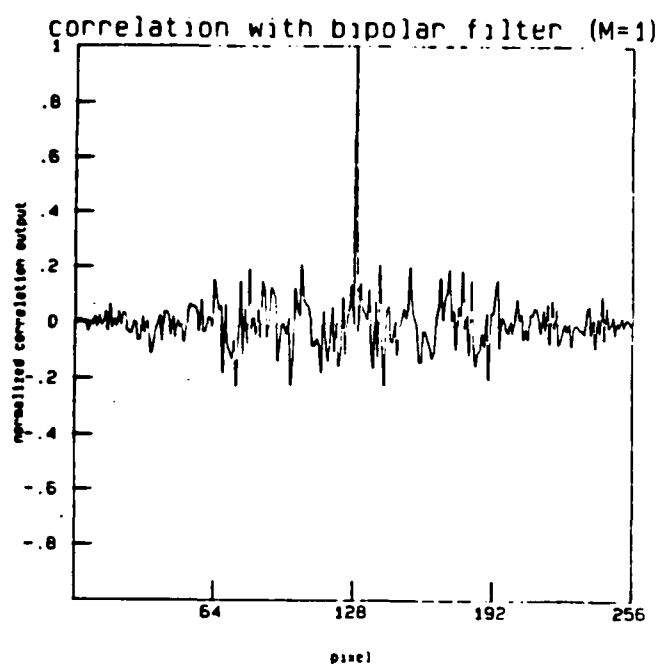
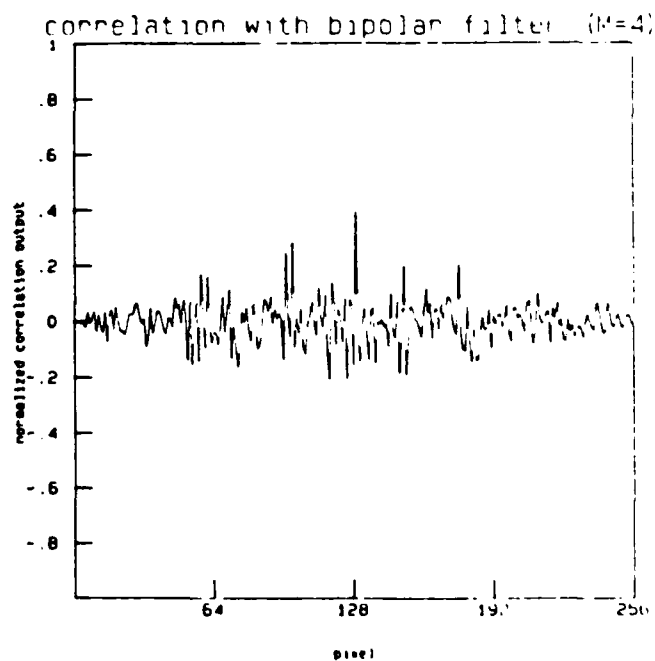
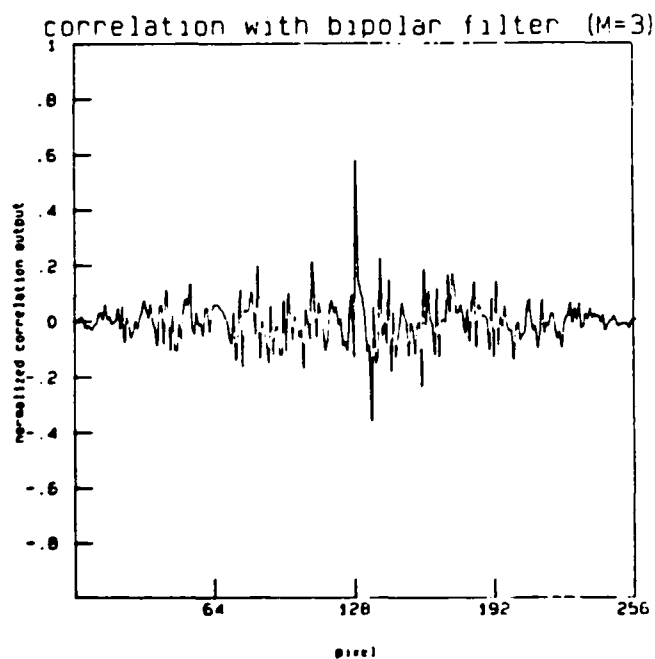


Figure III.3.5. Computer simulated correlations of bipolar weighed-sum filters of different number of stored vectors and some of their stored vectors. The threshold level for recognition is one half of the energy of each vector.



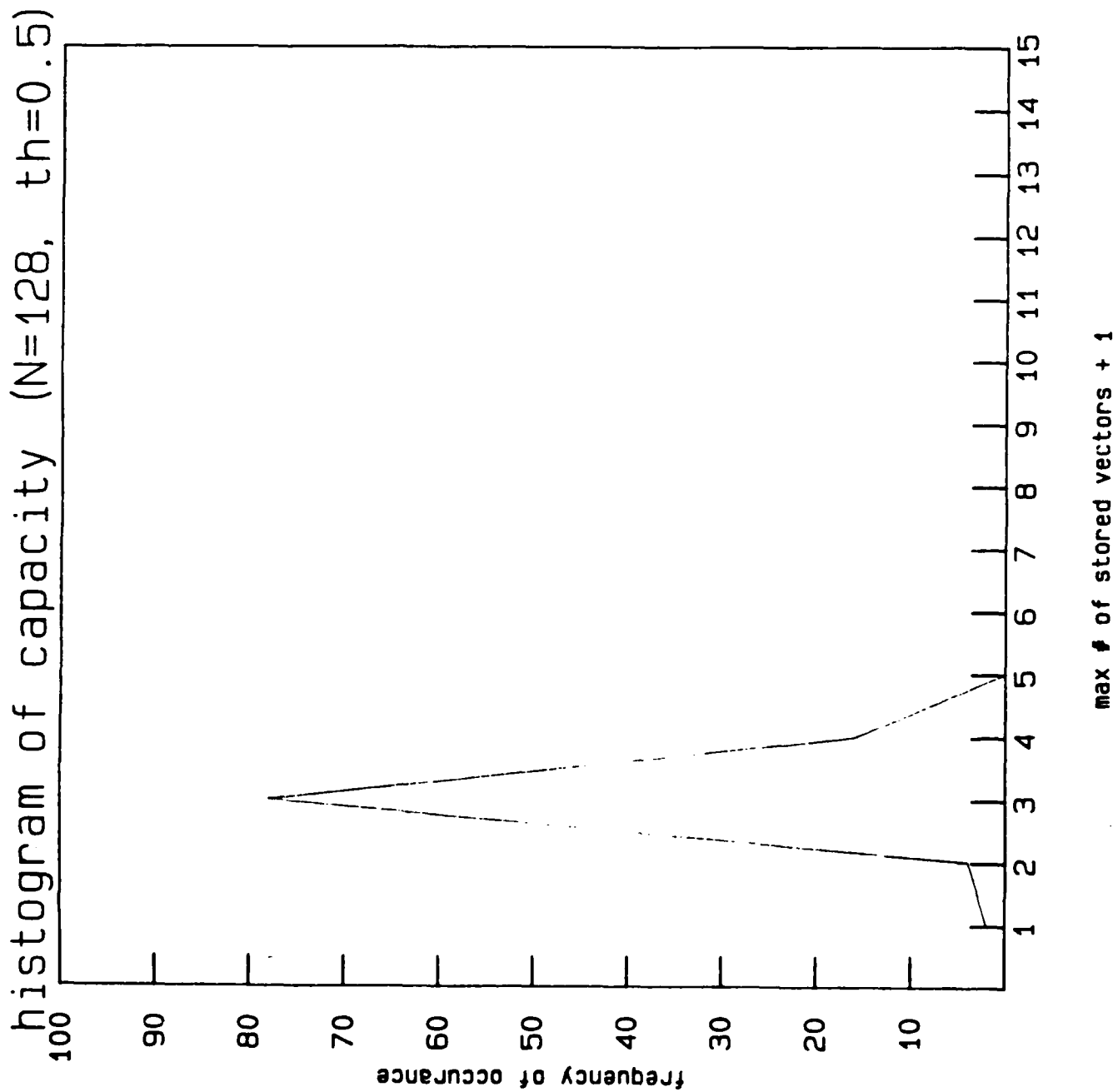
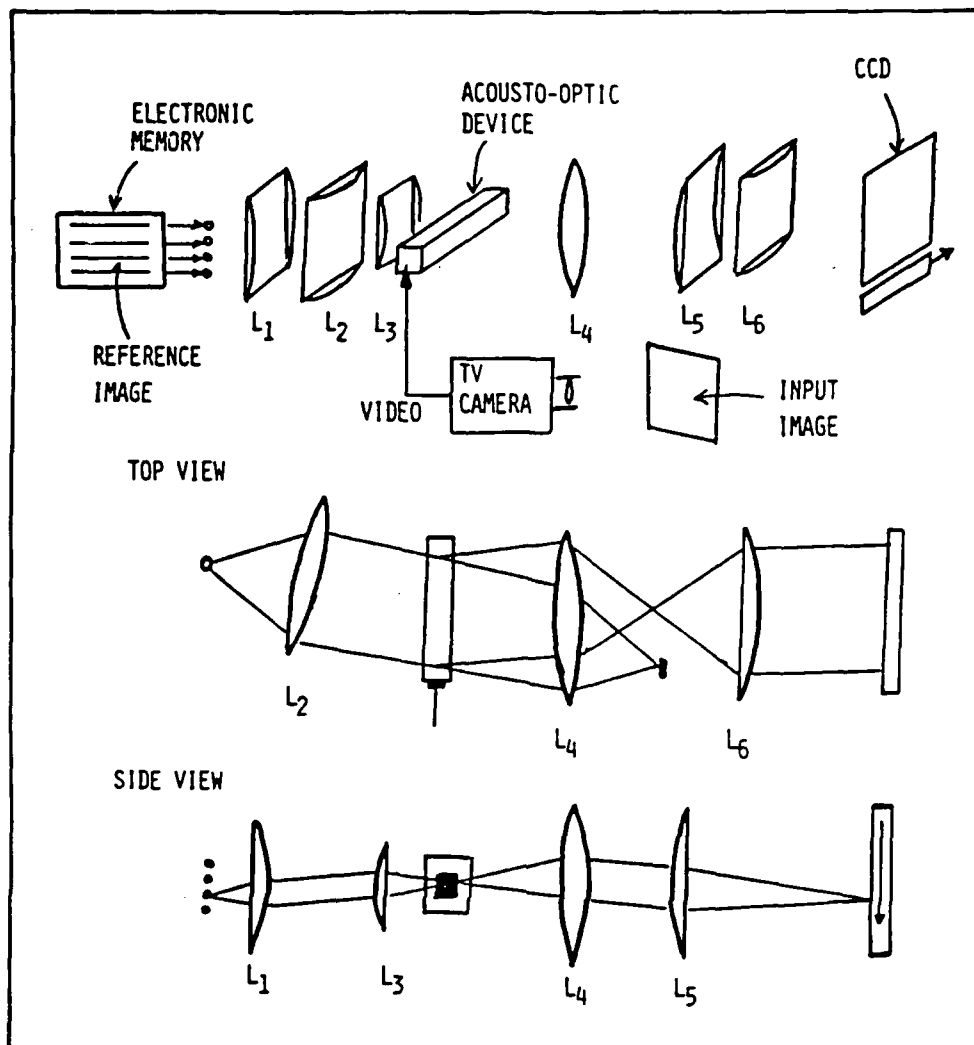
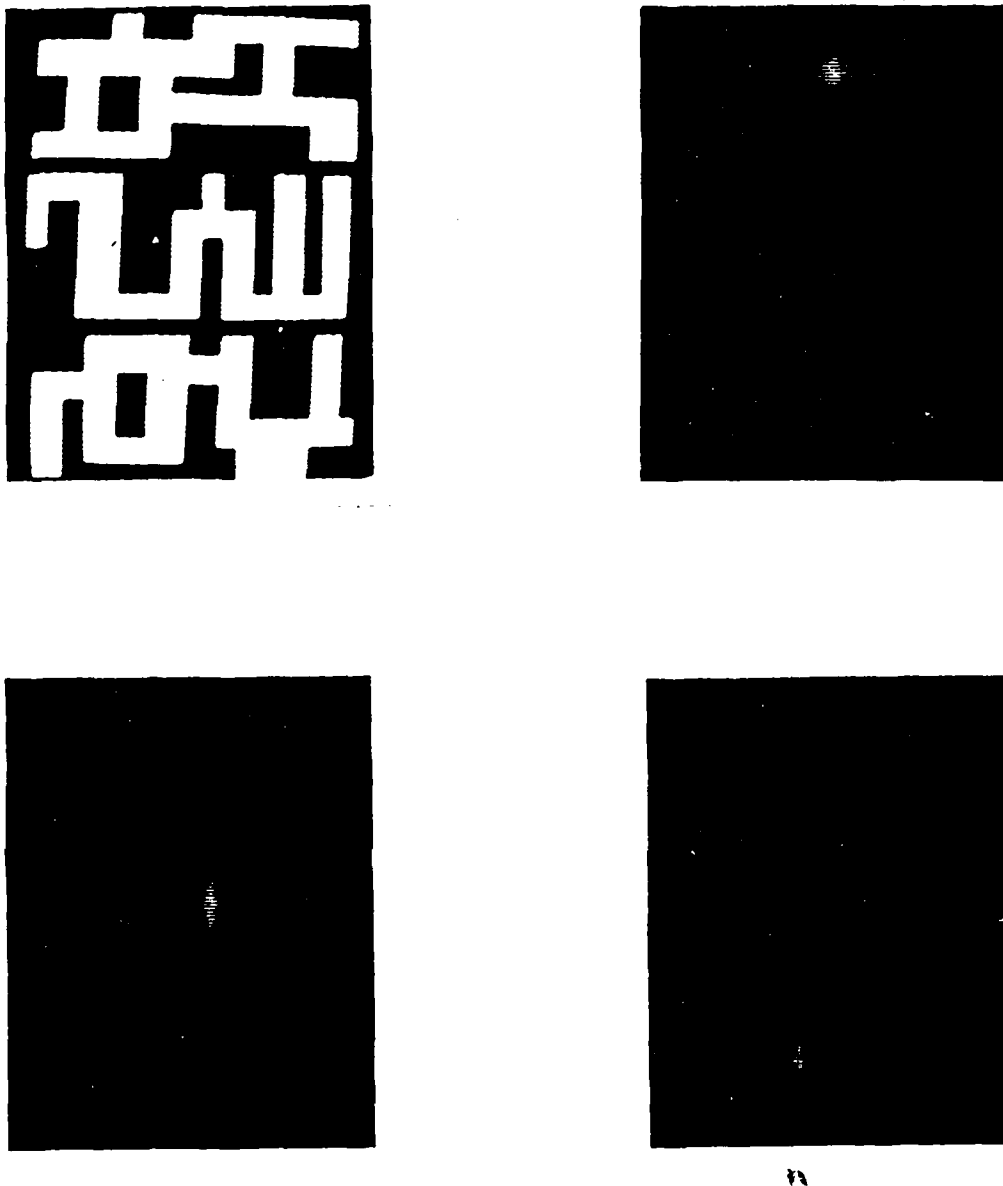


Figure III.3.6. The histogram of storage capacity of the bipolar weighed-sum filter based on 100 trials.



**Figure III.4.1 : Incoherent Correlator Architecture**





**Figure III.5.1 : Correlation Results**

- (a) Input scene [top: IMG1, middle: IMG2, bottom: IMG3]
- (b) Correlator output for reference image = IMG1
- (c) output for ref. = IMG2
- (d) output for ref. = IMG3

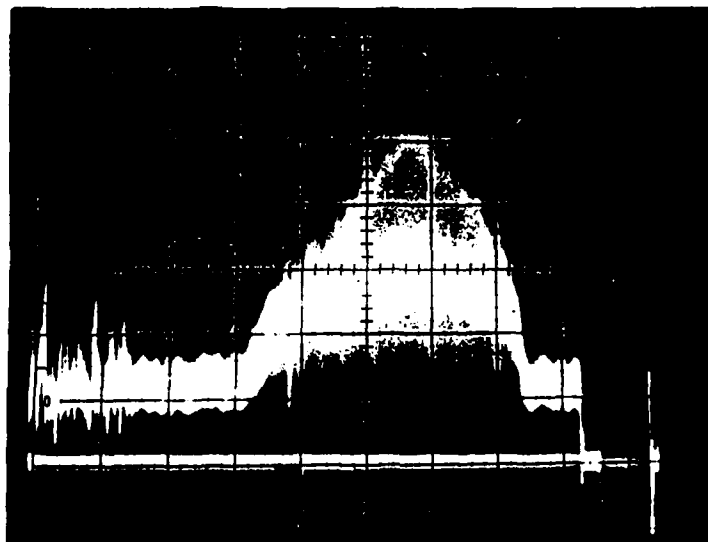


**Figure III.6.1** : Typical Line of Correlator Bias

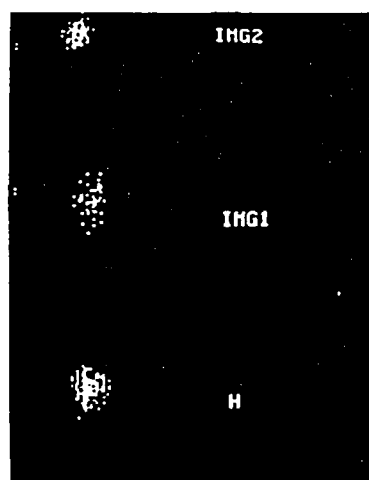
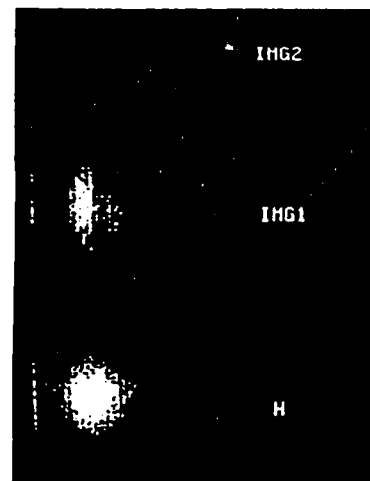
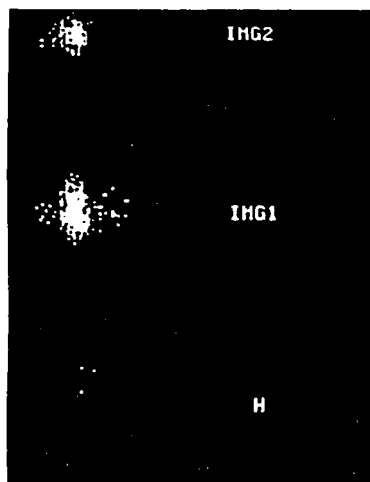


**Figure III.7.1 : Discriminant Function Implementation**

- (a) Correlator Output for Class 1 =  $IMG1+IMG2$  / Class 2 = H
- (b) Class 1 =  $IMG1+H$  / Class 2 = IMG2
- (c) Class 1 =  $IMG2+H$  / Class 2 = IMG1

## **IV MULTIPLICATIVE TIME AND SPACE INTEGRATING**

### **ACOUSTO-OPTIC SPECTRUM ANALYZER**

#### **IV.0 Introduction**

In this section we will describe multiplicative time and space integrating (TSI) acousto-optic architectures for spectrum analysis of images and of 1-D signals. The TSI approach is used which combines the best features of 1-D space integrating and 1-D time integrating spectrum analyzers<sup>1</sup>. Wagner and Psaltis have previously demonstrated experimentally an additive architecture for folded spectrum processing of 1-D signals<sup>2</sup>. In this section we describe and experimentally demonstrate a multiplicative processor suitable for finding the 2-D Fourier spectrum of images. The information signal is fed into a Bragg cell and a lens takes the Fourier transform in the coarse frequency (x) direction of the image. In the second Bragg cell, the DFT signal is entered which along with the time integrating CCD calculates the Fourier transform in the fine frequency (y) direction of the image. We begin the section by describing the principles of TSI processing. The space integrating spectrum analyzer is described using 1-D time signals and 2-D video images as inputs. Then, the Discrete Fourier transform (DFT) based time integrating spectrum analyzer is described and experimental results are given. The possible TSI architectures are given and analysis is carried out. Experimental data is presented and system performance issues such as bias removal techniques are discussed. We end with a summary of the processor and its possible applications.

#### **IV.1 Principles of TSI Processing**

Fig.IV.1.1 shows the basic setup for a TSI architecture for spectrum analysis. Bragg cells are used as input SLMs because of their high bandwidth. The input signal  $s(t)$  is a long 1-D signal that cannot be enclosed in the time window of the Bragg cell. This leads to representing  $s(t)$  as a space-time raster  $f(x,n)$  where  $n$  is the laser diode pulse number. This raster then passes through a Fourier transforming lens with power in the x-direction giving another space-time raster  $F_x(u,n)$  which consists of spatial Fourier transforms of the windowed signal  $s(t)$ . Next, the raster  $F_x(u,n)$  is spectrally resolved in temporal frequency by using time integrating Fourier transform modules. The output of the system is a folded spectrum of the input  $s(t)$ . The motivation for dividing the 2-D Fourier transform operation into a space integrating lens Fourier transform and  $N$  time integrating Fourier transforms comes from the separability of the 2-D Fourier kernel as noted in equation (IV.1.1). Figure IV.1.2 shows the basic principle of folded spectrum systems originally shown by Thomas<sup>3</sup>. Possible inputs  $s(t)$  to a folded spectrum system can be a narrowband highly coherent signal burried in white noise (SETI) or a video signal from a camera pointed at an image  $f(x,y)$ .<sup>2</sup> A video signal has a natural rastering mechanism, therefore the

2-D folded spectrum output is the 2-D Fourier spectrum of the input video image.

$$F(u, v) = \sum_{n=0}^{N-1} \left[ \int_A f(x, n) e^{-j2\pi ux} dx \right] e^{-j2\pi v \frac{n}{N}} \quad (IV.1.1)$$

## IV.2 Space Integrating Spectrum Analyzer

Figure IV.2.1 shows the optical setup for the SI Spectrum Analyzer. The field amplitude at the detector plane is

$$F(x', t) = \int_A \tilde{s}\left(t - \frac{x}{v}\right) e^{-j2\pi x \frac{x'}{v}} dx e^{-j\omega t} = [v\tilde{S}(uv) e^{-j2\pi uv t} * \text{Asinc}(Au)] e^{-j\omega t}$$

where  $v$  is the acoustic signal velocity in the Bragg cell and  $\tilde{s}(t)$  is the complex diffracted signal.

Using the reference signal  $r$  for heterodyne detection, the intensity on the detector plane is

$$I(x', t) = |[v\tilde{S}(uv) e^{-j2\pi uv t} * B(u)] + r|^2$$

For a single tone input

$$s(t) = a \cos(2\pi f' t)$$

the intensity is

$$I(x', t) = |a|^2 B^2\left(u - \frac{f'}{v}\right) + |r|^2 + 2|a|r B\left(u - \frac{f'}{v}\right) \cos(2\pi f' t + \Omega)$$

Taking the pulsing action of the laser diode into account every  $T$  seconds, the intensity on the  $n^{\text{th}}$  pulse is

$$I(x', n) = |a|^2 B^2\left(u - \frac{f_c}{v}\right) + |r|^2 + 2|a|r B\left(u - \frac{f_c}{v}\right) \cos(2\pi \delta n T + \Omega) \quad (IV.2.1)$$

where  $B(u)$  is the general blurr spot taking into account the finite aperture of the Bragg cell and acoustic apodization effects. Also,

$$f' = \frac{k}{T} + \delta = f_c + \delta$$

$$a = |a| e^{j\Omega}$$

Equation (IV.2.1) shows that for a single tone input, the output of the processor consists of a constant bias term, a signal dependent bias term positioned according to the signal coarse frequency  $f_c$  and a sampled temporal modulation at the signal fine frequency. The third term contains the original input signal, except it has been heterodyned to baseband by the pulsing action of the laser diode. It is this temporal modulation that

allows us to use time domain spectral analysis schemes, such as the DFT algorithm to resolve the signal into higher resolution spectral components. In order to avoid aliasing effects between the bandlimited signals in each coarse frequency blurr spot, we need to satisfy the Nyquist criteria .i.e

$$\frac{1}{T} > \frac{2}{T_a}$$

where  $T$  is the sampling time of the laser diode and  $T_a$  is the aperture of the Bragg cell. When  $s(t)$  is a video signal where  $f_n$  represents the  $n^{th}$  video line, the field amplitude on the detector plane can be written as

$$E(u, n) \approx K[\tilde{F}_n(u) * B(u)] \quad (IV.2.2)$$

where  $K$  is a scaling factor. For a camera looking at a tilted grating image with a spatial frequency  $u_0$  in the  $x$  coordinate direction (fast temporal variation) and frequency  $v_0$  in the  $y$  (slow) direction,

$$f_n(x) = \cos[2\pi u_0(x + n\phi)]$$

$$u_0 \geq \frac{1}{vT_v}$$

$$v_0 \leq \frac{1}{2vT_v}$$

$$\phi = vT_v \frac{v_0}{u_0}$$

where  $T_v$  is the video line time. In this mode of system operation, the laser diode pulsing rate should be set equal to the video line rate.i.e.  $T = T_v$  For example, if we have a grating with variation only in the  $x$  direction, ( $v_0 = 0$ ), from equation (IV.2.2) we get

$$E(u, n) = K[B(u - u_0) + B(u + u_0)] \quad (IV.2.3)$$

and for a variation only in the  $y$  direction of the image,

$$E(u, n) \approx KB(u)\cos(2\pi v_0 nX) \quad (IV.2.4)$$

$$X = vT$$

From equation (IV.2.3) it is clear that the fast spatial frequency variations along the  $x$  direction of an image can be resolved in the Fourier plane by using an acousto-optic device as an input transducer and a Fourier transforming lens to spatially channelize these fast frequencies into coarse frequency bins. Equation (IV.2.4) tells us that spatial variations of frequency  $v_0$  along the  $y$  direction in the image are converted by the pulsing space integrating acousto-optic spectrum analyzer to a sampled temporal variation of the same frequency in a coarse frequency bin. This temporal variation can then be channelized into its fine frequency bins along the  $y$  direction by using the DFT algorithm based spatially distributed time integrating modules generated by using imaging optics and a CCD detector array. Figure IV.2.4 shows the grating video images.

### IV.3 Time Integrating Spectrum Analyzer Experiment

We have used the DFT Algorithm approach to time spectrum processing<sup>4</sup>. The DFT algorithm is described by

$$S(k) = \sum_{n=0}^{N-1} s(n)W_N^{nk}$$

$$W_N = e^{-j\frac{2\pi}{N}}$$

where  $S(k)$  is the 1-D Fourier spectrum of the input signal  $s(n)$ . This operation can be broken up into a summation over  $n$  of the products of the input signal samples with its corresponding DFT matrix columns. As the DFT matrix is symmetric, we require only half the terms in a DFT column. The analog nature of each column is sinusoidal with a half cycle increase with each increasing DFT column. The DFT matrix represented as a 1-D signal is a stepped frequency chirp signal that can be written as

$$d(t) = \sum_{n=0}^{N-1} \cos[n\Delta\omega(t - nT)] \text{rect}\left[\frac{t - nT}{T}\right] \quad (IV.3.1)$$

We used a personal computer to generate the DFT signal. The DFT mask and the half cycle step behavior are shown in Figure IV.3.1. This method calculates the Cosine transform i.e. the real part of the Complex Fourier Spectrum. The spectrum analysis is performed along the length of the DFT column which acts as a spatially distributed local oscillator (DLO) in time. The frequency of the oscillators increases from the top (DC) of the column to the bottom (half the Nyquist sampling frequency). If one of the input signal frequencies coincides with one of the DLO beads, it beats with it to build up an interference peak at the location of that DLO bead. In this way, the frequency components of the input signal are resolved into the fine frequency bins along the DFT column ( $y$ ) direction. Figure IV.3.2 shows the optical system set up in the laboratory. The laser diode is pulsed at the video line rate and the input signal  $s(t)$  into the Bragg cell is

$$s(t) = \cos[(\omega_0 + \delta)t] + d(t)\cos\omega_0 t$$

where  $\omega_0$  is the center frequency of the Bragg cell. The signal  $s(t)$  is imaged on to the CCD via the +1 diffracted order light from the Bragg cell with appropriate single sideband filtering done in the Fourier plane of cylindrical lens  $C_2$ . The light intensity integrated on the CCD is

$$I(y) = \sum_{n=0}^{N-1} \left| e^{-j(\omega_0 + \delta)(nT - \frac{y}{v})} + \frac{1}{4} e^{-j[\omega_0(nT - \frac{y}{v}) + n\frac{\Delta\omega}{v}y]} \right|^2$$

$$I(y) \approx C + \cos\left(\frac{\omega_s}{v}y + \beta\right) \frac{\sin(N\alpha)}{\sin\alpha}$$

where

$$\alpha = \frac{1}{2}\left(\delta T - \frac{\Delta\omega}{v}y\right)$$

$\omega_s$  and  $\beta$  are signal dependent spatial frequency and phase terms and  $C$  is constant bias term. Typical value for  $\omega_s$  is  $\approx 1.86$  cycles per mm which gives only a few cycles on the CCD surface giving a very low modulation. Therefore, we see peaks located at the sinc type function maximum position  $y = \frac{vT}{\Delta\omega}$  corresponding to the signal fine frequency  $\delta$ . In our experiment,  $\delta$  is varied from DC to 7.8 KHz which corresponds to the bandwidth of a video image along its vertical ( $y$ ) or slower direction. Figure IV.3.3 shows the experimental results without bias removal. The peak moves along the imaged DFT signal ridge with changing fine frequency.

#### IV.4 Architectures for TSI Spectrum Analysis

Figures IV.4.1 and IV.4.2 show two possible TSI architectures for spectrum analysis using crossed Bragg cells, imaging optics, a pulsing laser diode, CCD detector array and supplementary electronics. The general signal chain for both systems is as follows. The DFT signal  $d(t)$  added to a reference bias  $a$  is mixed up to the center frequency  $\omega_0$  of the Bragg cell before being used as input to the acousto-optic device. This composite signal  $s_1(t)$  is then imaged on to the CCD plane with appropriate single sideband spatial filtering. In the other orthogonal Bragg cell, we enter the sum of a reference chirp  $c(t)$  with the information signal  $v(t)$  (eg. video, tones) that has been mixed to the Bragg cell center frequency. A lens takes the Fourier transform of the signal  $s_2(t)$  in the AO device and this spectrum is made to coincide with the detector plane. The electric field incident on the CCD detector plane is

$$E = \left[ \int_A \tilde{s}_1\left(t - \frac{x}{v}\right) e^{-j2\pi ux} dx \right] \left[ \tilde{s}_2\left(t + \frac{y}{v}\right) \right]$$

where

$$s_1(t) = [v(t) + c(t)] \cos \omega_0 t$$

$$s_2(t) = [a + d(t)] \cos \omega_0 t$$

$$v(t) = \sum_{n=0}^{n=N-1} f_n(t - nT) \text{rect}\left(\frac{t - nT}{T}\right)$$

for a video signal.

$$c(t) = \sum_{n=0}^{n=N-1} \cos[b(t - nT)^2] \text{rect}\left(\frac{t - nT}{T}\right)$$

and  $d(t)$  is defined by IV.3.1. Taking into account the pulsing of the laser diode ( $\delta(t - nT)$ ) and the single sideband filtering, we get the intensity on the  $n$ th pulse as

$$|E_n|^2 \approx \left| [v(\tilde{F}_n(vu) + \tilde{C}(vu)) * \text{Asinc} Au] [a + e^{-jn \frac{\Delta\omega}{v} y}] \right|^2 \quad (IV.4.1)$$

On expanding equation (IV.4.1) (see appendix A), and collecting similar terms, we get the total time integrated interferometrically generated charge distribution recorded on the



CCD after a frame time to be given by

$$I(u, y) = K \operatorname{Re} \left[ \sum_{n=0}^{n=N-1} (\tilde{F}_n(u) * B(u)) \cos(n \frac{\Delta\omega}{v} y) \right] + K_1 + K_2 \quad (1v.4.2)$$

where the first term gives the 2-D Cosine transform of the input signal and  $K_1$  and  $K_2$  represent constant bias and signal dependent bias terms respectively.  $K$  is a scaling constant and we have assumed that the reference chirp spectrum is uniform over the bandwidth of the information signal. The general blurr spot  $B(u)$  has been used in the analysis. For a continuous time signal as input, the first term of equation (IV.4.1) represents the folded spectrum of the input. On the other hand, for a video signal input, it gives the 2-D video image spectrum. See appendix A for the impulse response of the system corresponding to the two types of input. The architecture in figure IV.4.1 although analytically sound has two important practical limitations. In order to achieve high spectral resolution using present day hardware .i.e.AOD's, CCD's, the focal length of the imaging lenses runs into meters. Secondly, for ideal operation the single sideband filtering has to be done in the plane of the second Bragg cell which is not possible because of the thickness of the crystal and its support casing. The architecture in figure IV.4.2 solves both these problems by using crossed cylinders for imaging. This imaging method gives lens values that assure overall short system length and desired demagnifications for compatibility with the CCD detector specifications. In our case, we used 10 cm and 15 cm cylindrical lenses to achieve the desired demagnifications.

Figure IV.4.3 shows the laboratory setup of the architecture in Figure IV.4.2. The system timing is controlled by the CCD detector 7.16 MHz internal oscillator. The CCD blanking signal is used to generate a 15.734 KHz laser diode trigger signal with a pulse width of 100 nsec. This corresponds to a light flash every video line time. The anamorphic gaussian beam profile of the laser diode is collimated by the spherical lens such that the long axis is along the x direction of the SI AOD aperture. The Bragg diffracted light from the first AOD is Fourier transformed by a spherical lens in the x direction and recollimated in the y direction giving a slit of light positioned in the aperture of the second AOD. The Bragg diffracted light from the second AOD is imaged on to the CCD using the crossed cylinders. In the Fourier plane of the cylinder with power in the y direction, the appropriate spatial single sideband filtering is done. The AOD's used in this experiment are slow shear mode Telirium Oxide devices with an aperture time of 70  $\mu$ sec and bandwidth of 40 MHz. A 60 MHz center frequency is used for the AOD's. The reference chirp is stored in a digitally programmable read only memory (PROM) and read out each laser diode trigger pulse using the CCD pixel clock and a digital-to-analog converter. Figure IV.4.4 shows a reference chirp oscilloscope trace that was used in the experiments. The chirp, being digitally generated is perfectly coherent at every laser diode pulse. The DFT signal is generated by an IBM-PC image processing work station that is locked to the CCD detector clock. For video signal inputs, the CCD camera is locked to the CCD detector array by using special synchronizing circuitry. For folded spectrum processing of tones, the laser diode trigger frequency is adjusted according to the Nyquist criteria.

Experimental results from this processor are shown in figures IV.4.5 and IV.4.6 for a fine frequency analysis bandwidth of 7.86 KHz. The processor is operated with a coarse frequency resolution of 80 KHz per pixel. Data in figure IV.4.5 corresponds to a fine frequency variation from DC to 7.8 KHz with a zero coarse frequency variation. We see the interference peak move from left(DC) to right(7.86 KHz) along the DC coarse frequency bin. Figure IV.4.6(a) shows the 2-D folded spectrum of a single tone input where the position of the peak gives the coarse and fine frequencies. Coarse DC position corresponds to the base of the picture. Figure IV.4.6(b) shows the 2-D video spectrum of a tilted grating used as the video image. The DC of the fast (coarse) variation along the x direction of the image corresponds to the central bin between the two peaks on the picture. The slow (fine) variation along the y direction of the image corresponds to the left to right movement of the peak along each fast frequency bin. We get two peaks instead of one because the video signal is mixed with 60 MHz before entering the Bragg cell giving an amplitude modulated signal whose spectrum has two sidebands located symmetrically around the 60 MHz carrier frequency. The single tone experiments are carried out using a signal generator whose frequency is varied around 60 MHz. The 2-D results correspond to spectrums after electronic bias subtraction.

#### IV.5 Bias Removal Techniques

Bias separation from the desired signal is always an important issue in interferometric time integrating processors. We discuss three ways in which the bias can be removed. Pixel by pixel electronic bias subtraction can be done by using two synchronously operated CCD's, one to record the signal plus bias terms and the other for recording bias terms. In our experiments, we used a PC based image processing work station with a frame grabber to store the bias for subtraction. Another approach is to place the desired signal on a spatial carrier which is converted to a temporal variation by the natural readout mechanism of the CCD and then bandpass filtered by appropriate electronics. In the TSI processor, the 2-D spectrum can be placed on a spatial carrier by mixing the DFT signal by an frequency offsetted Bragg cell center frequency signal eg. 60.1 MHz and using a time delayed reference chirp signal. The bias subtraction and carrier demodulation methods of bias removal do not solve the problem of limited system dynamic range as processing is done after the detection of the signal. The effective system dynamic range at the output is

$$DR_s = DR \left[ \frac{SBR}{(1 + SBR)} \right]$$

where  $DR$  is the dynamic range of the output detector (CCD) and  $SBR$  is the signal to bias ratio on the detector. In most TI systems,  $SBR$  is much less than one. One way of solving this dynamic range problem is using a photorefractive crystal for bias removal<sup>5</sup>. The desired spectrum is generated on a spatial carrier along the crystal side and is read out by a Bragg matched beam. The possible architecture for the TSI spectrum analyzer using a photorefractive crystal is shown in figure IV.5.1. This architecture has definite attractions such as higher light efficiency, better system dynamic range and no reference chirp requirement in the signal chain. In addition, the single sideband filtering does not

have to be done in the Bragg cell aperture and this system can process higher space-bandwidth signals as the resolution of the photorefractive crystal is much greater than that of the CCD detector. As this system is not common path, it is more sensitive to jitter.

#### **IV.6 Processor Performance Issues**

The Caltech processor shown in figure IV.4.3 achieved coarse and fine frequency resolutions of 80 KHz and 100 Hz respectively. The number of coarse and fine frequency resolution bins corresponded to 384 and 491 respectively. The bandwidth of the system is controlled by the bandwidth of the reference chirp which is programmed in a high speed PROM to 5 MHz for video signal inputs. Modulation depths of 30 percent were obtained. The Caltech processor performance is limited by nonuniformities in the reference chirp spectrum due to inhouse electronics, the limited temporal coherence of the high power hitachi laser diode and intermodulation product terms resulting from AOD and amplifier nonlinearities. The coarse frequency resolution is limited by CCD pixel size, focal length of Fourier transforming lens, AO cell aperture and apodization effects. For the video processor, the ideal coarse frequency resolution of 15.7 KHz could be obtained by using a larger focal length lens and smaller CCD pixels. The fine frequency resolution is limited by integration time of the CCD which corresponds to 60 Hz. Note that using carrier demodulation for bias removal reduces the number of frequency bins along the carrier direction. For using a photorefractive crystal such as Bismuth Silicon Oxide (BSO) for bias removal in our proposed architecture we need around 8 W pulsed or 12.3 mW continuous power to record gratings with an Argon laser beam <sup>5</sup>. This high power requirement can be reduced for test purposes if we wait a few video frames before reading the integrated spectrum on the crystal using the Helium-Neon readout beam. The principle of operation involves the coherent addition of the image spectrum over successive video frames to build up enough charge density for recording gratings on the crystal. Another important issue to note is that in a multi-tone signal input environment, the TSI processor will not introduce crosstalk because each tone is spatially separated in the Fourier plane thus giving cross terms that have negligible contributions.

## Appendix

This appendix gives the derivation of equation IV.4.2 starting with equation IV.4.1 given earlier. For simplicity of the analysis, we have assumed the  $u = 0$  axis to correspond to the position of the Bragg cell center frequency ( $\omega_0$ ) on the CCD plane. The intensity on the  $n$ th pulse given in equation IV.4.1 can be written as

$$I_n = |(S + C)(a + d)|^2 \quad (1)$$

where ' $S$ ' and ' $C$ ' are Fourier spectrums of the information signal and reference chirps respectively taken by the space integrating Bragg cell spectrum analyzer and ' $a$ ' and ' $d$ ' are the reference bias signal and the spatially filtered and heterodyned to baseband DFT signal respectively. ' $a$ ' is a real quantity and ' $d$ ' is given by

$$d = e^{-jn \frac{\Delta\omega}{v} y}$$

$$|d|^2 = 1$$

Using the above relations and expanding equation (1) we get

$$\begin{aligned} I_n = & 2\text{Re}[aSC^* \text{Re}(d)] + (1 + a^2)|C|^2 + 2|C|^2 \text{Re}(ad) \\ & + (1 + a^2)|S|^2 + 2|S|^2 \text{Re}(ad) + 2(1 + a^2)\text{Re}(SC^*) \end{aligned} \quad (2)$$

Note that the reference chirp is a perfectly coherent chirp with no dependence on  $n$  as the same digital chirp is generated every laser diode pulse.  $\text{Re}$  in equation (2) stands for real value of a function. Equation (2) consists of 6 terms where the first term gives the 2-D spectrum, the second and third terms give the constant bias term and finally the fourth, fifth and sixth terms give the signal dependent bias term. Assuming the reference chirp spectrum  $C$  is uniform over the information signal bandwidth and has an arbitrary fixed phase which can be taken to be zero for simplicity of analysis, we can write  $C = C_0$  where  $C_0$  is a constant. Now taking the summation over all the  $N$  laser diode pulses to find the charge distribution on the CCD, the first term in equation (2) gives

$$I_1 = 2aC_0 \text{Re} \left[ \sum_{n=0}^{n=N-1} S \text{Re}(d) \right] \quad (3)$$

Substituting in equation (3) the value of  $S$  for a video signal and the value of  $d$ , we get the desired 2-D spectrum

$$I_1(u, y) = K \text{Re} \left[ \sum_{n=0}^{n=N-1} (\hat{F}_n(u) * B(u)) \cos\left(\frac{n\Delta\omega}{v} y\right) \right] \quad (4)$$

where  $K$  is a constant term involving the constant terms  $C_0$  and  $a$  and the finite size of the CCD detector array in the  $u$  and  $y$  directions. We have used the generalized blurr spot

$B(u)$  to account for the finite aperture of the Bragg cell in the SI direction. The second and third terms of equation (2) on summation give the constant bias term  $K_1$  to be

$$K_1 = NC_0^2(1 + a^2) + 2aC_0^2 \cos(\alpha y) \frac{\sin(N\beta y)}{\sin(\beta y)} \quad (5)$$

$$\alpha = (N - 1) \frac{\Delta\omega}{2v}$$

$$\beta = \frac{\Delta\omega}{2v}$$

where the first term in equation (5) gives a constant bias level and the second term gives a fine frequency DC ridge along  $y = 0$  with a very slow spatial modulation undetectable by the CCD. Now taking the summation over  $n$  of the fourth, fifth and sixth terms in equation (2), we get the signal dependent bias term  $K_2$  as

$$K_2 = N(1 + a^2)|S(u)|^2 + 2a|S(u)|^2 \cos(\alpha y) \frac{\sin(N\beta y)}{\sin(\beta y)} + 2C_0(1 + a^2)|S(u)|a_1 \quad (6)$$

Note that the absolute value operation on  $S(u, n)$  in equation (2) removes the time dependence in the spatial Fourier transform taken by the lens giving only the coarse frequency bias ridge terms in equation (6). The first and third terms in equation (6) give bias terms positioned at the signal coarse frequency ridges. The constant  $a_1$  depends on the fine frequency of the signal. The second term gives the coarse frequency ridge crossed with the fine frequency DC ridge. Combining the results from equations (4), (5) and (6) we get the total time integrated charge distribution on the CCD to be

$$I(u, y) = K \operatorname{Re} \left[ \sum_{n=0}^{n=N-1} (\tilde{F}_n(u) * B(u)) \cos(n \frac{\Delta\omega}{v} y) \right] + K_1 + K_2 \quad (7)$$

The impulse response of the system for a video image input with a spatial frequency  $u_0$  in the x-direction and spatial frequency  $v_0$  in the y-direction of the image is

$$I_1 \approx \cos(\eta) \frac{\sin(N\gamma)}{\sin(\gamma)} [B(u - u_0) + B(u + u_0)] \quad (8)$$

$$\eta = (N - 1)\gamma \approx \pi v_0 X (N - 1)$$

$$\gamma = \pi v_0 X - \frac{\Delta\omega}{2v} y$$

where we used the fact that the modulation along  $y$  is slow. We will get two peaks positioned at the coordinates  $u = u_0, y = 2\pi v_0 \frac{Xv}{\Delta\omega}$  and  $u = -u_0, y = 2\pi v_0 \frac{Xv}{\Delta\omega}$ .

For a single tone input signal with  $f_c$  and  $f_f$  the coarse and fine frequencies respectively, we get the impulse response of the system as

$$I_1 \approx \cos(\xi) \frac{\sin(N\xi)}{\sin(\xi)} B(u - \frac{f_c}{v}) \quad (9)$$

$$\xi = \pi f_f T + \frac{\Delta\omega}{v} y$$

This time we get one peak located at  $u = \frac{f_c}{v}, y = \pi f_f T \frac{v}{\Delta\omega}$  where  $\xi$  is a fine frequency dependent constant phase term.

### References

- [1] D. Psaltis and D. Casasent, "Time and Space Integrating Spectrum Analyzer," *Applied Optics*, vol. 18, p. 3203, 1979.
- [2] K. Wagner and D. Psaltis, "Time and Space Integrating Acousto-optic Folded Spectrum Processing for SETI," *Proc SPIE*, Vol 564-31, 1985.
- [3] C. E. Thomas, "Optical Spectrum Analysis of Large Space Bandwidth Signals," *Applied Optics*, vol. 5, p. 1782, 1966.
- [4] K. Wagner, "Time and Space Integrating Acousto-optic Signal Processing," Ph.D Thesis, California Institute of Technology, May 1987.
- [5] D. Psaltis, J. Yu and J. Hong, "Bias-free Time Integrating Optical Correlator using a Photorefractive Crystal," *Applied Optics*, vol. 24, No.22, Nov 1985.

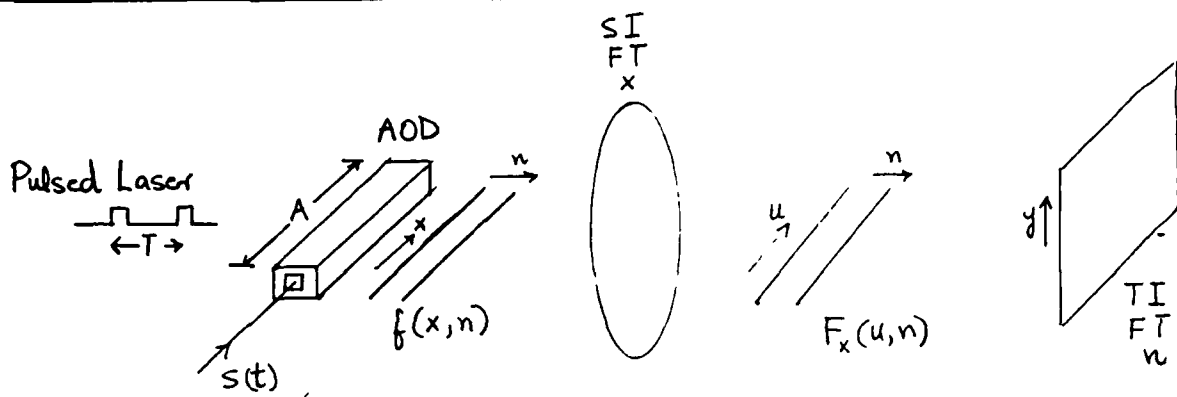


Figure IV.1.1

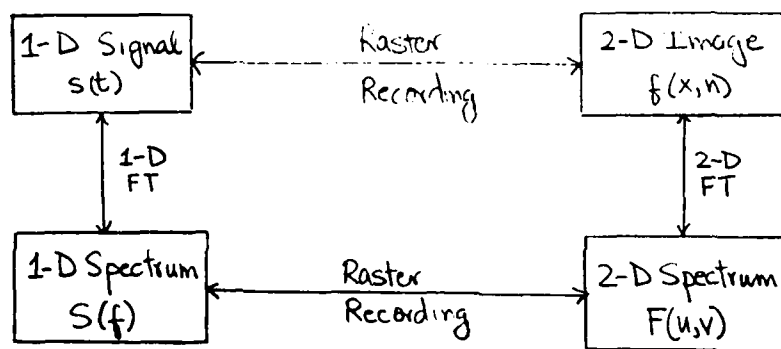


Figure IV.1.2

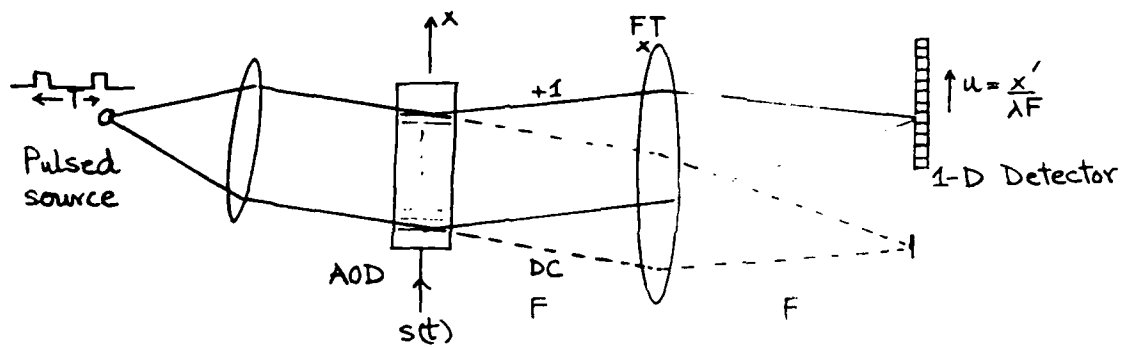


Figure IV.2.1

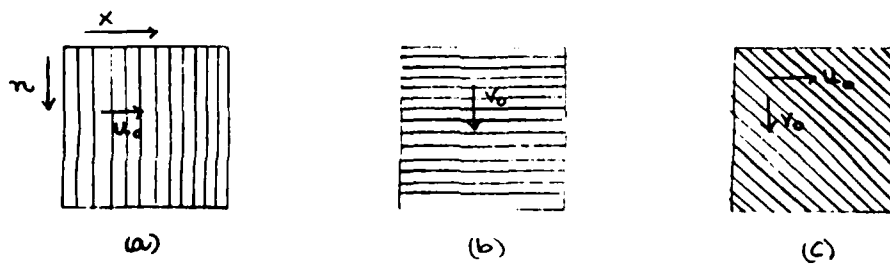
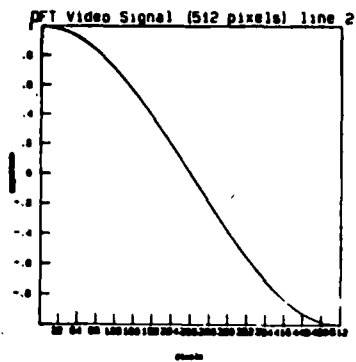
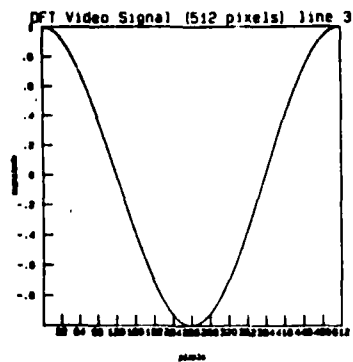


Figure IV.2.2



(a)



(b)



(c)

Figure IV.3.1



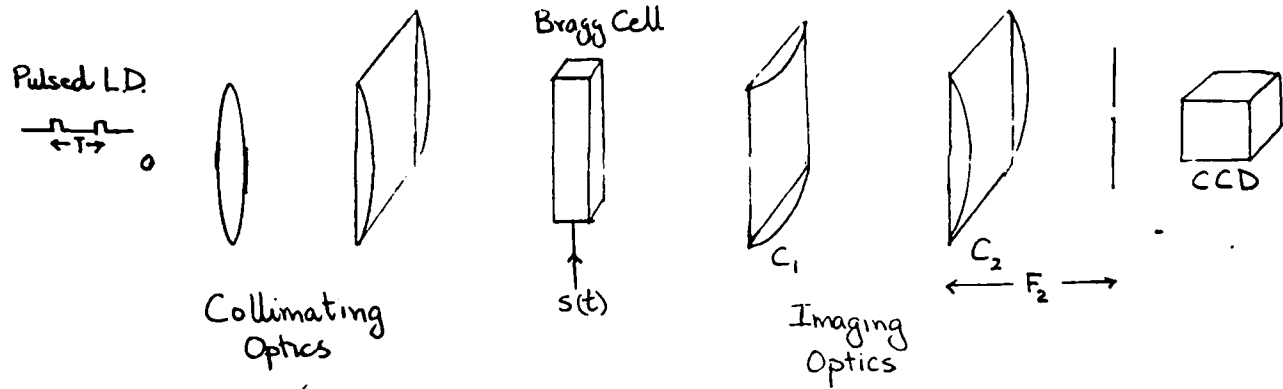


Figure IV.3.2

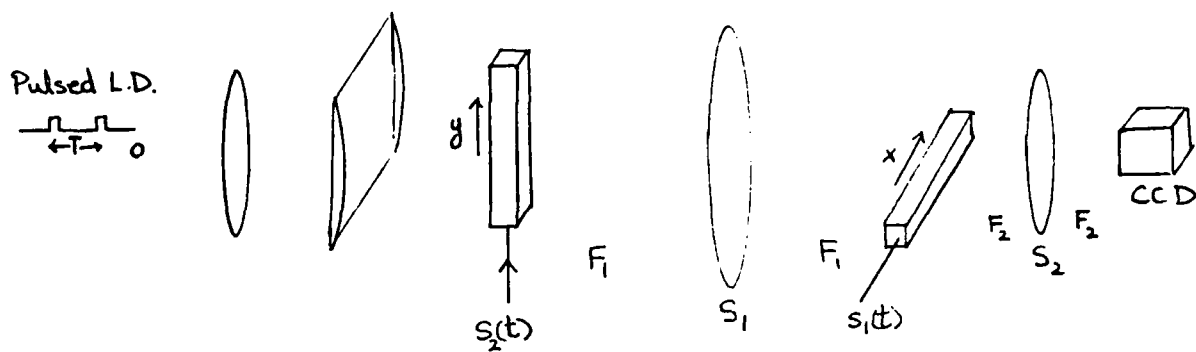
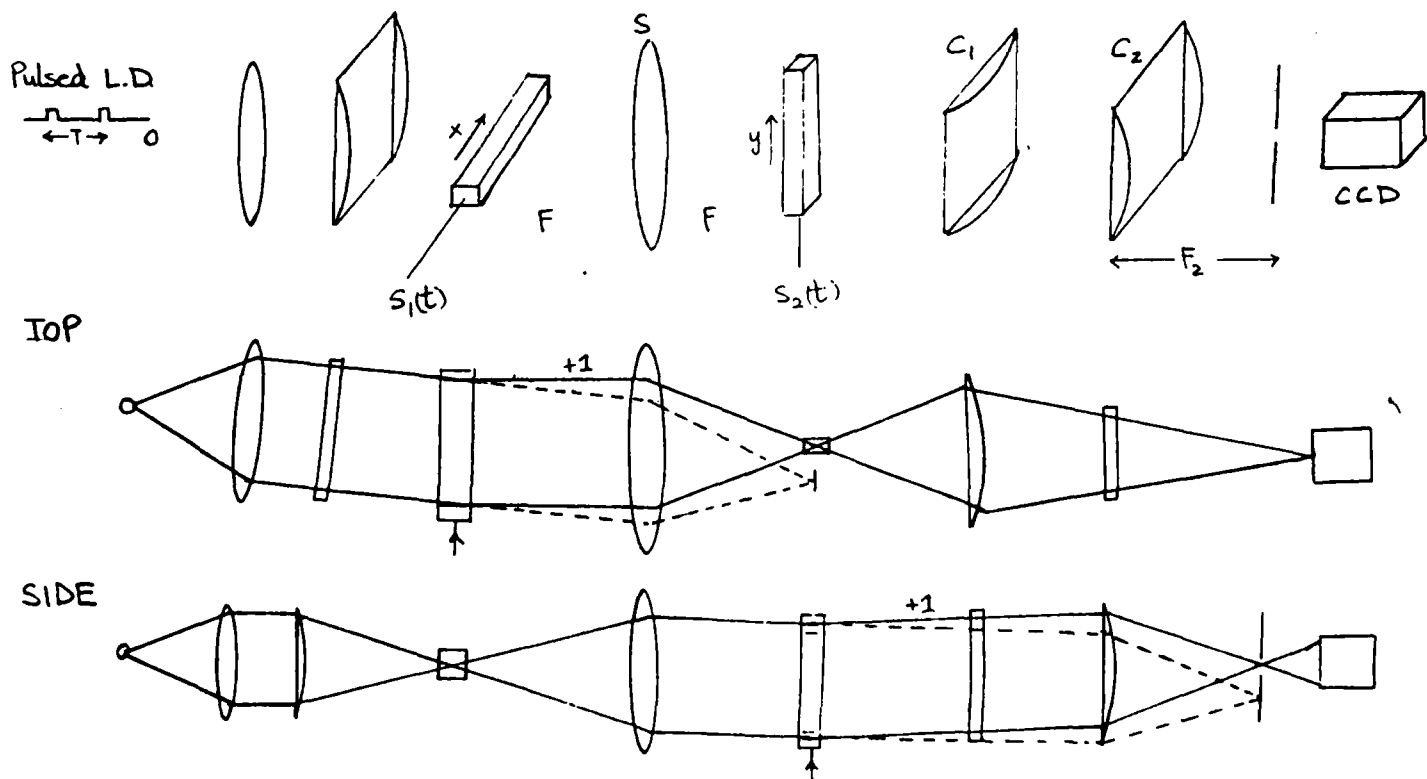
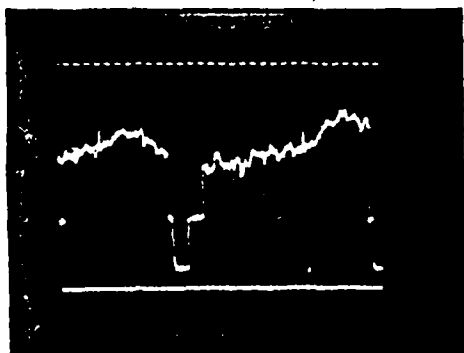


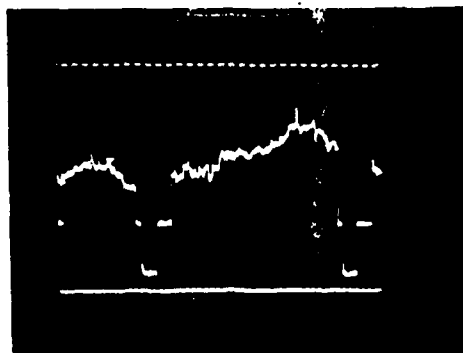
Figure IV.4.1

Figure IV.4.2

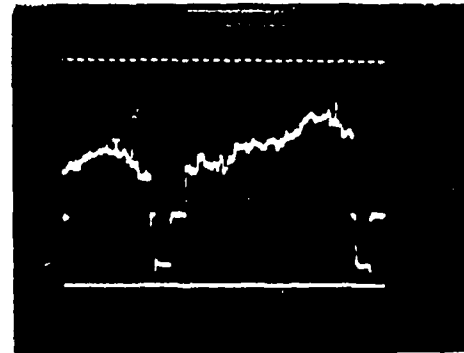




5.272 KHz



6.0678 KHz



7.0573 KHz

Figure IV.3.3

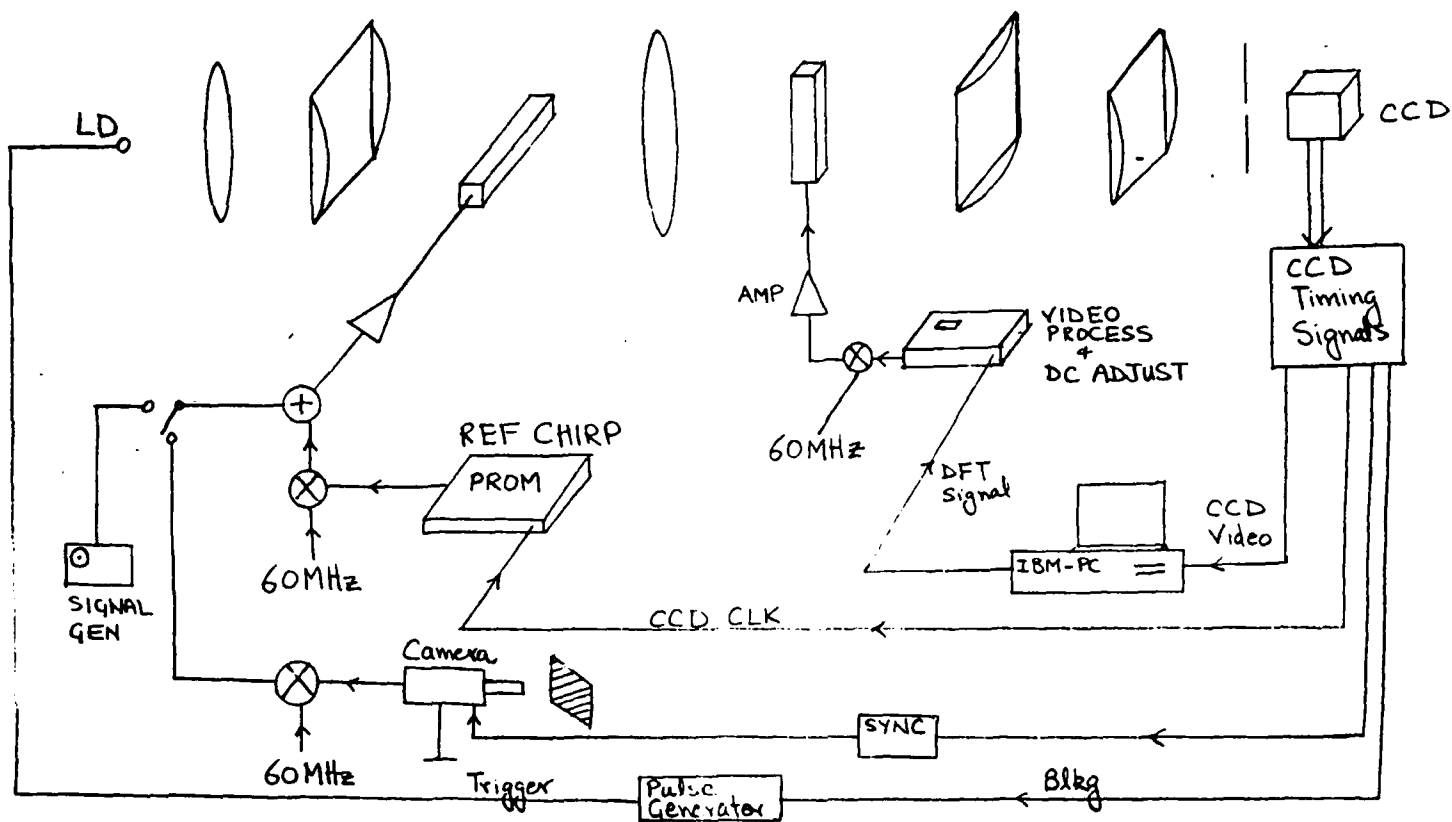


Figure IV.4.3

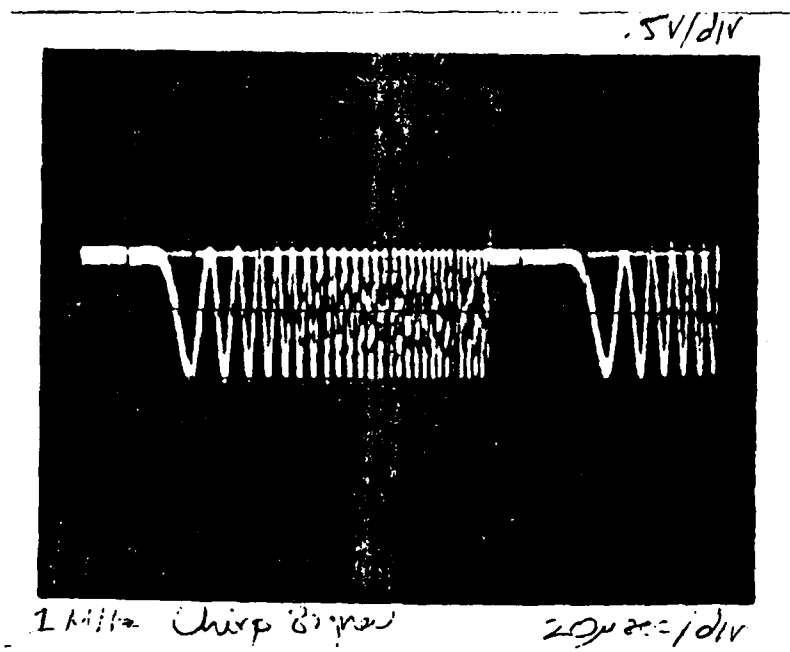


Figure IV.4.4

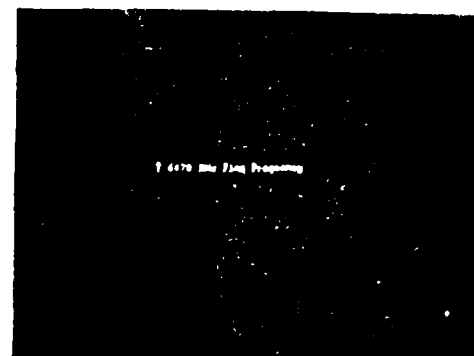
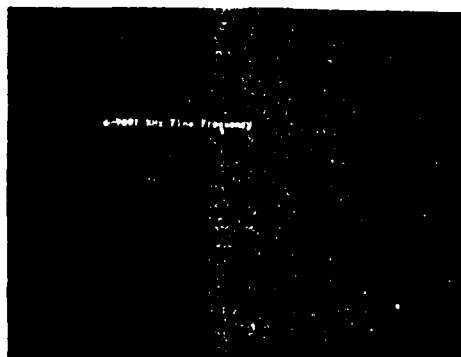
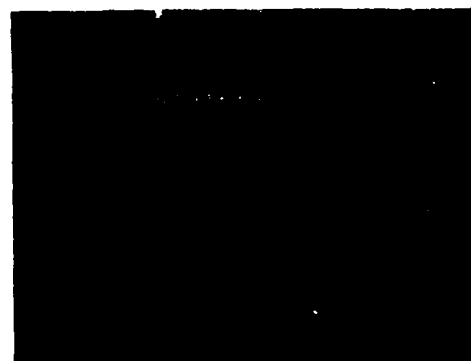
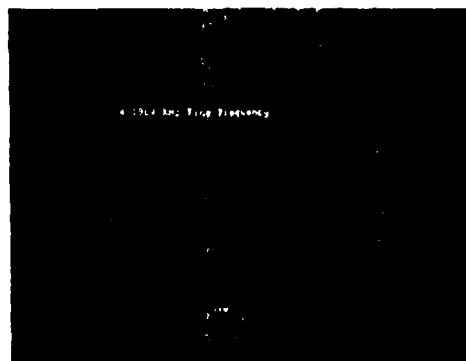
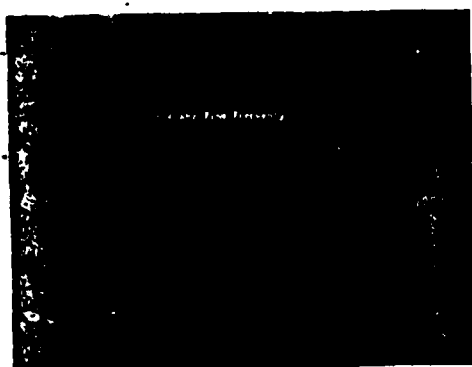


Figure IV.4.5



Figure IV.4.6

(a)

(b)



## V. Adaptive Broadband Array Processing

### V.0 Introduction

Adaptive signal processing techniques for processing broadband phased arrays are presented. After discussing the essential differences between narrowband arrays and broadband arrays, optimal forms for the broadband space-time filters are derived. Adaptive processing systems which converge to the optimal forms are then presented. Acousto-optic implementations using multi-channel acousto-optic devices are presented. One particular implementation makes use of a photorefractive crystal as a time-integrating detector [11,12].

### V.1 Narrowband Processors in Broadband Environments

The extension of adaptive filtering techniques to the space-time domain is applicable for sonar and radar signal processing where the outputs from an array of sensors must be weighted and summed to optimally estimate a signal in the presence of noise [1-3]. When the array processor encounters only narrowband signals centered at a common carrier frequency,  $f_0$ , the filter structure shown in Fig. V.1 is identical to that of the temporal filter except that the input samples are the outputs of the sensors instead of a tapped delay line. In such applications, only spatial discrimination of signals is required, and the jammer nulling capabilities of such systems are quite good as long as the jammers are narrowband. The output can be described by the following equation

$$z(t) = \sum_{n=1}^N h_n u_n(t), \quad (V.1)$$

where  $N$  is the number of elements in the array and  $h_n$  is the adaptively controlled weight for the  $n_{th}$  sensor output  $u_n(t)$ .

After suppressing the temporal carrier term  $\exp\{j2\pi f_0 t\}$ , the signal received by the  $n_{th}$  element due to a narrowband signal arriving at an angle  $\theta$  from boresight can be expressed as

$$u_n(t) = a(t) \exp\{ -j2\pi f_0 \sin\theta nd/c \}, \quad (V.2)$$

where  $c$  is the speed of light,  $a(t)$  is the slowly varying envelope of the signal, and  $d$  is the spacing between the array elements. The goal of the adaptation is the minimization of the mean squared error between the actual output of the processor and a desired signal. The scenario with which we will be concerned is the one where the desired signal is known to be on boresight, and interference from directions other than this must be suppressed. This is sometimes known as *sidelobe cancellation* [4]. An example of narrowband nulling is shown in Fig. V.2, where the array gain pattern for a uniformly weighted array and the

minimum mean-squared error gain pattern for receiving a signal on boresight and rejecting a jammer of the same frequency at a sidelobe angle are plotted.

Although the jammer is received at a sidelobe angle and is attenuated relative to the signal, the power of the jamming interferences is typically much larger than that of the signal, and so the summed output of the uniformly weighted processor will be dominated by the interference. In this case, the optimum pattern to which the adaptive processor converges places a perfect null precisely at the direction of the interference.

Given the size of the array ( $N$  = the number of receiving elements), an upper bound on the number of spatial jammers of the same frequency  $f_0$  that the array is able to reject can be established. The  $m_{th}$  jammer from a set of  $M$  jammers can be represented by an  $N$ -element vector  $\underline{u}^{(m)}$  whose  $n_{th}$  element is given by

$$u_n^{(m)} = \exp\{-j2\pi f_0 \sin\theta_m n d/c\}. \quad (V.3)$$

Simultaneous nulling of all of the  $M$  jammers leads to the system of equations

$$\begin{pmatrix} u_1^{(1)} & u_2^{(1)} & \dots & u_N^{(1)} \\ \vdots & \vdots & \ddots & \vdots \\ u_1^{(M)} & u_2^{(M)} & \dots & u_N^{(M)} \\ s_1 & s_2 & \dots & s_N \end{pmatrix} \begin{pmatrix} h_1 \\ h_2 \\ \vdots \\ h_N \end{pmatrix} = \begin{pmatrix} 0 \\ \vdots \\ 0 \\ 1 \end{pmatrix}, \quad (V.4)$$

where  $\underline{s}$  represents the signal vector, and the last equation of the system arises from the constraint that the signal be accepted. If the jammers are distributed spatially such that the vectors  $\{\underline{u}^{(m)}\}_{m=1}^M$  and  $\underline{s}$  are linearly independent, then in order for a solution  $\underline{h}$  to exist, there can be at most  $N$  equations in the system, yielding the upper bound of  $M \leq N - 1$ . The linear independence condition is akin to that of general position in pattern recognition [9] and assures that the jammers are irregularly distributed in space.

Since the narrowband arrays assign only one weight per sensor, no consideration of the temporal content of the received signal is taken. The spatial distinction of a signal is judged based on the observed differences in the phase of the signal as received by each element. If a particular jammer contains many frequencies spread over a significant bandwidth, each component will result in a unique relative phase difference from element to element and hence will look like a multiplicity of jammers directed at different angles. Thus, if a narrowband processor encounters a sufficiently wideband interference in some direction, it will use up all of its degrees of freedom (the adjustable weights) to null this single directional noise.

Two examples are shown in Figs. V.3 and V.4, where the minimum mean-squared error array patterns are plotted for a boresight desired signal and a multi-frequency jammer incident at  $\theta = 60^\circ$ . The element spacing in each case is  $\frac{c}{2f_0}$ . The jamming frequencies are  $f_0$ ,  $.85f_0$ , and  $.7f_0$ , with the signal power and the power in each jamming frequency being equal. For each case (Fig. V.3, Fig. V.4), a gain pattern for each jamming frequency is plotted, since the array response is frequency dependent. Fig. V.3 depicts the response of a 2 element array, and it is clear that only the frequency  $.85f_0$  is nulled perfectly, while Fig. V.4, which corresponds to a 4 element array, shows perfect nulling for all three frequencies.



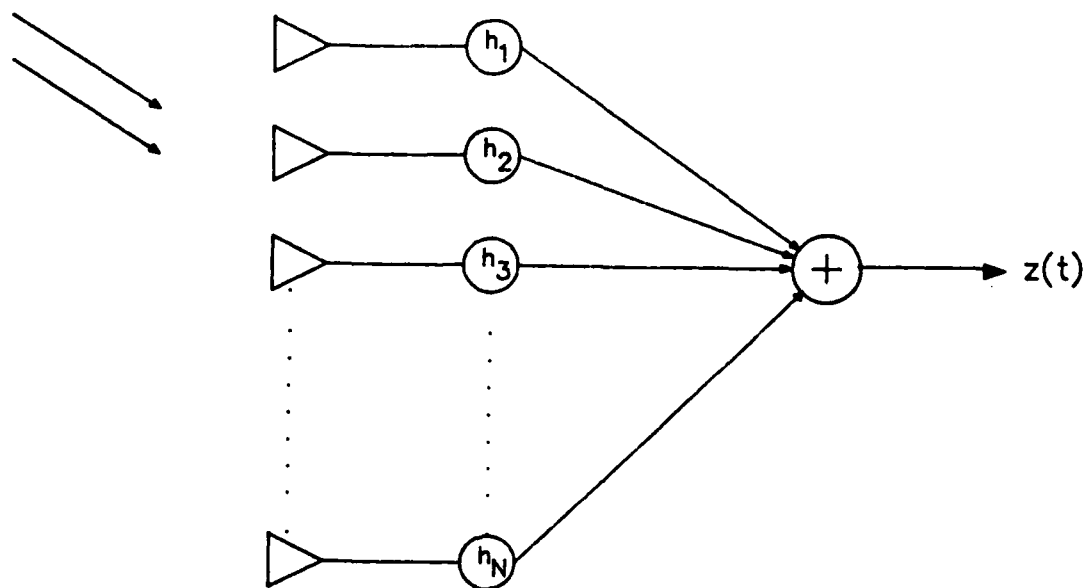


**Fig. V.1** Narrowband Array Processor

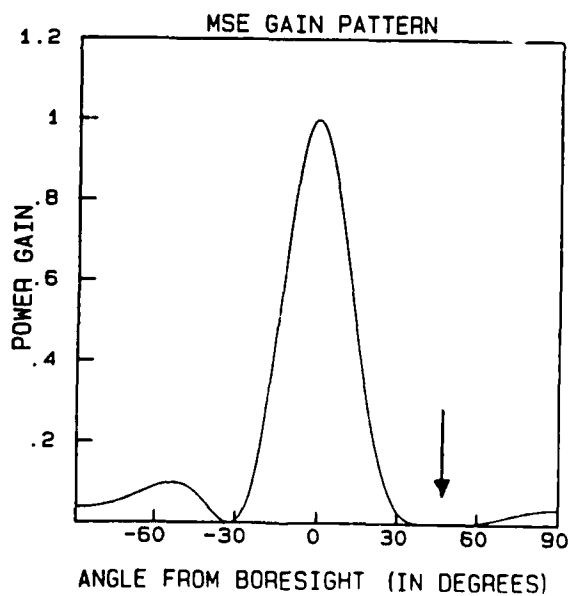
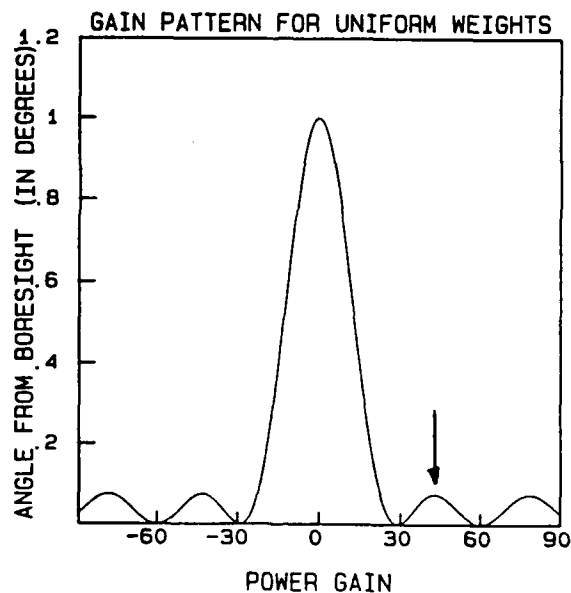


**Fig. V.2** Narrowband Sidelobe Cancellation (arrow indicates the angular position of the jammer): a) uniformly weighted array gain pattern; b) minimum mean squared error array gain pattern (jammer incidence angle is  $50^\circ$ )

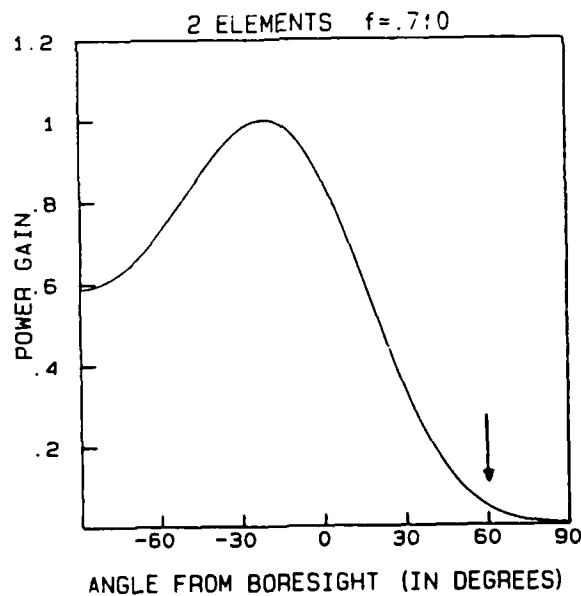
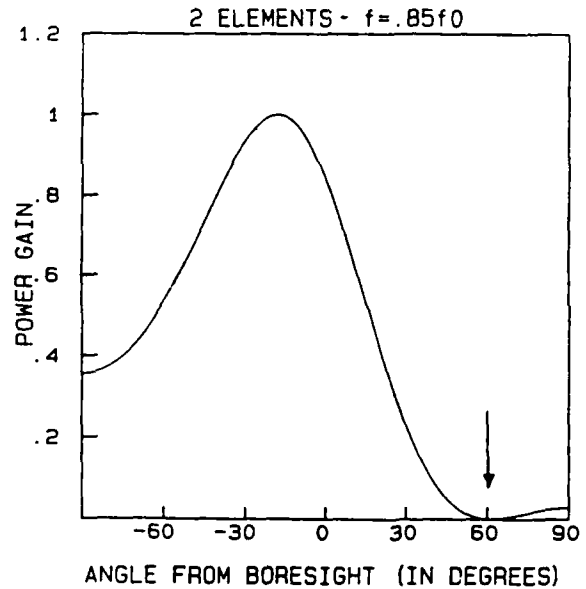
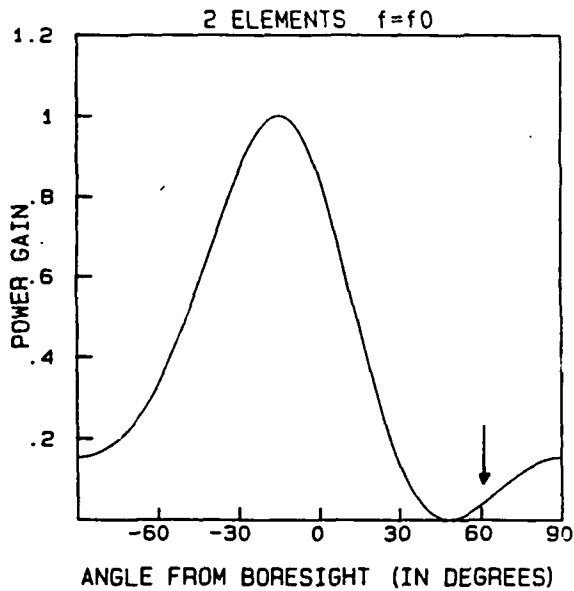


Fig. V.3 Minimum Mean Squared Error Gain Patterns for a Multiple Frequency Jammer ( $f = f_0, .85f_0, .7f_0$ ) Incident at  $60^\circ$  from Boresight (2 element array, element spacing is  $c/2f_0$ ): a) response for  $f_0$ , b) response for  $.85f_0$ , c) response for  $.7f_0$

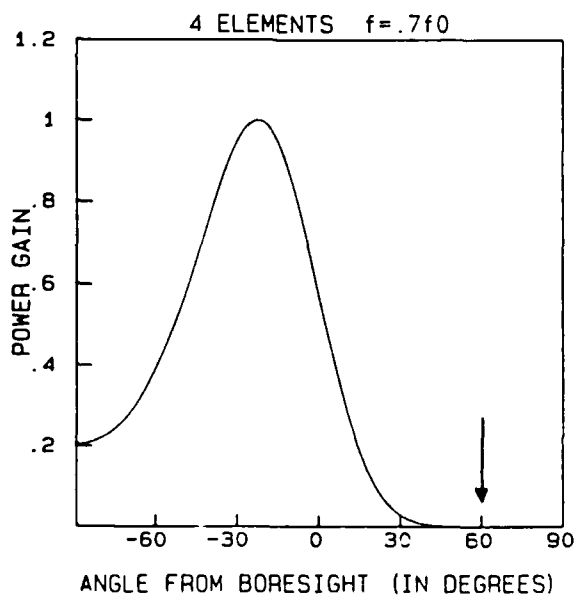
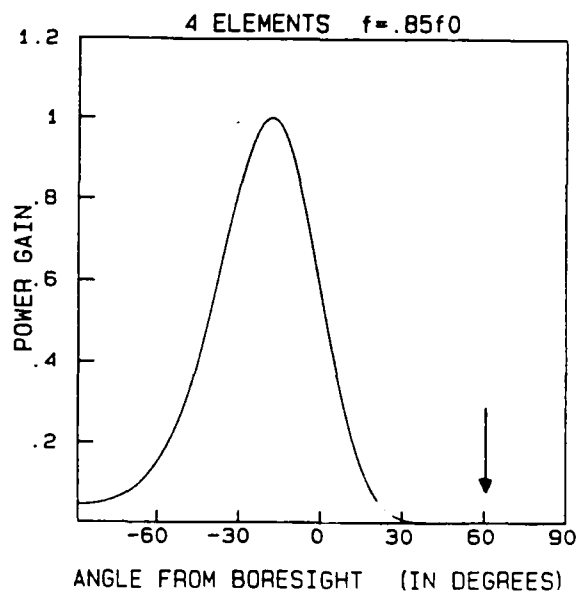
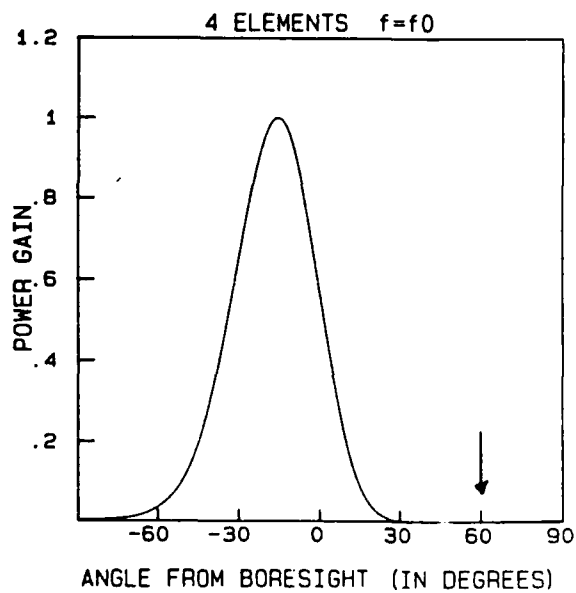


Fig. V.4 Minimum Mean Squared Error Gain Patterns for a Multiple Frequency Jammer ( $f = f_0, .85f_0, .7f_0$ ) Incident at  $60^\circ$  from Boresight (4 element array, element spacing is  $c/2f_0$ ): a) response for  $f_0$ , b) response for  $.85f_0$ , c) response for  $.7f_0$

## V.2 Optimum Broadband Systems

In narrowband applications, bandpass filters are used to assure a narrowband signal and noise environment as shown in Fig. V.1, but where signals with large bandwidths must be processed, such filters cannot be used. Even in broadband noise environments, we would like the  $N$  element array to be capable of cancelling  $N - 1$  jammers in general, regardless of their respective bandwidths. This requires that more degrees of freedom be available for the output of each sensor than the single weight that the narrowband processor provides. Shown in Fig. V.5 is an  $N$  element array processor that satisfies the requirements for operation in broadband environments by passing the output of each sensor through a linear time-invariant filter, or equivalently, a tapped delay line [5-7]. While spatial discrimination is still made possible by the spatial sampling done by the array of sensors, the additional capability of making distinctions based on the temporal content of the received signals is offered by the array of filters.

An optimum choice of the linear filters based on the mean squared error criterion can be made in the present scenario of a desired signal incident on boresight and broadband jammers from other directions. Let  $s(t)$  represent the desired signal which is assumed to derive from a stationary random process with zero mean and autocorrelation function given by  $R(\tau) = E[s(t + \tau)s^*(t)]$ . Since the desired portion of the received signal arrives on boresight, there is no dispersion, and each element receives an identical desired signal  $\alpha s(t)$ . The interference that arrives from different directions will induce signals in each element with different delays.

Let  $v_n(t)$  be the interference component received by the  $n_{th}$  element, assumed also to derive from a zero mean stationary random process with covariance function given by  $\gamma_{mn}(\tau) = E[v_m(t + \tau)v_n^*(t)]$ . The total signal received by the  $n_{th}$  element is therefore given by  $u_n(t) = \alpha s(t) + v_n(t)$ . The output of the array processor is given by

$$z(t) = \sum_{n=1}^N \int_{-\infty}^{\infty} h_n(\tau) u_n(t - \tau) d\tau. \quad (V.5)$$

The problem is to minimize the mean-squared error

$$\epsilon[h_n(\tau)] = E[|z(t) - s(t)|^2], \quad (V.6)$$

by varying the filter kernels  $h_n(\tau)$ . By using simple variational arguments, it is shown in Appendix B that the minimizing solution for  $h_n(\tau)$  must satisfy the system of linear integral equations

$$\sum_{m=1}^N \int_{-\infty}^{\infty} h_m(\tau) [\alpha R(t - \tau) + \gamma_{mn}(t - \tau)] d\tau = R(t), \quad (V.7)$$

where  $n = 1, 2, \dots, N$ . Transformation of the above system to the frequency domain yields

$$\sum_{m=1}^N H_m(f) [\alpha S(f) + \Gamma_{mn}(f)] = S(f). \quad (V.8a)$$

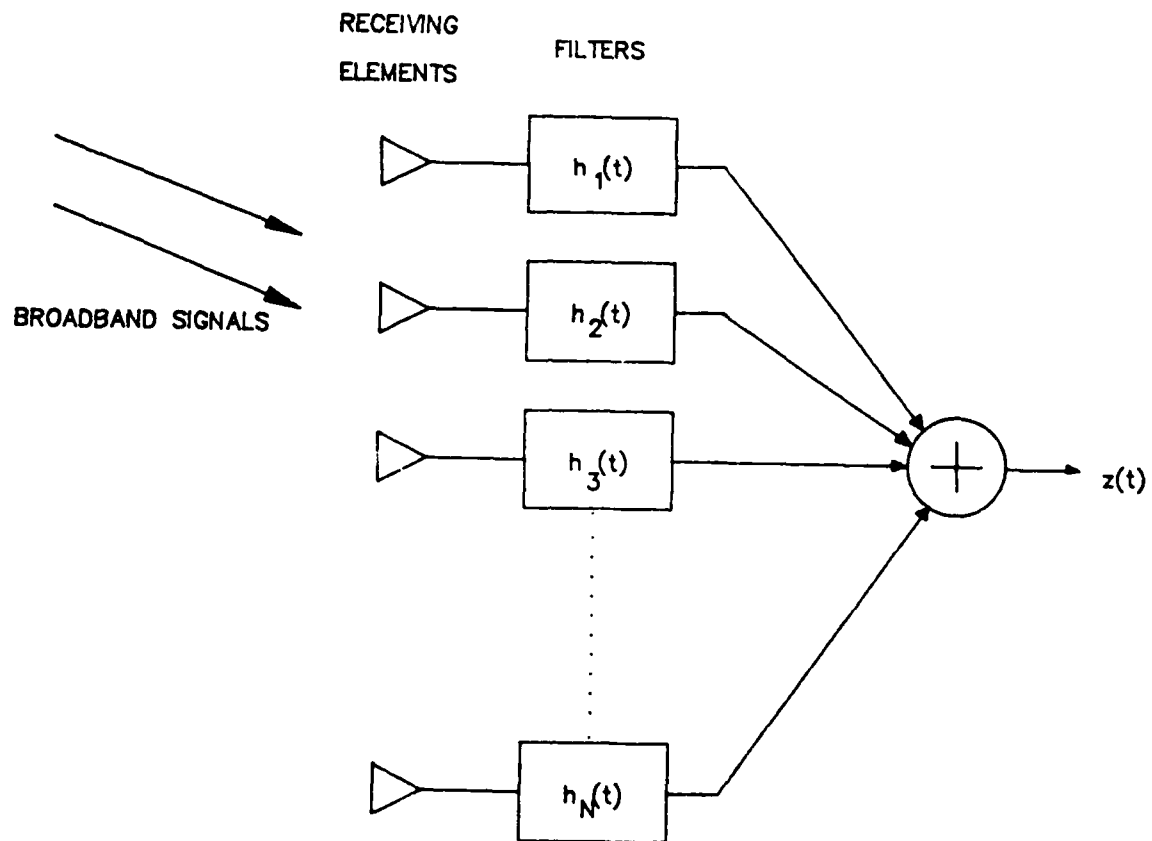


Fig. V.5 Frost's Broadband Array Processor

Here  $S(f)$  is the spectral density function of the signal and  $\Gamma_{mn}(f)$  is the cross-spectral density matrix of the interference, given by the Fourier transforms of the corresponding covariance functions, and  $H_m(f)$  is the frequency response of the  $m_{th}$  filter of the array. For comparison, the corresponding equation for a narrowband processor with a single complex weight  $w_m$  for the  $m_{th}$  receiving element is

$$\sum_{m=1}^N w_m [\alpha + C_{mn}] = 1, \quad \text{for } n = 1, 2, \dots, N, \quad (V.8b)$$

where  $\alpha$  is the amplitude of the received signal component on boresight and  $C_{mn} = E[v_m v_n^*]$ , the covariance matrix of the noise components. A comparison of Eqs. V.8a and V.8b shows that the optimal broadband strategy is to simply provide an optimum narrowband weight for each frequency  $f$ . Thus, the optimum broadband system reduces to a channelized system of optimum narrowband sub-systems.

If we now assume that the signal spectrum is approximately white (e.g., spread spectrum codes) with spectral density  $S_0$  and the received signal component is small compared to the noise so that  $\alpha S_0 \ll 1$ , then Eq. V.8 can be approximated by

$$\sum_{m=1}^N H_m(f) \Gamma_{mn}(f) \approx S_0. \quad (V.9)$$

The frequency-dependent response of the individual filters can now be varied to compensate for the spectral characteristics of the environment, whereas the narrowband processor offered no such flexibility with its single, frequency-independent weight for each sensor.

### V.3 Directional Cancellation of a Single Broadband Interference[2,4-6]

The example of a cancellation of a multi-frequency interference given in Fig. V.4 shows that a narrowband array processor suppresses a broadband jammer by placing the null over a wide region near the interference direction. This is true in general for any narrowband array processor with a number of elements sufficiently large to null a broadband interference. A large number is needed because the array pattern shifts with frequency. By solving Eq. V.9 explicitly for the case of a single broadband interference incident at an angle  $\theta_i$  with respect to boresight, we will show analytically that the broadband system suppresses the interference with a null that does not shift with frequency, placed precisely at  $\theta_i$ .

Let  $\alpha(t)$  be the broadband interference waveform incident at an angle  $\theta_i$  with respect to boresight, so that the  $n_{th}$  element receives the relatively delayed version  $\alpha(t - n\Delta)$ , where  $\Delta = d \sin \theta_i / c$ . Assume that the interference waveform is derived from a zero mean stationary random process with the autocorrelation function given by  $\gamma(\tau) = E[\alpha(t + \tau) \alpha^*(t)]$ , the covariance between the interference received by the  $n_{th}$  and  $m_{th}$  elements is given by

$$\begin{aligned} \gamma_{mn}(\tau) &= E[\alpha(t + \tau - m\Delta) \alpha^*(t - n\Delta)] \\ &= \gamma(\tau + (n - m)\Delta). \end{aligned} \quad (V.10)$$

The inclusion of sensor or receiver noise that is uncorrelated for each element and assumed to be white with spectral density  $\sigma_0^2$  yields

$$\gamma_{mn}(\tau) = \gamma(\tau + (n - m)\Delta) + \delta_{mn}\delta(\tau)\sigma_0^2 \quad (V.11)$$

as the covariance of the total noise present in the  $m_{th}$  and  $n_{th}$  elements. The noise cross spectral density matrix, required for the optimal solution, is the Fourier transform of the above expression. It is given by

$$\Gamma_{mn}(f) = \exp\{j2\pi f(n - m)\Delta\}S_\alpha(f) + \delta_{mn}\sigma_0^2. \quad (V.12)$$

The particularly simple form assumed by the noise cross spectral density matrix enables the inversion of Eq. V.9 to be carried out explicitly. It can be shown that the solution of Eq. V.9, which gives the optimum form for each filter, is given by

$$H_n(f) = (S_0/\sigma_0^2)\{1 - \exp\{-j\pi f\Delta(N + 1 - 2n)\} \frac{\sin(\pi f N \Delta)}{\sin(\pi f \Delta)} S_v(f)/(\sigma_0^2 + N S_v(f))\}. \quad (V.13)$$

The gain pattern that results from this choice of filters can be determined by computing the array response to a monochromatic plane wave signal at various frequencies and incidence angles. Specifically, if we let  $\theta$  represent the incidence angle of this probe beam, the gain pattern as a function of the probe frequency and angle is given by

$$g(f, \theta) = (\exp\{-j\pi f(N + 1)\Delta'\} S_0/\sigma_0^2) \left\{ \frac{\sin(\pi f N \Delta')}{\sin(\pi f \Delta')} - \exp\{-j\pi f(\Delta' - \Delta)(N + 1)\} \frac{\sin(\pi f N \Delta)}{\sin(\pi f \Delta)} \frac{S_v(f)}{(\sigma_0^2 + N S_v(f))} \right\}, \quad (V.14)$$

where  $\Delta' = d \sin \theta / c$ . At incidence angles other than that of the interference,  $\theta_i$ , the second term is small since  $\Delta \neq \Delta'$  so that

$$g(f, \theta \neq \theta_i) \approx (S_0/\sigma_0^2) \exp\{-j\pi f(N + 1)\Delta'\} \frac{\sin(\pi f N \Delta')}{\sin(\pi f \Delta')}, \quad (V.15)$$

which is simply the array pattern with uniform weighting.

When we probe near the interference, however, so that  $\theta \approx \theta_i$ , then the second term becomes appreciably large and the gain becomes

$$g(f, \theta \approx \theta_i) \approx (S_0/\sigma_0^2) \exp\{-j\pi f(N + 1)\Delta\} \frac{\sin(\pi f N \Delta)}{\sin(\pi f \Delta)} \{1 - N S_v(f)/(\sigma_0^2 + N S_v(f))\}. \quad (V.16)$$

With the assumption that the interference power is large compared to that of the detector noise so that  $N S_v(f) \gg \sigma_0^2$ , the gain becomes zero near the interference direction. Note also that this null in the array pattern remains fixed for all frequencies where there is sufficient interference power to overcome the detector noise.



## V.4 Adaptive Array Processor

As in the strictly temporal case, the adaptive broadband sidelobe canceller also utilizes convolvers and correlators to accomplish the desired task. However, because of the multi-dimensional nature of the signals (spatial and temporal), arrays of correlators and convolvers must be employed. The basic system is shown in Fig. V.6.

The output of the processor is simply the sum of all of the signals from the array elements and a feedback signal, which is derived from a cascade of multi-channel correlation and convolution operations performed on the output and input signals. The output is fed back to the first block, which calculates the correlation between the output signal and the  $N$  input signals from the array elements. Each of the resulting correlation functions, given by  $(u_n(t) \star z(t))$ ,  $n = 1, 2, \dots, N$ , is then convolved with its corresponding input. The  $N$  convolved results are summed to give

$$\hat{u} = G \sum_{n=1}^N u_n(t) \star (u_n(t) \star z(t)) \quad (V.17)$$

as the feedback signal, where  $G$  is the feedback gain.

To show that the adaptive processor approximates the optimum response, however, the output must first be expressed in the form of Eq. V.5, where the impulse response for each array filter is explicitly shown. We will show that the equation describing the filter impulse response functions,  $h_n(t)$ ,  $n = 1, 2, \dots, N$ , of the adaptive processor is approximately equivalent to that of the minimum mean-squared error processor given by Eq. V.9.

In order to clarify the analysis to follow, we redraw the schematic of Fig. V.6a as shown in Fig. V.6b so that as in the Frost architecture (Fig. V.5), the output from individual filters can be identified and described. Here, the output of the  $n_{th}$  filter is given by

$$y_n(t) = \int_{-\infty}^{\infty} h_n(t - \tau) u_n(\tau) d\tau,$$

or equivalently,  $Y_n(f) = H_n(f)U_n(f)$  where  $Y_n(f)$  is the Fourier transform of  $y_n(t)$ . The overall output is then given by  $z(t) = \sum_n y_n(t)$ . Inspection of Fig. V.6b yields

$$\begin{aligned} x_n(t) &= u_n(t) - G[u_n(t) \star z(t)] \star u_n(t) \\ &= \left[ \delta(t) - G[u_n(t) \star z(t)] \right] \star u_n(t), \end{aligned} \quad (V.18)$$

where  $\delta(t)$  is the Dirac delta function. Since  $x_n(t) = h_n(t) \star u_n(t)$ , the impulse response of the  $n_{th}$  filter is described by

$$\begin{aligned} h_n(t) &= \delta(t) - Gu_n(t) \star z(t) \\ &= \delta(t) - Gu_n(t) \star \sum_{m=1}^N u_m(t) \star h_m(t). \end{aligned} \quad (V.19)$$

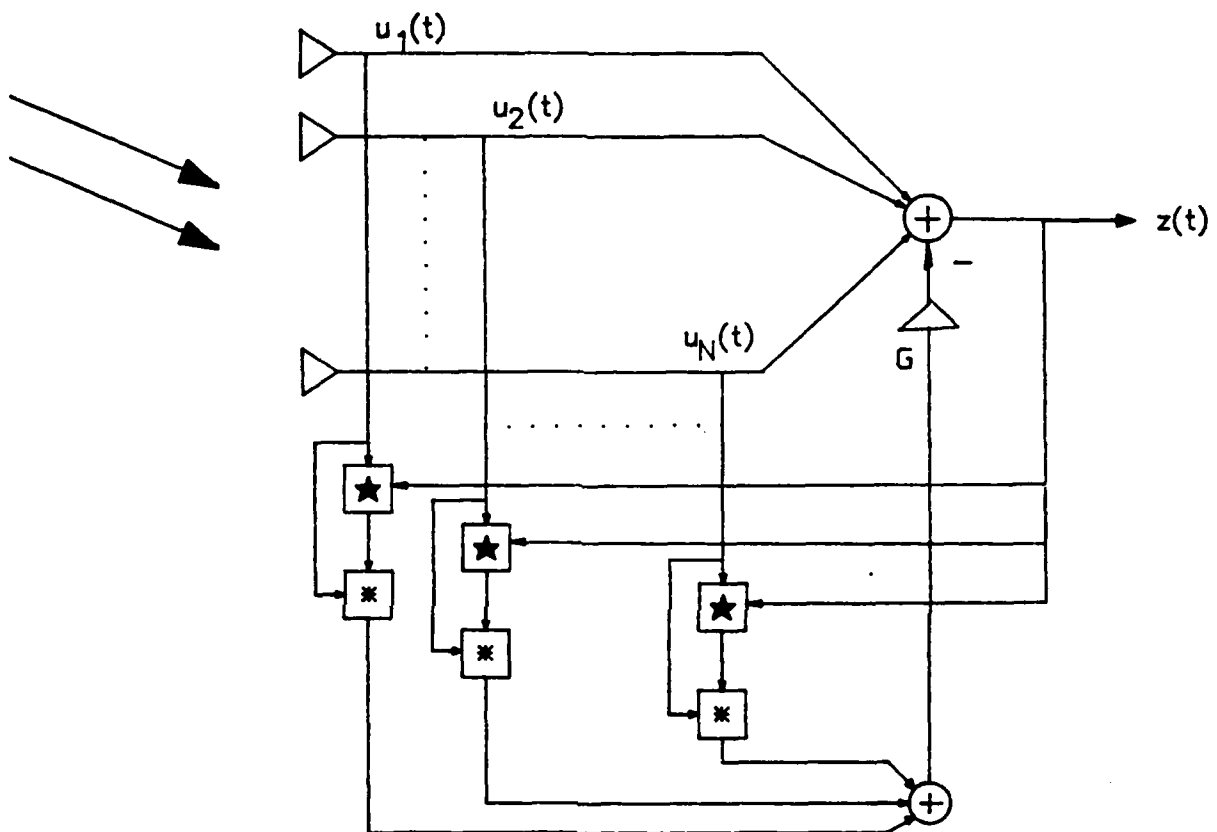


**Fig. V.6** Broadband Adaptive Sidelobe Canceller

Taking the Fourier transform of the above equation and rearranging yields

$$\sum_m [\delta_{nm} + GU_n^*(f)U_m(f)] H_m(f) = 1, \quad (V.20)$$

where  $U_n(f)$  is the Fourier Transform of  $u_n(t)$ . If the feedback gain  $G$  is sufficiently large so as to leave the first term of Eq. V.19 negligible compared to the second, then Eq. V.20 becomes

$$G \sum_m U_n^*(f)U_m(f)H_m(f) \approx 1. \quad (V.21)$$

This is of the same form as the optimum equation, Eq. V.9, provided that the input SNR is sufficiently low so that we can identify  $u_n^*(f)u_m(f)$  as the estimate of the noise cross spectral density matrix  $\Gamma_{mn}(f)$ . The particularly simple form of Eq. V.20 can be inverted, however, to give a closed form solution for the adapted filtering functions. The derivation is analogous to that leading up to Eq. V.13 and yields

$$H_n(f) = 1 - \frac{U_n^*(f) \sum_{m=1}^N U_m(f)}{1 + G \sum_{m=1}^N |U_m(f)|^2}, \quad n = 1, 2, \dots, N. \quad (V.22)$$

Suppose that the total signal received by the array consists of a weak probe signal on boresight represented by  $p(t)$  whose Fourier transform is  $P(f)$  and strong interference signals incident in other directions, the noise received by the  $n_{th}$  element represented by  $v_n(t)$  whose Fourier transform is  $V_n(f)$ . Thus, the total input is given by  $u_n(t) = p(t) + v_n(t)$ . The probe is sufficiently weak as to only negligibly affect the determination of the filtering functions  $H_n(f)$  so that approximately,

$$H_n(f) \approx 1 - \frac{V_n^*(f) \sum_{m=1}^N V_m(f)}{1 + G \sum_{m=1}^N |V_m(f)|^2}, \quad n = 1, 2, \dots, N. \quad (V.23)$$

The output is described by

$$\begin{aligned} Z(f) &= \sum_{n=1}^N H_n(f)U_n(f) \\ &= \sum_{n=1}^N \left[ 1 - \frac{V_n^*(f) \sum_{m=1}^N V_m(f)}{1 + G \sum_{m=1}^N |V_m(f)|^2} \right] [P(f) + V_n(f)]. \end{aligned} \quad (V.24)$$

Further expansion yields

$$\begin{aligned} Z(f) &\approx \left[ N - \frac{|\sum_{m=1}^N V_m(f)|^2}{1 + G \sum_{m=1}^N |V_m(f)|^2} \right] P(f) \\ &\quad + \sum_{n=1}^N V_n(f) \left[ 1 - \frac{\sum_{m=1}^N |V_m(f)|^2}{1 + G \sum_{m=1}^N |V_m(f)|^2} \right]. \end{aligned} \quad (V.25)$$

As expected, the second term is effectively suppressed if the feedback gain can be made large.

## V.5 Optical Implementation

The optical implementation of the adaptive sidelobe canceller is a fairly straightforward extension of the optical techniques used for the temporal systems described in Chapter 3. The extension is made simply by using arrays of convolvers and correlators to handle the  $N$  input signals from the antenna array sensors. The input spatial light modulators to be used are multi-channel and single channel acousto-optic devices that offer large dynamic range and can operate on broadband signals. We concentrate first on a space-time integrating system that involves the use of a photorefractive crystal to perform the time integration. A strictly space integrating array processor is described in Section V.6.

The basic task of the processor is to form the feedback signal given by Eq. V.17. Note, however, that since correlation can be expressed as  $u_n(t) \star z(t) = u_n^*(-t) \star z(t)$ , and convolution is both an associative and commutative operation, the feedback signal can be expressed equivalently as

$$\hat{u}(t) = Gz(t) \star \sum_{n=1}^N u_n(t) \star u_n^*(-t). \quad (V.26)$$

This rearrangement suggests that we can modify the system architecture somewhat by first computing an autocorrelation function of each input signal, adding the autocorrelations

and convolving the summed result with the output,  $z(t)$ , to form the feedback signal as illustrated in Fig. V.7.

For the purpose of discussion, however, we adhere to the strict interpretation of Eq. V.17 as discussed in V.4. As shown in Fig. V.6a, the output is first correlated against each of the  $N$  input waveforms, and each resulting correlation is then convolved with its corresponding input. The  $N$  convolution-correlation signals thus produced are summed to form the feedback signal. The multi-channel correlations are performed using time integration and the convolution with the output signal is achieved with space integration.

Shown in Fig. V.8 is the multi-channel correlator, where the output autocorrelations are written as modulations of an index grating formed on the crystal by the photorefractive effect. More specifically, AOD1 and AOD2 are arranged to operate in a coherent, additive architecture. The single channel AOD1 diffracts a portion of its input light. This passes through AOD2 without being affected because of Bragg mismatch and is imaged onto the crystal to yield the amplitude  $z(t + x/v - T/2)\exp\{j2\pi f_0(t + x/v)\}$  in the crystal plane. The multi-channel AOD2 diffracts the undiffracted beam from AOD1, which is aligned to be well matched to its acoustic gratings to yield the optical amplitude

$$\sum_n u_n(t - x/v - T/2)r_n(y)\exp\{j2\pi f_0(t - x/v)\},$$

also imaged onto the crystal. Here  $r_n(y)$  characterizes the vertical confinement of the acoustic beam in each channel of the multi-channel AOD and can be approximated by

$$r_n(y) = \left(\frac{1}{N\delta y}\right)\text{rect}\left[\frac{y - (n - \frac{N+1}{2})y_0}{\delta y}\right], \quad n = 1, 2, \dots, N, \quad (\text{V.27})$$

$\delta y$  being the acoustic beam width and  $y_0$  the separation between neighboring channels, where  $N$  is assumed to be odd.

These two amplitudes are incident at an angle with respect to each other. Since both have the same Doppler-shift in frequency, an intensity grating is seen by the crystal. In fact, an array of one-dimensional modulated index gratings, each confined vertically by  $r_n(y)$ , is formed within the crystal. It can be shown that the modulation functions are proportional to the desired correlation functions, and specifically, the diffracted light due to the  $n_{th}$  grating when the crystal is illuminated by a plane wave is given by [8]  $E_n(x, y)\exp\{-j2\pi f_0(2x/v)\}$ . Here

$$\begin{aligned} E_n(x, y) &\propto r_n(y) \int_0^t \exp[(t' - t)/\tau] u_n(t' - x/v - T/2) z^*(t' + x/v - T/2) dt' \\ &\propto r_n(y) \int_{t-x/v-T/2-\tau}^{t-x/v-T/2} u_n(t') z^*(t' + 2x/v) dt'. \end{aligned} \quad (\text{V.28})$$

In this equation, the exponentially decaying window function has been approximated by a rectangular window of temporal duration  $\tau$ . The resulting integral is proportional to the correlation function of  $u_n(t)$  and  $z(t)$  with  $2x/v$  as the shift variable.

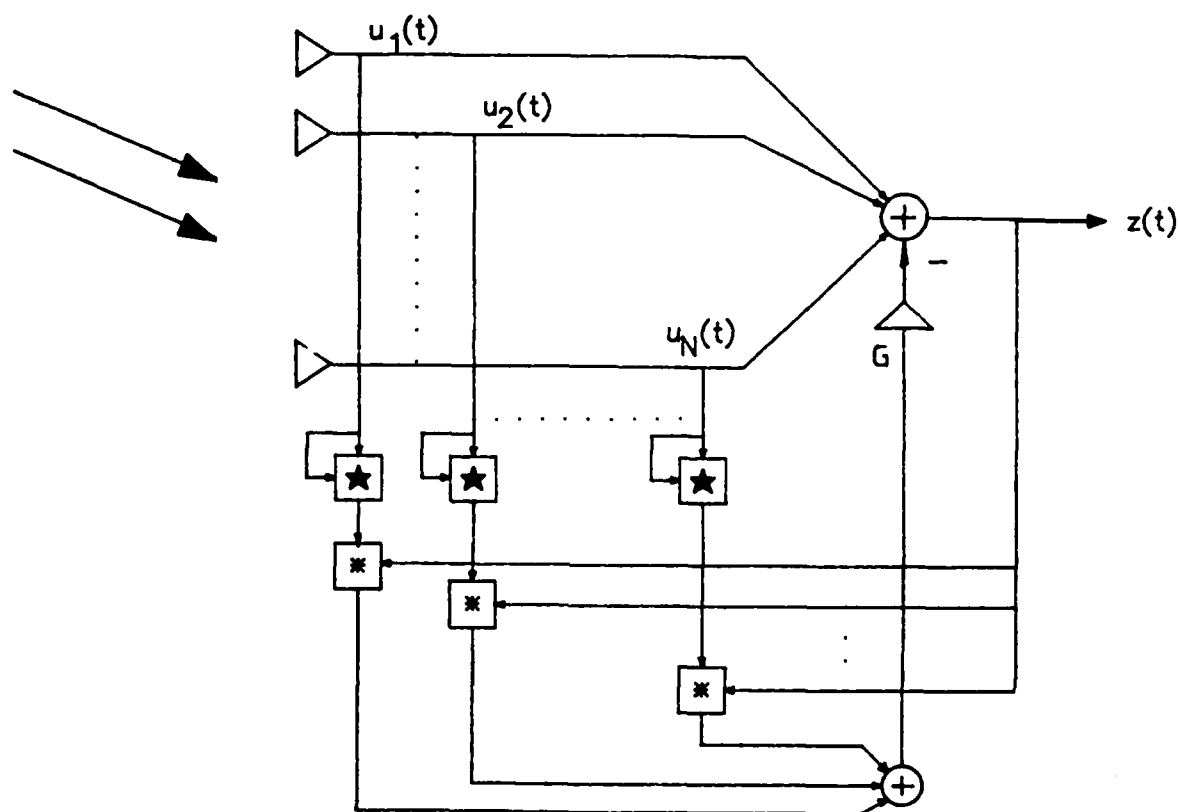


Fig. V.7 Variant of the Broadband Adaptive Array Processor

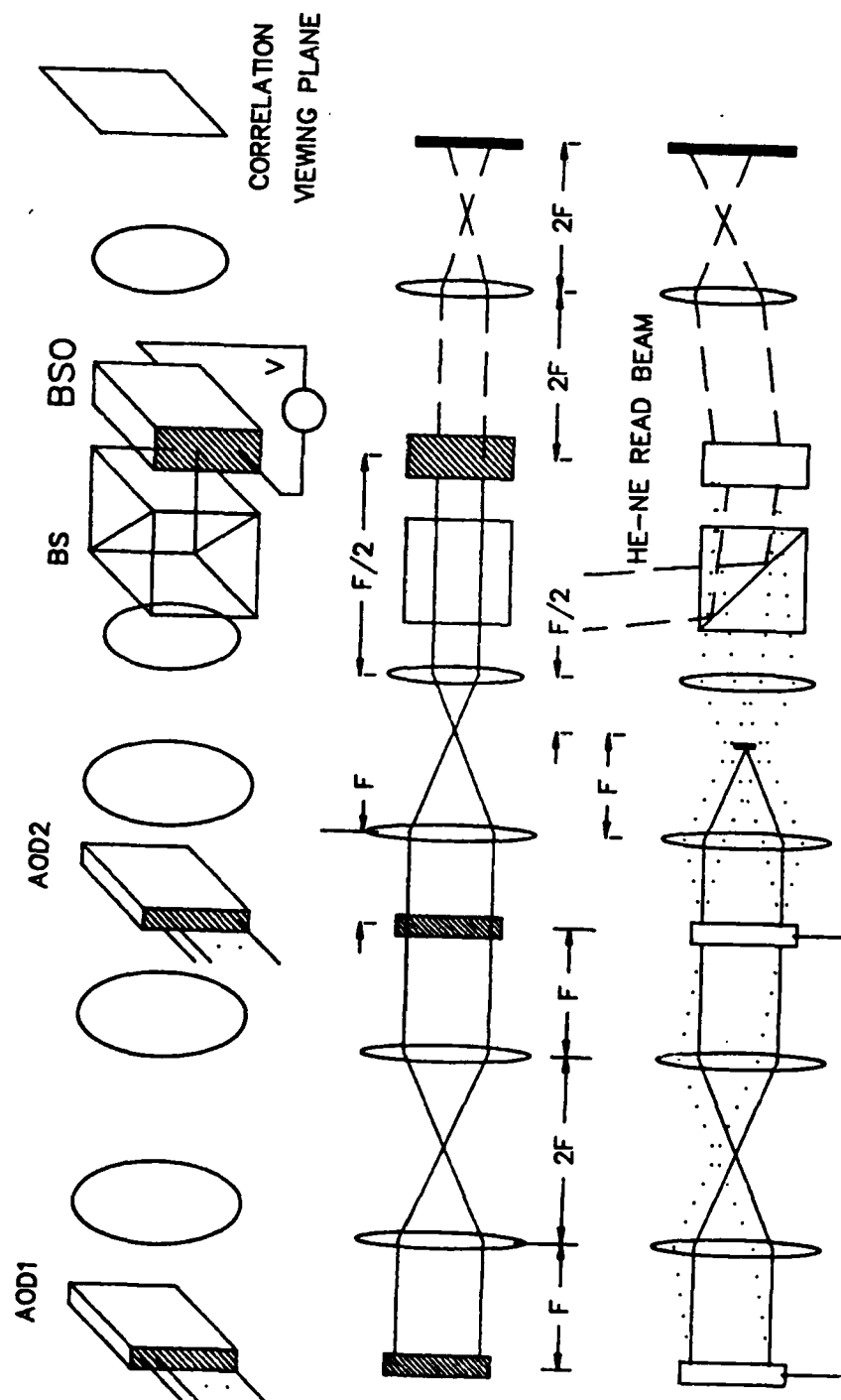


Fig. V.8 Multi-Channel Photorefractive Correlator

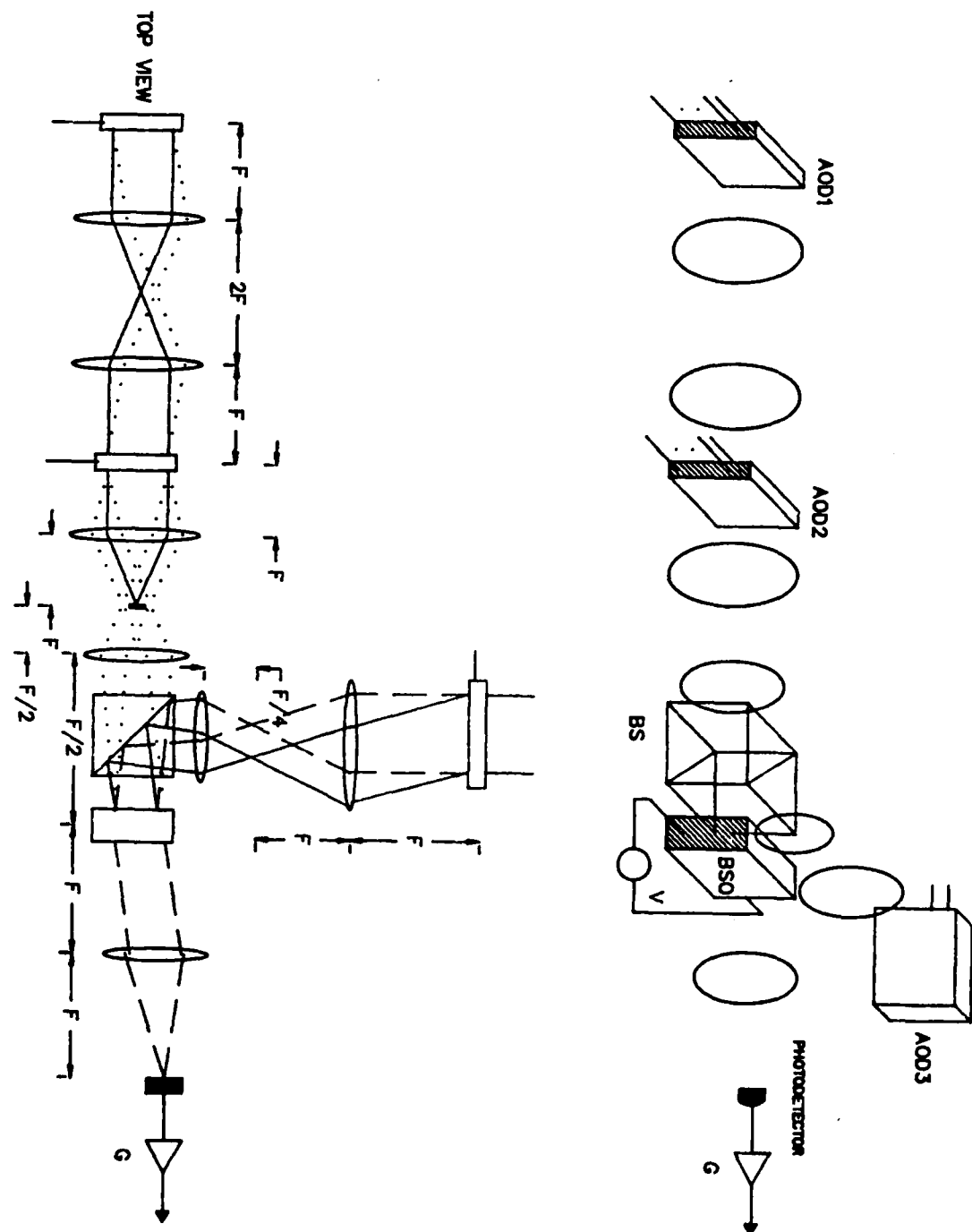


Fig. V.9 Photorefractive Adaptive Array Sidelobe Canceller



To complete the task of forming the feedback signal, we combine the previously described correlators with a space integrating convolver, resulting in the system shown in Fig. V.9. The added portions are the multi-channel AOD (AOD3) which is driven by the system output  $z(t)$ , some imaging optics, and a single photodetector. Since the auto-correlations are available at a compressed horizontal spatial scale,  $2x/v$ , a combination of cylindrical and spherical lenses C1, L5, L6 is used to anamorphically image AOD3 onto the crystal. This anamorphic imaging provides a 2:1 demagnification ratio in the horizontal direction and 1:1 in the vertical.

A portion of the He-Ne read beam is diffracted by AOD3 and passes through the crystal unaffected since its propagation direction is not properly Bragg-matched to the correlation gratings in the crystal. The DC beam from AOD3, however, is arranged to be Bragg matched to the gratings and reads out the correlation functions. If the acoustic velocity in AOD3 is  $v$ , the same as that of AOD1 and AOD2, and all of the AODs are driven at the same frequency,  $f_0$ , then the read beam diffracted by the crystal and that diffracted by AOD3 are collinear and interfere temporally at  $f_0$  because of the Doppler shift induced by AOD3. The diffracted light amplitude just behind the crystal due to the crystal gratings is proportional to  $\sum_n E_n(x, y) \exp\{j2\pi f_0(-2x/v)\}$ , and the diffracted light from AOD3 evaluated at the same plane is  $\sum_n \exp[j2\pi f_0(t - 2x/v)] u_n(t - 2x/v - T/2) r_n(y)$ .

The sum of the above two amplitudes are Fourier transformed by lens L7, and the resulting intensity distribution is integrated across the Fourier plane by a sufficiently large photodetector. If  $w$  is the width of each AOD, the result is the output photocurrent

$$\begin{aligned}
 i(t) &\propto \text{Re} \left\{ \exp\{j2\pi f_0 t\} \sum_n \int_{-w/4}^{w/4} \int_{-\infty}^{\infty} E_n^*(x, y) u_n(t - 2x/v - T/2) dy dx \right\} \\
 &\quad + \text{DC terms} \\
 &\propto \text{Re} \left\{ \exp\{j2\pi f_0 t\} \sum_n \int_{-w/4}^{w/4} \int_{-\infty}^{\infty} \int_{t-x/v-T/2-\tau}^{t-x/v-T/2} r_n(y) u_n^*(t') z(t' + 2x/v) \right. \\
 &\quad \left. u_n(t - 2x/v - T/2) dt' dy dx \right\} + \text{DC terms} \\
 &\propto \text{Re} \left\{ \exp\{j2\pi f_0 t\} \sum_n \int_{-T/4}^{T/4} \int_{t-x/v-T/2-\tau}^{t-x/v-T/2} u_n^*(t') z(t' + 2x/v) \right. \\
 &\quad \left. u_n(t - 2x/v - T/2) dt' dx \right\} + \text{DC terms}.
 \end{aligned} \tag{V.29}$$

The high frequency term centered at  $f_0$  is approximately equal to the desired feedback signal given by Eq. V.17. The output of the system  $z(t)$  is then formed by subtracting the feedback signal from the sum of the input signals  $\sum_n u_n(t)$  to yield

$$\begin{aligned}
 z(t) = \sum_n \left\{ u_n(t) - \left( \frac{G}{T\tau} \right) \int_{-T/4}^{T/4} \int_{\tau}^0 u_n^*(t' + t - \beta - T/2) z(t' + t + \beta - T/2) \right. \\
 \left. u_n(t - 2\beta - T/2) dt' d\beta \right\},
 \end{aligned} \tag{V.30}$$

where  $\beta = x/v$ ,  $T = w/v$ , and  $G$  is the feedback gain. Here we have assumed that the signals received by the array are all centered at  $f_0$  and that they drive the AODs directly after being amplified.

By defining an equivalent impulse response,  $h_n(\alpha)$ , for the system such that  $z(t) = \sum_n \int_{-\infty}^{\infty} h_n(\alpha) u_n(t - \alpha) d\alpha$ , Eq. V.30 can be expanded further to give

$$z(t) = \sum_n \left\{ u_n(t) - \left( \frac{G}{T\tau} \right) \sum_n \int_{-T/4}^{T/4} \int_{-\tau}^0 \int_{-\infty}^{\infty} u_n^*(t' + t - \beta - T/2) h_m(\alpha) u_m(t' + t + \beta - T/2 - \alpha) u_n(t - 2\beta - T/2) d\alpha dt' d\beta \right\}. \quad (V.31)$$

An equation that describes the impulse response can then be derived by noting that the output appearing on the left side of the above equation can be expressed, using the impulse response. With the assumption that the integration time,  $\tau$ , is long enough to warrant the approximation  $\text{sinc}[f\tau] \approx \delta(f)$ , the resulting impulse response equation is given by

$$h_n(\beta) \approx \delta(\beta) - \left( \frac{G}{T} \right) \text{rect} \left[ \frac{\beta - T/2}{T} \right] \sum_m \int \int_{-\infty}^{\infty} \exp\{j2\pi f'(\beta - \alpha - T/2)\} h_n(\alpha) U_n^*(f') U_m(f') df' d\alpha, \quad (V.32)$$

where  $U_n(f)$  is the Fourier transform of the  $n_{th}$  input signal  $u_n(t)$ . Taking the Fourier transform of the above equation gives

$$H_n(f) = 1 - G \sum_m \int_{-\infty}^{\infty} \exp\{j\pi(f' - f)T\} \text{sinc}[(f' - f)T] H_m(f') U_n^*(f') U_m(f') df'. \quad (V.33)$$

This is very similar to the optimal equation discussed in V.2 if we identify the product  $U_n^*(f) U_m(f)$  as an approximation of the required cross spectral density matrix. In particular, the effect of the finite convolution time is to distort the spectral properties of the input noise field. Thus, the optical implementation is expected to place a spectrally broader null in comparison with the interference bandwidth, but the spatial characteristics remain similar to the optimal case.

## V.6 Adaptive Array Processor with Variable Look Direction

The array processor described thus far is a sidelobe-cancelling system where the maximum sensitivity (the "look direction") is always constrained to be in the direction of boresight.\* In this section, an acousto-optic processor is presented which is an extension of the temporal active processor described in [1] to the space-time domain. The optical architecture considered uses space integration as opposed to the photorefractive implementation considered in the previous section. The optimizing criterion used is that of maximizing the output SNR (signal detection) and the signal need not arrive on boresight.

The scenario considered is that where a signal waveform  $s(t)$  is incident on the array at a known angle  $\theta$  with respect to boresight, and noise (possibly broadband) from directional

---

\* The look direction can be changed by introducing appropriate delays in the signals received by each element before they are processed.

sources corrupt the received signal waveform. Let  $s_n(t) = s(t - n(d/c)\cos\theta)$  be the signal waveform received by the  $n_{th}$  element. The total signal received by the  $n_{th}$  element is then given by  $u_n(t) = s_n(t) + v_n(t)$ , where  $v_n(t)$  is the sum of all noise terms. Here  $d$  is the array element spacing, and  $c$  is the speed of light.

The output of a general space-time filter can be expressed as

$$y(t) = \sum_{n=1}^N \int_{-\infty}^{\infty} u_n(\tau) h_n(t - \tau) d\tau, \quad (V.34)$$

where  $u_n(t)$  is the complex envelope of the total rf signal (centered at  $f_0$ ) received by the  $n_{th}$  array element, and  $h_n(t)$  is the filtering function for each channel. A similar expression is obtained for the optically implemented space-time filter using two multi-channel AODs shown in Fig. V.10. This system is coherent, and the output can be shown to be given by

$$y(t) = \frac{2c_1}{T} \sum_{n=1}^N \int_0^{T/2} u_n(t - \tau - T/2) h_n(t + \tau) d\tau, \quad (V.35)$$

where the filtering function  $h_n(t)$  is used to drive the second AOD, and  $c_1$  is a constant that depends on laser power, AOD diffraction efficiencies, and the quantum efficiencies of the detectors. The only differences from the general filter (Eq. V.34) are limited accumulation time and the time compression of the output. This is of little consequence since signal detection rather than estimation is considered here. The noise  $v_n(t)$  present in the received signal is modeled by a zero-mean random process with a covariance matrix given by

$$\gamma_{mn}(t) \equiv E[v_m(t)v_n^*(t - \tau)]. \quad (V.36)$$

It can be shown through variational arguments that the choice of  $h_n(t)$ , for which the SNR of the AO space-time filter is maximum at a specified time  $t_0$ , must satisfy the following system of integral equations:

$$\sum_{m=1}^N \int_{-\infty}^{\infty} \gamma_{mn}(\tau - \beta) h_m(\beta) d\beta = \lambda s_n^*(t_0 - \tau), \quad n = 1, 2, \dots, N. \quad (V.37)$$

The details of this derivation are given in Appendix B.

For adaptivity, we need to calculate and continuously update the filter function to drive the output to the optimum result. As with the temporal active processor, the output must be correlated with the input to produce the appropriate filter function. Since the array processor has  $N$  inputs and one output, this requires that we correlate  $N$  signals with a common one. This can be achieved with the arrangement shown in Fig. V.11. That figure shows the use of a multi-channel AOD driven by the  $N$  antenna element outputs in conjunction with a single channel AOD driven by the processor output signal.

The complex envelope of the output of the  $n_{th}$  detector element is given by

$$r_n(t) = \frac{4c_2}{T} \int_{-T/4}^{T/4} y(t + \tau) u_n^*(t + 2\tau - T/2) d\tau. \quad (V.38)$$

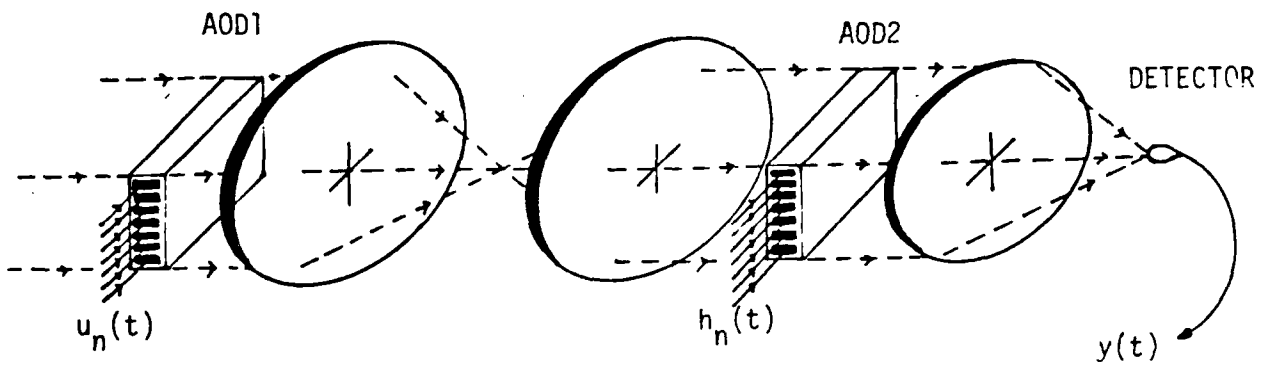


**Fig. V.10** Multi-Channel Acousto-Optic Space Integrating Convolver

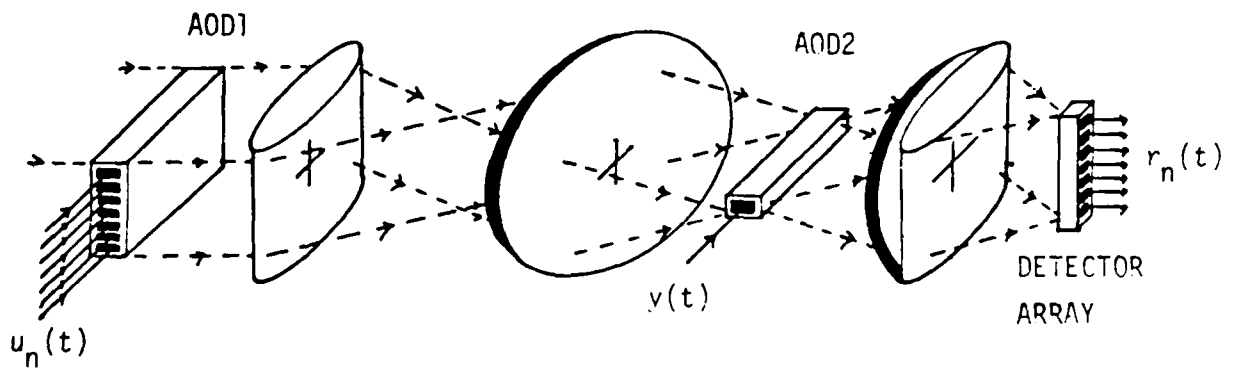


**Fig. V.11** Multi-Channel Acousto-Optic Space Integrating Correlator with a Single Reference

where  $c_2$  is a constant that depends on the laser power, AOD diffraction efficiencies, and the quantum efficiency of the detector. For proper correlation to appear at each output, the signal driving the single channel AOD must be time-compressed by a factor of two. This is indeed the case for the system described. Thus, the AOD implemented space-time filter and the  $N$  channel correlator with a single reference are compatible.

Shown in Fig. V.12 is the array processor block diagram that shows the interconnections required; it is a direct extension of the temporal active processor to two dimensions. The output from each antenna element is correlated with the processor output to produce the filter function for that element. The "steering vector"  $s_i^*(-t)$  determines the look direction of the array and also is the temporal reference signal used for the detection of the desired signal  $s(t)$ .

Fig. V.13 shows the optically implemented adaptive array processor with the AOD implemented space-time filter in the upper branch and the  $N$  channel correlator in the lower one. By combining Eqs. V.35 and V.38, the equation that determines the filter function  $h_n(t)$  is seen to be

$$h_n(t) = s_n^*(-t + t_0) - G \frac{8c_1c_2}{T^2} \sum_m \int_0^{T/2} \int_{-T/4}^0 u_n^*(t + 2/beta - T/2) u_m(t + \beta - \tau - T/2) h_m(t + \beta + \tau) d\beta d\tau, \quad (V.39)$$

where  $G$  is the feedback gain. Under conditions of low input SNR and large feedback gain, Eq. V.39 can be transformed to the frequency domain to yield

$$\exp(-j2\pi f_0 t_0) S_n^*(f) \approx G c_1 c_2 \sum_{m=1}^N H_m(f) \int_{-\infty}^{\infty} U_n^*(f') U_m(f') \exp[j\pi(f - f')T/4] \text{sinc}[(f - f')T/4] \text{sinc}[(f - f')T/2] df', \quad (V.40)$$

where  $S_n(f)$  is the Fourier transform of  $s_n(t)$ .

For comparison, consider the Fourier transform of Eq. V.36; the optimum filter equation is given by

$$\sum_m \Gamma_{mn}(f) H_m(f) = \lambda \exp(-j2\pi f t_0) S_n^*(f), \quad (V.41)$$

where  $\Gamma_{mn}(f)$  is the spectral density matrix. Identifying the integral in Eq. V.40 as the smoothed estimate of the cross spectral density matrix of the input noise vector, Eq. V.40 is approximately equivalent to Eq. V.41. However, the effect of the finite time integration window is seen in the smoothing of the noise spectrum.

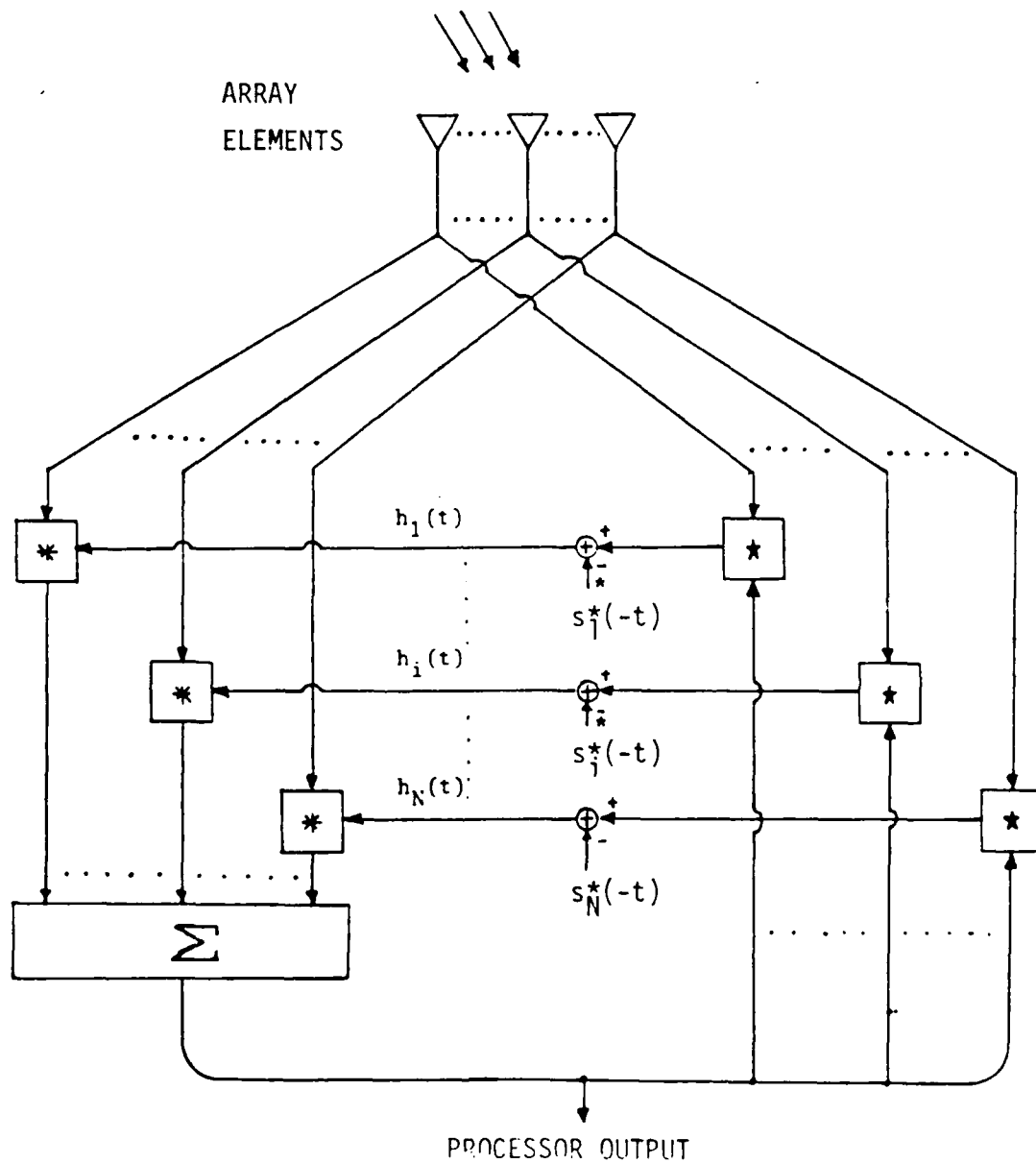


**Fig. V.12** Broadband Adaptive Array Processor to Maximize the Output SNR

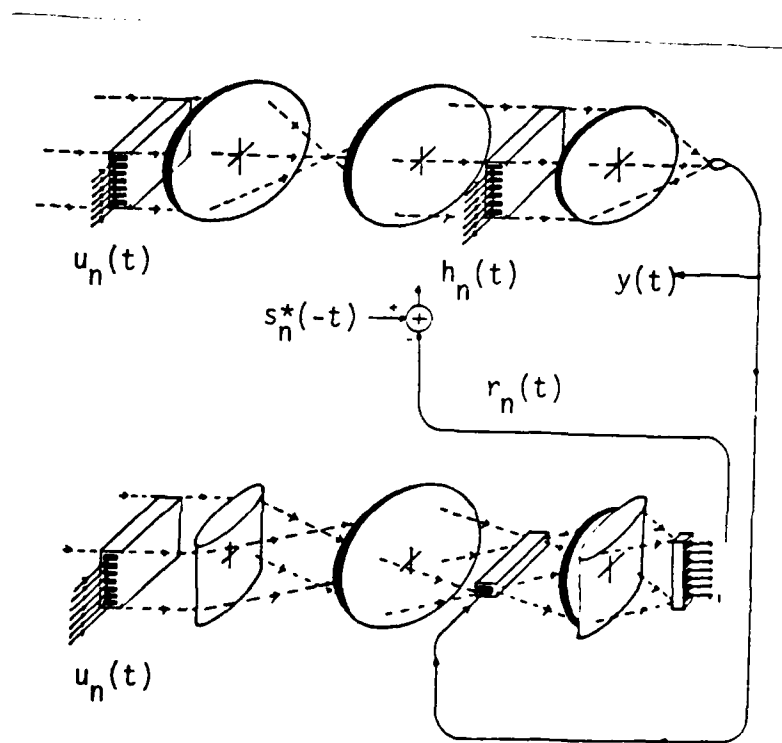


**Fig. V.13** Acousto-Optic Adaptive Array Processor to Maximize the Output SNR

## References for Chapter 4

- [1] A. P. Appelbaum, "Adaptive arrays," *IEEE Trans. Antennas. Prop.*, **AP-24**, 585,(1976).
- [2] B. Widrow, P. E. Mantey, L. J. Griffiths, and B. B. Goode, "Adaptive antenna systems," *Proc. IEEE*, **55**, 2143,(1976).
- [3] W. F. Gabriel, " Adaptive arrays - an introduction ," *Proc. IEEE*, **64**, 2 239,(Feb. 1976).
- [4] R. A. Monzingo and T. W. Miller, *Introduction to Adaptive Arrays*, John Wiley and Sons, New York, 1980.
- [5] O. L. Frost. III, "An algorithm for linearly constrained adaptive array processing," *Proc. IEEE*, **60**, no.8, 925,(Aug. 1972).
- [6] J. H. Chang and F. B. Tuteur, "A new class of adaptive array processors," *J. Acoust. Soc. Am.*, **49**, no.3, 639,(Mar. 1971).
- [7] W. E. Rodgers and R. T. Compton, Jr., "Adaptive array bandwidth with tapped delay-line processing," *IEEE Trans. Aero. Elec. Sys.*, **AES-15**, no.1, 21,(Jan. 1979).
- [8] N. V. Kukhtarev, V. B. Markov, S. G. Odulov, and M. S. Soskin, "Holographic storage in crystals I: steady state," *Ferroelectrics*, **22**, 949,(1979).
- [9] R. O. Duda and P. E. Hart, *Pattern Classification and Scene Analysis*, John Wiley and Sons, New York, 1973.
- [10] D. Psaltis and J. Hong, "Adaptive acousto-optic filter," *Applied Optics*, **23**, no. 19,(Oct. 1, 1984).
- [11] D. Psaltis, J. Yu, and J. Hong, "Bias-free time-integrating correlator using a photorefractive crystal," *Applied Optics*, **24**, 3860,(Nov. 15,1985).
- [12] J. Hong, J. Yu, S. Hudson, and D. Psaltis, "Photorefractive crystals as time-integrating elements in acousto-optic filters," *SPIE Conference: Optics, Electro-optics, and Sensors*, **789-39**, Orlando, FL,(May 20, 1987).



## Appendix

### Optimum Broadband Array Processors

The optimum broadband array-processing systems discussed in Chapter V are derived in this appendix. The two optimality criteria considered are the mean squared error and the maximum output SNR conditions. Simple variational arguments are used to derive the necessity conditions for these criteria. Since the costs to be minimized are quadratic functionals of the impulse responses that are varied, these necessity conditions are sufficient as well, and so describe the systems uniquely. Throughout this appendix, the noise received by the  $n_{th}$  array element is represented by  $v_n(t)$  which is assumed to be a zero mean, stationary, random process with covariance  $\gamma_{mn}(\tau) = E[v_m(t)v_n^*(t - \tau)]$ .

#### *Minimum Mean Squared Error Sidelobe Canceller*

We model the desired signal by a zero-mean stationary random process  $s(t)$  whose autocorrelation function is given by  $R(\tau) = E[s(t)s^*(t - \tau)]$ . Let the total signal (desired signal plus noise) received by the  $n_{th}$  element be represented by  $u_n(t) = s(t) + v_n(t)$ . Since the scenario of interest focuses on a signal arriving on boresight, each element receives the same desired signal without dispersion.

The form of the processor is shown in Fig. V.5, where the parameters that must be optimized are the  $N$  impulse response functions. The output signal is given by

$$z(t) = \sum_{n=1}^N \int_{-\infty}^{\infty} h_n(\tau) u_n(t - \tau) d\tau, \quad (A1)$$

and the cost to be minimized is given by

$$\begin{aligned} C[h_n(t)] &= E[|z(t) - s(t)|^2] \\ &= \sum_m \sum_n \int \int_{-\infty}^{\infty} h_m^*(\beta) h_n(\tau) [R(\beta - \tau) + \gamma_{nm}(\beta - \tau)] d\tau d\beta \\ &\quad + R(0) - \left\{ \sum_n \int_{-\infty}^{\infty} h_n(\tau) R(-\tau) d\tau + c.c. \right\}, \end{aligned} \quad (A2)$$

where we have assumed the noise and signal portions to be statistically independent. Let  $\hat{h}_n(t)$  represent the optimum filter for the  $n_{th}$  element, and let  $g_n(t)$  represent any other impulse response function. In order for  $\hat{h}_n(t)$  to be the cost-minimizing solution, the perturbed cost function  $C[\hat{h}_n(t) + \alpha g_n(t)]$  must have a minimum value at the point  $\alpha = \alpha_R + j\alpha_I = 0$ , where  $\alpha_R$  and  $\alpha_I$  are real. The two conditions that express this mathematically are

$$\begin{aligned} \frac{\partial}{\partial \alpha_R} C[\hat{h}_n(t) + \alpha g_n(t)]|_{\alpha=0} &= 0, \\ \frac{\partial}{\partial \alpha_I} C[\hat{h}_n(t) + \alpha g_n(t)]|_{\alpha=0} &= 0. \end{aligned} \quad (A3)$$

Carrying out the above calculations leads to two equations which combine to yield

$$\sum_n \int_{-\infty}^{\infty} g_n(\tau) \left\{ \sum_m \int_{-\infty}^{\infty} h_m^*(\beta) [R(\beta - \tau) + \gamma_{nm}(\beta - \tau)] d\beta - R^*(\tau) \right\} d\tau = 0. \quad (A4)$$

Since  $g_n(t)$  is an arbitrary function in Eq. A4, the terms within the braces must sum identically to zero. This gives the following condition that the optimum filter must satisfy:

$$\sum_m \int_{-\infty}^{\infty} h_m^*(\beta) [R(\beta - \tau) + \gamma_{nm}(\beta - \tau)] d\beta - R^*(\tau) = 0, \quad (A5)$$

which is both necessary and sufficient because the cost functional is quadratic. This is the generalization of Wiener's result to the space-time domain of broadband phased arrays.

#### *Maximum Output SNR Array Processor*

We now consider the task of signal detection, using the array processor of Fig. V.5. The signal is a known waveform  $s(t)$ , which arrives at an angle  $\theta$  with respect to boresight, and the noise field is the same as that discussed for the MMSE (Minimum Mean-Squared-Error) processor. The total signal received by the  $n_{th}$  element is therefore given by

$$u_n(t) = s_n(t) + v_n(t), \quad (A6)$$

where  $s_n(t) = s(t - nd \cos \theta / c)$  is the signal waveform as seen by the  $n_{th}$  element.

The output is given by

$$e(t) = \sum_n \int_{-\infty}^{\infty} u_n(t - \tau) h_n(\tau) d\tau. \quad (A7)$$

Since the processor is linear, the signal component can be readily identified from the noise at the output. The output signal and noise are described, respectively by

$$\begin{aligned} e_{\text{signal}}(t) &= \sum_n \int_{-\infty}^{\infty} s_n(t - \tau) h_n(\tau) d\tau, \\ e_{\text{noise}}(t) &= \sum_n \int_{-\infty}^{\infty} v_n(t - \tau) h_n(\tau) d\tau. \end{aligned} \quad (A8)$$

The goal is to maximize the output SNR given by

$$SNR = \frac{|e_{\text{signal}}(t_0)|^2}{E[|e_{\text{noise}}(t_0)|^2]} \quad (A9)$$

at a prescribed time  $t_0$ .

An equivalent problem is to minimize the output noise power while constraining all admissible impulse responses to give the same output signal amplitude at  $t_0$ . In particular, the functional expressed by Eq. A9 can be maximized by minimizing the cost given by

$$\begin{aligned} Q[h_n(t)] &= E[|e_{noise}(t_0)|^2] - \lambda \left\{ \sum_n \int_{-\infty}^{\infty} s_n(t_0 - \tau) h_n(\tau) d\tau - c \right\} \\ &= \sum_n \sum_m \int \int_{-\infty}^{\infty} h_n(\tau) h_m^*(\beta) \gamma_{nm}(\beta - \tau) d\tau d\beta \\ &\quad - \lambda \left\{ \sum_n \int_{-\infty}^{\infty} s_n(t_0 - \tau) h_n(\tau) d\tau - c \right\}, \end{aligned} \quad (A10)$$

where the constraint  $e_{signal}(t_0) = c$  has been included through the use of the Lagrangian multiplier  $\lambda$ .

Again, representing the optimum filter by  $\hat{h}_n(t)$  and an arbitrary function by  $g_n(t)$ , we apply the conditions given by Eq. A3 to obtain

$$\sum_n \int_{-\infty}^{\infty} g_n(\tau) \left\{ \sum_m \int_{-\infty}^{\infty} \gamma_{nm}(\beta - \tau) h_m^*(\beta) d\beta - \lambda s_n(t_0 - \tau) \right\} d\tau = 0. \quad (A11)$$

Since  $g_n(t)$  is an arbitrary function, the terms within the braces must sum identically to zero, yielding the condition

$$\sum_m \int_{-\infty}^{\infty} \gamma_{mn}(\tau - \beta) h_m(\beta) d\beta = \lambda^* s_n^*(t_0 - \tau), \quad (A12)$$

which is the matched filter result generalized for phased-array processing. The Lagrangian multiplier  $\lambda$  is immaterial since it merely multiplies all  $N$  filters by a constant factor and has no effect on the output SNR. Therefore, Eq. A12 describes the optimum result to within a constant factor.

## VI

### INVERSE SYNTHETIC APERUTURE RADAR : IMAGING METHOD AND OPTICAL IMPLEMENTATION

#### VI.1 Introduction

Radar has proven over many years as an effective means of detecting and tracking targets. A very desirable additional feature is the ability to identify the target being tracked. The most straight-forward approach to target identification is to produce an image of the target which can then be presented to a pattern recognition system. Unfortunately radars, due to practical constraints on their physical apertures, are generally not able to obtain enough information from a single radar echo to produce an image. Instead they must *synthesize an aperture* by recording over time, as either the target or the radar moves, a series of echos from the target until enough information is obtained to produce an image. The recorded echos contain information not only about the target's reflectivity, which is what we wish to compute in the imaging process, but also the about the relative motion between radar and target. The effects of the latter can interfere with the imaging process and must be compensated for if a well-focused image of the target is to be produced.

#### VI.2 Fundamentals of Radar Imaging

When viewed from a small range of angles a target can be characterized by a *reflectivity function*  $f(\vec{r})$  such that if a field  $E(t)$  is incident from a radar onto a volume  $d^3r$ , centered at a point  $\vec{r}$  on the target, then a field  $f(\vec{r})E(t)d^3r$  is reflected back towards the radar (we use a coordinate system centered and fixed on the target). Imaging a target is the process of computing  $f(\vec{r})$ .

If the radar sits at the point  $\vec{\rho}$  and transmits a field

$$e^{j2\pi\nu_0 t}$$

then the reflected field received at the radar is given by

$$e^{j2\pi\nu_0 t} E(\nu_0) = e^{j2\pi\nu_0 t} \int f(\vec{r}) e^{-j2\pi\nu_0 2|\vec{\rho}-\vec{r}|/c} d^3r \quad (VI.1)$$

which is the sum of the reflected fields from all points on the target, each of which has a phase shift due to the  $2|\vec{\rho}-\vec{r}|/c$  time it takes the signal to go from the radar to the point  $\vec{r}$  and back. If  $\rho \equiv |\vec{\rho}|$ , the *gross-range*, is large enough to put the radar in the target's far-field then the far-field approximation

$$|\vec{\rho}-\vec{r}| \approx \rho - \vec{e}_\rho \cdot \vec{r} \quad (VI.2)$$

is valid, where  $\vec{e}_\rho$  - *the aspect* - is the unit vector in the radar's direction. Using (VI.2) in (VI.1) and mixing out the temporal carrier  $\exp(j2\pi\nu_0 t)$ , we have

$$E(\nu_0) = e^{-j2\pi 2\nu_0 \rho/c} \int f(\vec{r}) e^{j2\pi [2\nu_0 \vec{e}_\rho/c] \cdot \vec{r}} d^3 r. \quad (VI.3)$$

Using the definition of the Fourier transform

$$\hat{f}(\vec{u}) = \int f(\vec{r}) e^{j2\pi \vec{u} \cdot \vec{r}} d^3 r$$

(VI.3) can be written as

$$E(\nu_0) = e^{-j2\pi 2\nu_0 \rho/c} \hat{f}(2\nu_0 \vec{e}_\rho/c).$$

Thus, apart from a gross-range-induced phase distortion, the radar has obtained a sample of the target's spatial spectrum. The location of the sample in the target's Fourier space is determined by the radar's frequency and aspect. If instead of a pure sinusoid the radar transmits a signal of bandwidth  $\beta$  around a center frequency  $\nu_0$  then the target's spectrum will be sampled along that portion of the ray  $\vec{e}_\rho$  from  $2(\nu_0 - \beta/2)/c$  to  $2(\nu_0 + \beta/2)/c$  in magnitude. If additionally some relative motion between the target and radar causes  $\rho$  and  $\vec{e}_\rho$  to become functions of time -  $\rho(t)$  the *gross-range history* and  $\vec{e}_\rho(t)$  the *aspect history* respectively - then

$$E(\nu_0 + \nu, t) = e^{-j2\pi 2(\nu_0 + \nu)\rho(t)/c} \hat{f}(2(\nu_0 + \nu)\vec{e}_\rho(t)/c) \quad (VI.4)$$

for  $-\beta/2 \leq \nu \leq \beta/2$ . Hence by exploiting wide-band signals and radar/target motion a region of the target's Fourier space can be recorded. This process is referred to as *synthesizing an aperture*. Computing  $f(\vec{r})$  is then a matter of putting this data in a suitable form and inverse Fourier transforming.

### VI.3 Motion Compensation

If we know  $\hat{f}(\vec{u})$ , the Fourier transform of  $f(\vec{r})$ , in a region of Fourier space we can inverse transform and obtain  $f(\vec{r})$  to within the resolution determined by the finite extent of the region. Unfortunately the data  $E(\nu_0 + \nu, t)$  is not recorded as a function of the target's spatial frequency,  $\vec{u}$ , but as a function of radar frequency and time,  $\nu_0 + \nu$  and  $t$  respectively. To figure out the value of  $\hat{f}(\vec{u})$  at some position  $\vec{u}_1$  in Fourier space from the recorded data we need to find  $\nu_1$  and  $t_1$  such that

$$2(\nu_0 + \nu_1)\vec{e}_\rho(t_1)/c = \vec{u}_1. \quad (VI.5)$$

so that

$$E(\nu_0 + \nu_1, t_1) = e^{-j2\pi 2(\nu_0 + \nu_1)\rho(t_1)/c} \hat{f}(\vec{u}_1).$$

In addition we need to know the value of  $\rho(t_1)$  so that we can eliminate the phase distortion and arrive at

$$\hat{f}(\vec{u}_1) = e^{j2\pi 2(\nu_0 + \nu_1)\rho(t_1)/c} E(\nu_0 + \nu_1, t_1).$$

The frequency  $\nu_1$  can be solved for easily from (VI.5)

$$\|\vec{u}_1\| = 2(\nu_0 + \nu_1)/c \Rightarrow \nu_1 = \frac{1}{2}c\|\vec{u}_1\| - \nu_0.$$

To find  $t_1$  from (VI.5) we need to solve

$$\vec{e}_\rho(t_1) = \vec{u}_1 / \|\vec{u}_1\|$$

which requires knowledge of the aspect history  $\vec{e}_\rho(t)$  just as removal of the phase distortion requires knowledge of the gross-range history  $\rho(t)$ . Removing gross-range-induced phase distortion and mapping from radar frequency and time to position in the target's Fourier space are referred to as *motion compensation*. We will refer to the former as *gross-range compensation* and to the latter as *aspect compensation*.

The term *synthetic aperture radar* (SAR) is used to describe situations in which the target is stationary and relative motion between radar and target is due to radar motion alone. Since the radar's motion is generally controllable and/or measurable both the gross-range and aspect histories are known and hence motion compensation can be performed and an image of the target produced.

*Inverse synthetic aperture radar* (ISAR) describes situations in which the target is moving so relative motion is due, at least in part, to target motion. This is the kind of imaging we will discuss in this paper. Since target motion is generally *not* controllable and *not* measurable we lack the complete knowledge of the gross-range and aspect histories needed to perform motion compensation. Thus ISAR imaging is not possible unless we can measure  $\rho(t)$  and  $\vec{e}_\rho(t)$  or figure out some way to compute them during the imaging process. Because radars are range measuring devices it is possible to measure  $\rho(t)$  and techniques have been developed to perform gross-range compensation [1,2]. Therefore in what follows we will assume this has been done and concentrate on the problem of performing aspect compensation.

#### VI.4 ISAR Imaging in Two Dimensions

We are going to examine the special case in which target motion is such that  $\vec{e}_\rho(t)$  is confined to a single plane through the origin. This accurately describes a great many cases of practical interest - e.g. targets moving in straight lines, targets rotating about some fixed axis - and is the case commonly treated in the literature [1,2,3]. By the choice of coordinate axes, we can always take this plane to be the  $x, y$  plane so that  $\vec{e}_\rho = [\cos\theta(t), \sin\theta(t), 0]$ . Then equation (VI.4) describing the reflected field becomes, after gross-range compensation,

$$\begin{aligned} E(\nu_0 + \nu, t) &= \int f(\vec{r}) e^{j2\pi 2(\nu_0 + \nu)\vec{e}_\rho(t) \cdot \vec{r}} d^3r \\ &= \int \int \int f(x, y, z) e^{j2\pi 2(\nu_0 + \nu)[x \cos\theta(t) + y \sin\theta(t)]} dx dy dz \end{aligned}$$

$$= \int \int f(x, y) e^{j2\pi 2(\nu_0 + \nu)[x \cos \theta(t) + y \sin \theta(t)]} dx dy \quad (VI.6)$$

where

$$f(x, y) \equiv \int f(x, y, z) dz.$$

Motion limited to a single plane results in a lack of information about the target in the direction perpendicular to that plane; the radar "sees" a two-dimensional target  $f(x, y)$  which is the projection of the real three-dimensional target onto the plane of motion. We will assume that during the time the radar observes the target the following small angle approximations are valid,

$$\cos \theta(t) \approx 1$$

$$\sin \theta(t) \approx \theta(t)$$

$$2\nu y \theta(t)/c \ll 1.$$

Using these in (VI.6) results in

$$E(\nu_0 + \nu, t) = \int \int f(x, y) e^{j2\pi 2[(\nu_0 + \nu)x/c + \nu_0 y \theta(t)/c]} dx dy.$$

Processing this recorded field into an image proceeds in two steps.

First we resolve in the  $x$  or *range* direction by inverse Fourier transforming over the band of transmitted frequencies. We obtain

$$\begin{aligned} & \int_{-\beta/2}^{\beta/2} E(\nu_0 + \nu, t) e^{-j2\pi 2(\nu_0 + \nu)x/c} d\nu \\ &= \int_{-\beta/2}^{\beta/2} \int \int f(\xi, y) e^{j2\pi 2[(\nu_0 + \nu)(\xi - x)/c + \nu_0 y \theta(t)/c]} d\xi dy d\nu \\ &= \int \left( \beta \int f(\xi, y) e^{-j2\pi 2\nu_0(x - \xi)/c} \text{sinc} \left( \frac{x - \xi}{c/2\beta} \right) d\xi \right) e^{j2\pi 2\nu_0 y \theta(t)/c} dy \\ &\approx \int f(x, y) e^{j2\pi 2\nu_0 y \theta(t)/c} dy = \hat{f}_y(x, 2\nu_0 \theta(t)/c) \equiv \hat{f}_y(x, \phi(t)) \end{aligned}$$

where for convenience we define  $\phi(t) = 2\nu_0 \theta(t)/c$ . The function  $\hat{f}_y(x, \phi(t))$  is the Fourier transform with respect to  $y$  of  $f(x, y)$ , evaluated at  $\phi(t)$ .

The second step is to achieve resolution in the  $y$  or *cross-range* direction. For each value of  $x$  the function we are left with,  $\hat{f}_y(x, \phi(t))$ , is the Fourier transform of the function we seek to compute,  $f(x, y)$ , but which has been distorted by a coordinate transformation,  $\phi(t)$ , due to the target's aspect history. In general, therefore, aspect compensation is required before imaging (inverse Fourier transforming in  $y$ ) is possible. If  $\phi(t)$  was known then aspect compensation could be performed by the inverse coordinate transformation

$$\int \hat{f}_y(x, \phi(t)) \delta(\phi(t) - v) \frac{d\phi(t)}{dt} dt = \int \hat{f}_y(x, \phi) \delta(\phi - v) d\phi = \hat{f}_y(x, v).$$

Following this with an inverse Fourier transform

$$\int \hat{f}_y(x, v) e^{-j2\pi yv} dv = f(x, y)$$

would resolve the target in  $y$  for this value of  $x$ . Repeating this process for each value of  $x$  would produce the full two-dimensional image. The coordinate transformation and Fourier transform can be combined into a single linear transformation

$$\begin{aligned} f(x, y) &= \int \hat{f}_y(x, v) e^{-j2\pi yv} dv = \int \left( \int \hat{f}_y(x, \phi(t)) \delta(\phi(t) - v) \frac{d\phi(t)}{dt} dt \right) e^{-j2\pi yv} dv \\ &= \int \hat{f}_y(x, \phi(t)) \frac{d\phi(t)}{dt} e^{-j2\pi y\phi(t)} dt. \end{aligned} \quad (VI.7)$$

The problem in ISAR imaging is that  $\phi(t)$  is unknown and therefore this transformation is unknown *a priori*.

### VI.5 Effects of Neglecting Aspect Compensation

The problem of aspect compensation is generally avoided in ISAR imaging by *assuming* that the target moved in such a smooth manner that  $\phi(t) = \Omega t$  for some unknown constant  $\Omega$ . In general  $\phi(t)$  will actually be of the form  $\phi(t) = \Omega t + \epsilon(t)$  where  $\Omega t$  is the linear part of  $\phi(t)$  and  $\epsilon(t)$  is the nonlinear part (due to, for instance, target acceleration). If we take  $\phi_e(t) = t$  as an estimate of the true  $\phi(t)$  and use this to process the data via equation (VI.7) the result is an estimate of  $f(x, y)$  given by

$$\begin{aligned} f_e(x, y) &= \int \hat{f}_y(x, \phi(t)) e^{-j2\pi y\phi(t)} dt = \int \left( \int f(x, \eta) e^{j2\pi \eta \phi(t)} d\eta \right) e^{-j2\pi y\phi(t)} dt \\ &= \int f(x, \eta) \left( \int e^{j2\pi \eta \epsilon(t)} e^{-j2\pi t(y - \Omega \eta)} dt \right) d\eta \\ &= \int f(x, \eta) h(y, \eta) d\eta \end{aligned}$$

where

$$h(y, \eta) = \int e^{j2\pi \eta \epsilon(t)} e^{-j2\pi t(y - \Omega \eta)} dt, \quad (VI.8)$$

represents the cross-range impulse response of the ISAR imaging system. That is  $h(y, \eta)$  is the cross-range image of a point scatterer at position  $\eta$  on the target. If the target actually moved so that  $\phi(t) = \Omega t$  then  $h(y, \eta) \propto \text{sinc} \Delta t (y - \Omega \eta)$ , where  $\Delta t$  is the length of time the radar observed the target, and so  $f_e(x, y) \approx f(x, y/\Omega)$  and this approach works. Diffraction limited resolution is achieved although there is an unknown scaling in  $y$  due to the unknown constant  $\Omega$ .



On the other hand if there is any non-linearity in the aspect history (i.e.  $\epsilon(t) \neq 0$ ) then  $h(y, \eta)$  will have a width greater than that of the diffraction limit. If  $|\eta\epsilon(t)|$  is small then (VI.8) can be approximated by

$$h(y, \eta) \approx \int (1 + j2\pi\eta\epsilon(t)) e^{-j2\pi t(y - \Omega\eta)} dt$$

$$\propto [\text{sinc } \Delta t z + 2\pi\eta\hat{\epsilon}(z) * \text{sinc } \Delta t z]|_{z=y-\Omega\eta}$$

where  $\hat{\epsilon}$  is the Fourier transform of  $\epsilon$ . The first term is the diffraction limited impulse response. The second term produces blurring beyond the diffraction limit. It grows stronger with larger  $|\eta|$  and has a width beyond the diffraction limit equal to the spectral width of  $\epsilon(t)$ . For large  $|\eta\epsilon|$  the width of  $h(y, \eta)$  is approximately  $2|\eta| \cdot |d\epsilon/dt|_{\max}$  (twice the maximum instantaneous frequency of  $\exp[j2\pi\eta\epsilon(t)]$ ) beyond the diffraction limit. In either case the impulse response is blurred beyond the diffraction limit when there is any non-linearity in the aspect history with the blurring being worst at the edges (largest  $|\eta|$ ) of the target.

## VI.6 Learning Aspect Compensation

Computing  $f(x, y)$  from  $\hat{f}_y(x, \phi(t))$  is an underdetermined problem because we lack necessary information, namely  $\phi(t)$ , needed to obtain the correct solution. For any guess we might make at  $\phi(t)$ , say  $\phi_e(t)$ , we can produce an image, call it  $f_e(x, y)$ , through the transformation described in equation (VI.7). However  $f_e(x, y)$  will faithfully represent  $f(x, y)$  only if we somehow get  $\phi_e(t) \approx \phi(t)$ . What we need is some additional constraint on the problem which when satisfied forces  $\phi_e(t) \approx \phi(t)$ .

Neglecting aspect compensation as discussed above (which is the common practice in ISAR imaging) essentially puts a constraint on  $\phi(t)$ ; in order to produce a well-focused image it is required that  $\phi(t) = \Omega t$ . The problem with this approach is that we don't have any control over  $\phi(t)$ , since we don't control the target's motion, and hence we can't enforce this constraint. A better approach, we think, is to put a constraint on something we do have control over, namely the image. We have some control over the image by our choice of an aspect history estimate,  $\phi_e(t)$ . The obvious constraint is to require that the image be as well-focused as possible. Therefore we loosen constraints on the target's motion by adopting a parametric form for  $\phi_e(t)$  with degrees of freedom, such as

$$\phi_e(t; a_1, \dots, a_n) = a_1 t + a_2 t^2 + \dots + a_n t^n,$$

while at the same time seeking to enforce the constraint that the image obtained by processing with  $\phi_e(t)$  be focused. Below we describe a simple quantitative measure which we can use to enforce this constraint.

With  $\epsilon(t; a_1, \dots, a_n) \equiv \phi_e(t; a_1, \dots, a_n) - \phi(t)$  denoting the error in the estimate of the aspect history we get an image of the target through the linear transformation in (VI.7) (we will no longer explicitly show the dependence of  $\phi_e$  and  $\epsilon$  on  $a_1, \dots, a_n$ )

$$f_e(x, y; a_1, \dots, a_n) = \int \hat{f}_y(x, \phi(t)) \frac{d\phi_e(t)}{dt} e^{-j2\pi y\phi_e(t)} dt$$

$$\begin{aligned}
&= \int \left( \int f(x, \eta) e^{j2\pi\eta[\phi_e(t) - \epsilon(t)]} d\eta \right) \frac{d\phi_e(t)}{dt} e^{-j2\pi y \phi_e(t)} dt \\
&= \int f(x, \eta) \left( \int e^{-j2\pi\eta\epsilon} e^{-j2\pi(y-\eta)\phi_e} d\phi_e \right) d\eta \\
&= \int f(x, \eta) h(y, \eta; a_1, \dots, a_n) d\eta
\end{aligned}$$

where

$$h(y, \eta; a_1, \dots, a_n) = \int e^{-j2\pi\eta\epsilon} e^{-j2\pi(y-\eta)\phi_e} d\phi_e$$

is the impulse response of our imaging system. The impulse response depends on  $a_1, \dots, a_n$  because  $\phi_e(t)$  and  $\epsilon(t)$  do. It is easy to show that

$$f_e(x, y; \alpha a_1, \dots, \alpha a_n) = \alpha f_e(x, \alpha y; a_1, \dots, a_n)$$

so scaling  $\phi_e(t)$  by a constant factor scales the image in the  $y$  dimension but has no effect on how well focused the image is. Assuming we have no *a priori* information about the target which would allow us to choose the proper scaling we will always scale the parameters  $a_1, \dots, a_n$  so that  $\Delta\phi_e = 1$ , where  $\Delta\phi_e \equiv \max[\phi_e(t)] - \min[\phi_e(t)]$ . This insures that the scale of the image remains constant.

By an analysis of the impulse response similar to that used in section VI.5 above we can show that image blurring increases as  $\epsilon$  grows larger and that for a given  $\epsilon(t)$  the blurring is most severe at the edges of the image (large  $|\eta|$ ). Since the width of a blurred image is the width of the well-focused image plus the width of the blurring at the edges we are led to construct an "energy" function  $w(x; a_1, \dots, a_n)$ , defined by

$$\int_{-w(x; a_1, \dots, a_n)/2}^{w(x; a_1, \dots, a_n)/2} |f_e(x, y; a_1, \dots, a_n)|^2 dy = c \int_{-\infty}^{\infty} |f_e(x, y; a_1, \dots, a_n)|^2 dy,$$

as a measure of the width of our image and hence the amount of blurring. For a given  $x$ ,  $w$  is the number such that a fraction  $c$ ,  $0 < c < 1$ , of the total energy of this strip of the image lies in the region  $x \in [-w/2, w/2]$ ; we take  $c < 1$  because due to noise and the sidelobes of the impulse response all of the energy cannot be confined to a finite region but only "most" of the energy. Our system can learn the necessary aspect compensation by searching its state space (the parameters  $a_1, \dots, a_n$ ) until it minimizes this energy function and hence the image blurring. At this point the output of the system is a well-focused strip of the image (provided there are enough degrees of freedom in  $\phi_e(t)$  to allow a good approximation to  $\phi(t)$ ). The constant scale constraint  $\Delta\phi_e = 1$  is essential because it insures that changes in  $w$  are due to changes in the amount of blurring in the image and not merely to changes in the scale of the image. Since blurring is largest for largest  $|\eta|$  aspect compensation can be learned most accurately by minimizing  $w(x_0; a_1, \dots, a_n)$  where  $w(x_0; a_1, \dots, a_n) \geq w(x; a_1, \dots, a_n)$  for all  $x \neq x_0$ , that is by learning on that strip of the image which is widest. The remainder of the image can then be computed strip

by strip through (VI.7), the kernel of which our system has just learned by minimizing  $w(x_0; a_1, \dots, a_n)$ .

To summarize, the algorithm is as follows. Initialize the parameters (we take  $a_1 = 1, a_{i \neq 1} = 0$ ). Find  $x_0$  such that  $w(x_0; a_1, \dots, a_n) \geq w(x; a_1, \dots, a_n)$ . Then minimize  $w(x_0; a_1, \dots, a_n)$  with respect to  $a_1, \dots, a_n$  producing the one strip of the image,  $f(x_0, y)$ . Finally use the aspect history estimate  $\phi_e(t; a_1, \dots, a_n)$  learned in the last step to compute the rest of the image,  $f(x \neq x_0, y)$ , strip by strip.

Figures VI.1a-VI.1c show the results of a simulation of this imaging technique. We considered a target consisting of a collection of point scatterers arranged in a "V" shape (figure VI.1a) and simulated the radar returns corresponding to an aspect history of  $\phi(t) = t^2, 0 \leq t \leq 1$ . Figure VI.1b shows the image produced by the standard processing approach which takes  $\phi_e(t) = t$ . We allowed our processor 2 degrees of freedom,  $\phi_e(t) = at + bt^2$ , which together with the scaling constraint,  $\Delta\phi_e = 1$  for  $0 \leq t \leq 1 \Rightarrow a + b = 1$ , defined a one-dimensional state space. By searching over this state space until  $w(x_0; a, b)$  was minimized (we took  $c = 0.95$ ) our processor produced the image shown in figure VI.1c.

We also applied this technique in a simple acoustic imaging experiment. Figure VI.2a is a picture of the target, a collection of ping-pong balls arranged in a "V" shape (each row of balls is about 500mm long). While illuminating the target with acoustic pulses and recording the reflected field we varied its position so that it had an aspect history  $\theta(t) = 2.5^\circ(t + t^2), 0 \leq t \leq 1$ . We then produced images using both the standard processing approach and our algorithm (with  $\phi_e(t) = at + bt^2$  and  $a + b = 1$  as above). The resulting images are displayed in figures VI.2b and VI.2c respectively.

## VI.7 Optical Implementation

The computation required to produce one strip of the image, given in equation (VI.7), is a shift-variant linear transformation which optics is well suited to implement. Figure VI.3 shows an optical implementation of the iterative ISAR algorithm we described above. It consists of a programmable optical matrix-vector multiplier with an electronic feedback path from the output to the matrix. Given a matrix

$$K(t, y; a_1, \dots, a_n) = \frac{d\phi_e(t; a_1, \dots, a_n)}{dt} e^{-j2\pi y \phi_e(t; a_1, \dots, a_n)}$$

the optical section computes the linear transformation

$$f_e(x_0, y; a_1, \dots, a_n) = \int f(x_0, \phi(t)) \frac{d\phi_e(t; a_1, \dots, a_n)}{dt} e^{-j2\pi y \phi_e(t; a_1, \dots, a_n)} dt.$$

The feedback circuitry varies the matrix at each iteration through the parameters  $a_1, \dots, a_n$  and computes the energy  $w(x_0; a_1, \dots, a_n)$  from the output  $f_e(x_0, y; a_1, \dots, a_n)$ . It continues to iterate until it finds the global energy minimum. At this point the output is a well

focused image of a strip of the target around  $x_0$  and the processor has learned the necessary aspect compensation. With the matrix fixed the remaining data,  $\hat{f}_y(x, \phi(t))x \neq x_0$ , is then fed through the processor allowing the full two-dimensional image to be produced strip by strip.

We set up a preliminary version of this processor using a magneto-optic device (MOD) for the programmable matrix, a 1D CCD array to detect the output  $|f_e(x, y; a_1, \dots, a_n)|^2$ , and a PC to update the matrix. We did not implement the first half of the optical matrix-vector multiplier, which spreads  $f(x, \phi(t))$  in the  $y$  direction to form the product  $f(x, \phi(t))K(t, y; a_1, \dots, a_n)$  in the plane of the matrix. Instead we formed this product digitally and fed the result into the MOD.

Figures VI.4a-VI.4c show the output of the optical processor in various stages of learning to image a strip of the "V" shaped simulated target discussed above. The input data was the same as that used in the simulation above. The initial output (with  $\phi_e(t; a_1, \dots, a_n) = t$ ) is depicted in figure VI.4a. Here the error in the aspect history estimate is large and the image is quite blurred. From this point the processor starts moving through its state space,  $(a_1, a_2)$ , minimizing the energy  $w(x_0; a_1, a_2)$ . Figure VI.4b shows the output at an intermediate stage. Finally the processor settles at the output shown in figure VI.4c which had the minimum width and in which the two point scatterers in this strip of the image are well-focused.

## References

- [1] Wehner, D.R., *High Resolution Radar*, Artech House, 1987
- [2] Chen, C.C., Andrews, H.C., "Target-Motion-Induced Radar Imaging", *IEEE Trans. Acoust. Electron. Syst.*, vol AES-16
- [3] Farhat, N., Chu, T.H., "Tomography and Inverse Scattering", ICO-13

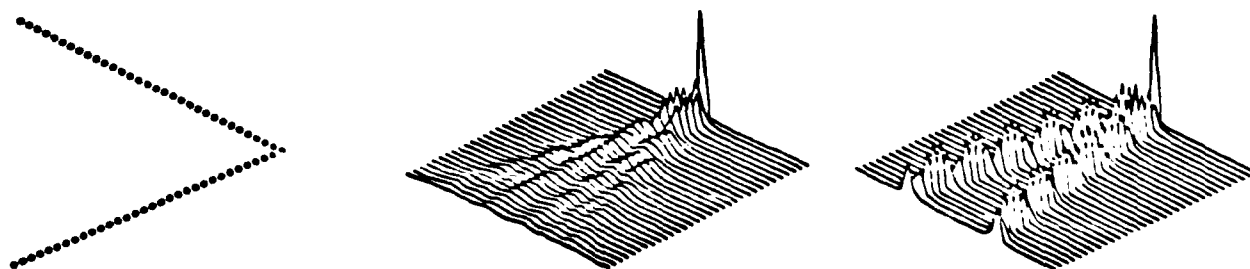


Fig VI.1a, b, c

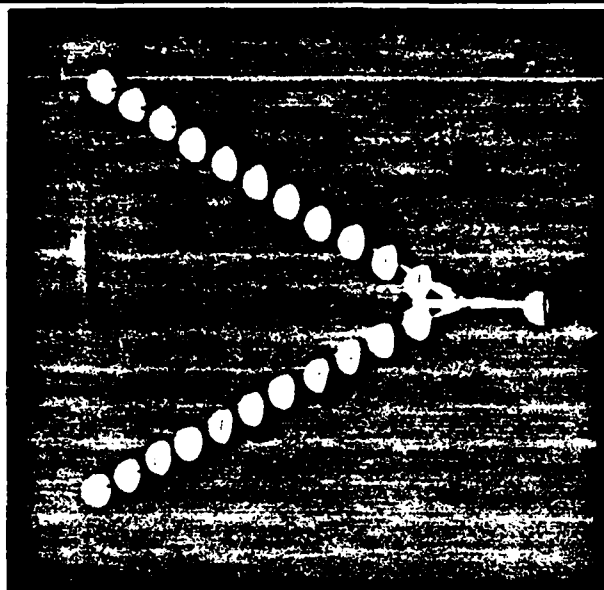


Fig VI.2a

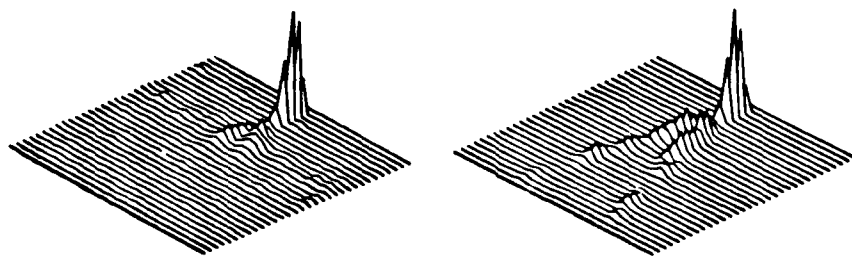


Fig VI.2b,c

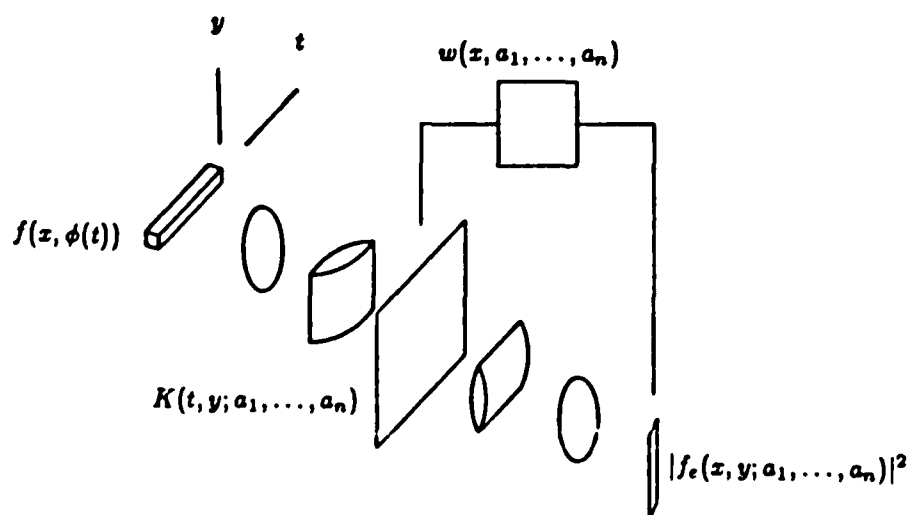


Fig VI.3

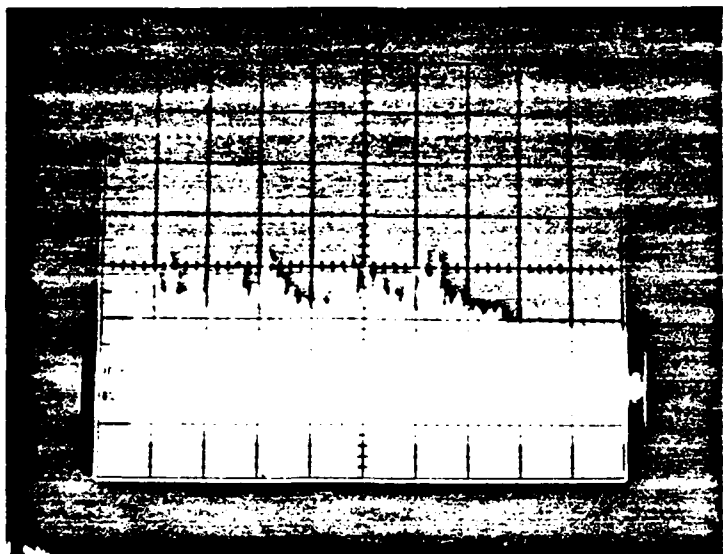


Fig VI.4a

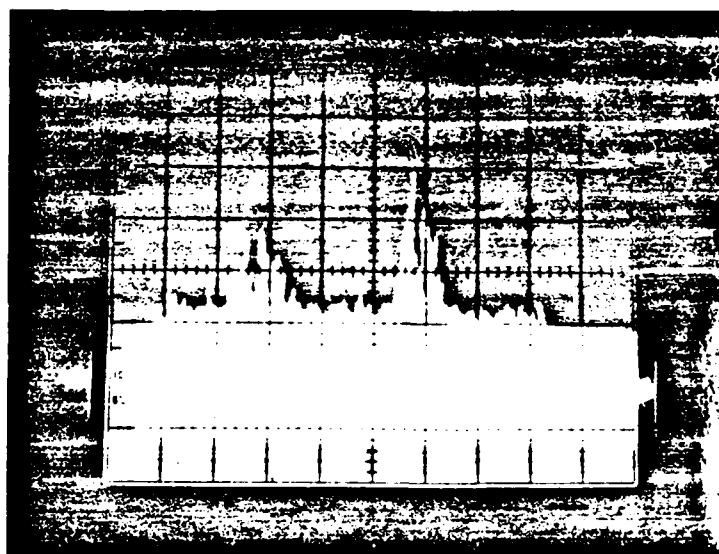


Fig VI.4b

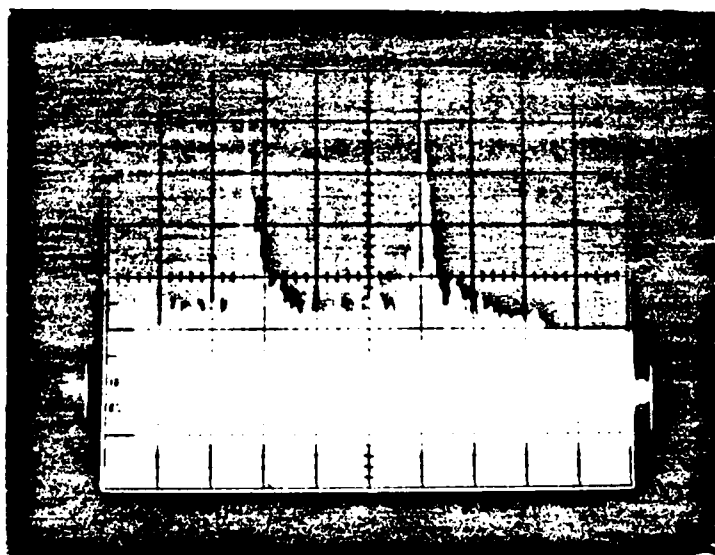


Fig VI.4c

## VII

### CAPACITY OF OPTICAL CORRELATORS

#### VII.1 Introduction

Vander Lugt correlators have been used for a long time in optical pattern recognition[1]. In the typical implementation, shown in figure VII.1, the Fourier transform of an input image is used to read out a hologram containing the Fourier transform of a reference image. This diffracted beam is then inverse Fourier transformed to produce the correlation between the input and reference images on the output plane. Vander Lugt correlators are typically used as pattern recognition systems. Whether or not a peak is present at the output of the correlator determines whether or not the input image is sufficiently close to the stored reference. Recently much work has been done on the use of a Vander Lugt correlator to pattern classification [2][3]. In this case, the correlator distinguishes whether the input is a member of one of two classes with each class being composed of many images. Typically, a reference filter is formed as a linear combination of the images in both classes and the presence or absence of a peak at the correlation plane determines which class the input belongs to. In this paper, we discuss the capacity of the Vander Lugt correlator. This is to say we estimate the maximum number of images that can be stored in the reference filter before the system begins to misclassify images. This capacity has been studied in great detail for systems without shift invariance (e.g. perceptrons). The classic results from pattern recognition about the capacity of a linear discriminant function do not directly apply in this case because the VanderLugt correlator is shift invariant. In this paper, we will discuss the capacity of the system incorporating the shift invariance of the Vander Lugt correlator. We will also discuss the effect on the capacity of binarizing the reference filter and lastly we will demonstrate that by using a volume hologram to record the filter, the capacity of the system is greatly increased, as well as becoming capable of multi-class classification.

#### VII.2 Capacity of Linear Filters

In the most common pattern classification scheme, the inner product is performed between the input image  $\phi(x, y)$  composed of  $N$  pixels and a reference filter  $h(x, y)$ .

$$O = \sum_{y'=1}^{\sqrt{N}} \sum_{x'=1}^{\sqrt{N}} h(x', y') \phi_i(x', y') \quad (VII.1)$$

Comparing the output  $O$  with a pre-set threshold, determines which of the two classes the input belonged to. A standard method of forming the reference filter is as a linear

combination of the images in both classes:

$$h(x, y) = \sum_{i=1}^M w_i \phi_i(x, y) \quad (VII.2)$$

The weights  $w_i$  can be chosen through a variety of training algorithms such as the perceptron learning algorithm. It is a well known result that the capacity of such a system is [4]

$$M = 2N \quad (VII.3)$$

where  $N$  is the number of pixels in each image. In this paper, we will consider the construction of a simpler filter in which the weights are binary.

$$w_i = \begin{cases} 1 & \text{if } \phi_i \in \text{Class I} \\ 0 & \text{if } \phi_i \in \text{Class VII} \end{cases} \quad (VII.4)$$

In other words, the filter is formed by simply summing the images belonging to class 1, while ignoring those in class 2. This is implemented in a Vander Lugt correlator, by multiply exposing the hologram to the images in class 1 while doing nothing for the images in class 2. Classification can then be performed by detecting and thresholding the output at the center of the correlation plane. For the remainder of the paper, we will assume that the images  $\phi(x, y)$  consist of binary  $N$  pixels, each pixel being a bipolar (ie 1 or -1), independent random variable. Under these assumptions, the capacity of the VanderLugt correlator using the peak-only detection scheme can by found be solving the following transcendental equation[5]:

$$M = \frac{N}{4 \log(M^3/N)} \quad (VII.5)$$

As  $N \rightarrow \infty$ , the above expression asymptotically approaches

$$M = \frac{N}{8 \log N} \quad (VII.6)$$

Thus the use of the simpler method for constructing the reference filter, results in a relatively modest loss in capacity by a factor of  $16 \log N$

### VII.3 Capacity of Shift Invariant Filters

Because Vander Lugt correlators are inherently shift invariant it is possible to classify prescribed images and their shifted versions as well. In order to implement a shift invariant classification scheme, detection at the output is done over the entire correlation plane. As a result the detection of a peak anywhere in the output plane determines whether the input is a member of class 1 or a shifted form of a member in class 1. Figure VII.2a shows a cross section through the origin of the digital correlation of an input image with a filter containing only one image. The resulting output shows a single correlation peak and



relatively small sidelobes. When the reference is constructed by adding 3 images (figure VII.2b, the sidelobe structures shows a significant rise in amplitude. However, since only the single correlation peak lies above the threshold, classification of the input image is still performed correctly. However, when the number of reference images is increase to 6 (Fig VII.2c), there are now two peaks which lie above the threshold level. As a result, the system can no longer decide whether the input image is a member of class 1 or a shifted version of a member of class 1. Therefore, we expect that the capacity of the shift invariant system is smaller. For the relatively simple method of filter construction, we can readily derive an analytic capacity for the shift invariant correlator. In the shift invariant case, the Vander Lugt system performs a correlation between one of the input image  $\phi(x,y)$  and the reference filter  $h(x,y)$

$$O(x,y) = \sum_{y'=1}^{\sqrt{N}} \sum_{x'=1}^{\sqrt{N}} h(x',y') \phi_i(x' + x, y' + y). \quad (VII.7)$$

For the case where the filter is constructed by simply summing the images in class 1 (multiple exposure) and assuming the same input statistics for each image, the capacity of the shift invariant Vander Lugt system is given by the solution of the following transcendental equation [5]

$$M = \frac{N}{4 \log(M^3 N)} \quad (VII.8)$$

Asymptotically, the capacity approaches

$$M = \frac{N}{16 \log N} \quad (VII.9)$$

Thus, the capacity is decreased by only a factor of two from that of the non shift invariant system. This result is important since there is to our knowledge no prior estimate for the loss in capacity due to shift invariance. For the case considered here (the filter derived as a simple sum), the loss is very small; a factor of 2. To verify the theoretical capacity of the correlator, 100 computer trials were averaged to determine the capacity for various  $N$ . For each trial, two random vectors were generated to form the initial reference filter. Each image was correlated to determine whether classification was performed correctly. If no error occurred, a new random image was added to the reference filter and correlation with all the image was done. The number of images in the reference was increased until a misclassification occurred. At this point, the capacity was said to be one less than the number of images stored in the reference.

Figure VII.3 shows the capacity of both the peak only and shift invariant systems as a function of the number of pixels,  $N$ , in the image. Experimental simulations show good agreement with theoretical predictions. It is important to note that because the simulations were performed in the regime of small  $N$ , the transcendental equations for the capacity (eqs (VII.5) and (VII.8)) were used to plot the theoretical curves.

## VII.4 Capacity of Binary Filters

As demonstrated above, the capacity of the VanderLugt system can be very large. One potential limitation that might prevent us from actually implementing such a large pattern classification system is the accuracy with which the hologram can record the reference. To get a feel for the susceptibility of the system to nonlinearities and inaccuracies, we considered the capacity of the Vander Lugt correlator when the reference filter has been binarized.

In this case, the reference filter consists of a thresholded version of the filter generated from the multiple exposure algorithm

$$h(x, y) = \text{sgn} \left[ \sum_{i=1}^M w_i \phi_i(x, y) \right] \quad (\text{VII.10})$$

Again, assuming that the input pixels consists of bipolar independent random variables, we find that the capacity of the binary Vander Lugt correlator is asymptotically

$$M = \frac{N}{8\pi \log N} \quad (\text{VII.11})$$

There is only a further  $\pi/2$  reduction in capacity from that of the non binarized shift invariant filter. In figure VII.4, a comparison is made between the linear and a binary filters. In both cases, the input images had 256 pixels and the reference filter contained 3 images. As seen from the figure, the sidelobe level of the binary correlator is significantly larger than that for the linear filter. As a result, as additional images are added to the reference filter, the binary correlator will begin to misclassify sooner. This will correspondingly lead to a lower capacity (theoretical and experimental) for the binary correlator. In figure VII.5, the capacity of both the binarized and nonbinarized filters are plotted as a function of the number of pixels in the image. Again, computer simulations demonstrate a good agreement with theoretical predictions.

## VII.5 Capacity of the Volume VanderLugt Correlator

In this section, we consider the use of a volume hologram to record the reference filters in a Vander Lugt correlator[6]. We expect that because information is recorded in three dimensions as opposed to the two dimensions for plane holograms, the storage capacity of the volume VanderLugt correlator is increased. Let us first consider how a volume Vander Lugt correlator operates (Fig VII.6). Consider the correlation between two point sources. In the recording stage (Fig VII.6a), the point source generates a plane wave which interferes with a reference wave to form a grating which is recorded in the volume hologram. When an input point source at the same position is presented to the correlator (Fig VII.6b), a new plane wave reads out the stored grating. The diffracted plane wave is

then focussed to form the expected correlation peak at the output. If, however, the input point source is shifted in the direction parallel to the plane of incidence (Fig VII.6c), the plane wave that is generated will not be Bragg matched with the grating in the volume hologram. Consequently no diffracted wave will be produced and no correlation spot will be formed. In the direction perpendicular to the plane of incidence, the volume hologram exhibits very little Bragg sensitivity and a correlation can still be read out. As a result, shifts of the input in a direction parallel to plane of incidence will not be recognized, while in the perpendicular direction the correlator remains shift invariant.

For an arbitrary input,  $A(x, y)$  and reference image,  $R(x, y)$ , it can be shown that the output of the volume Vander Lugt correlator is [7]

$$O(x, y) = [A(x, y) * R(x, y)] \text{sinc}(\alpha x) \quad (VII.12)$$

where  $\alpha = T \sin \theta / 2\lambda F$  and  $*$  is the correlation operator.  $T$  is the thickness of the hologram,  $\theta$  is the Bragg angle, and  $F$  is the focal length of the inverse Fourier transform lens. In other words, the output of the correlator consists of the correlation between the input and reference apodized by a sinc function whose width is determined by the thickness of the volume hologram.

To experimentally demonstrate this apodizing effect, the auto correlation of an O was performed using the volume Vander Lugt correlator. Figure VII.7 shows a digitally generated autocorrelation of an O which simulates a standard Vander Lugt correlator with a reference O recorded on a plane hologram. In the volume Vander Lugt correlator, the reference O was recorded on a lithium niobate crystal measuring 25x25x5mm. The reference beam was situated such that the plane of incidence was in the horizontal direction. Figure VII.8a shows the output of the volume Vander Lugt correlator when the input O is positioned at the same plane as the reference O. The output consists of the standard correlation of the two O's multiplied by the horizontal sinc function. When the input O is shifted in the direction parallel to plane of incidence (Fig VII.8b), the correlation shifts and only correlation structure to one side of the peak is presented at the output. The smaller spot lying to the right of the primary horizontal band corresponds to the very strong correlation peak lying in the first sidelobe of the apodizing sinc function. Further shifts of the input as shown in figure VII.8c, merely reads out the correlation structure further from the peak.

The Bragg selectivity in the volume VanderLugt correlator allows one to perform multi-class categorization of the input images[8]. In the recording stage (Fig VII.9a), a set or reference filters is recorded by interfering each with a reference beam separated by the angular bandwidth of the volume hologram. When an input image is presented to the volume Vander Lugt correlator (Fig VII.9b), a set of correlations is performed simultaneously and presented spatially distributed at the output. The Bragg selectivity of the hologram guarantees that the correlation bands will not interfere with each other. As a result, by detecting which band the correlation peak appear, determines which of many classes the input image belongs to.

We can consider each correlation band as a separate output channel performing a simple pattern classification task independent of the other channels. By assuming the

same input statistics for the images in each class, the capacity of each output channel can be analytically derived. In this case, the maximum number of images that can be stored was found to be equal to that of the standard VanderLugt correlator (eq VII.5). Asymptotically, the capacity of each channel approaches

$$M' = \frac{N}{16 \log N} \quad N \rightarrow \infty \quad (VII.13)$$

The number of output channels,  $K$ , that can be stored in the volume hologram is

$$K = \frac{TL \sin \theta}{\lambda F} \quad (1 \leq K \leq N) \quad (VII.14)$$

where  $L$  is the actual dimension of the output detector array in the direction parallel to the plane of incidence. Hence the total capacity of the system is

$$M_{Total} = \frac{KN}{16 \log N} \quad (N \rightarrow \infty; 1 \leq K \leq N) \quad (VII.15)$$

Thus the effect of the using a volume hologram is that the capacity is increased by the number of output channels the hologram can support and one to perform multi-class classification. However, one drawback is the partial loss of shift invariance in one direction that results from the use of a volume hologram.

## VII.6 Conclusion

In conclusion, we have demonstrated that the capacity of a Vander Lugt correlator without shift invariance is  $N/8 \log N$  for the simple additive filter. By incorporating the shift invariance inherent in an optical correlator, the capacity is only decreased by a factor 2. Furthermore, by binarizing the reference filter, there is a further loss by a factor of  $\pi/2$ . However, by utilizing a volume hologram to record the reference filter, the capacity of the correlator is increased by a factor that can be as high as  $N$  with a proportional loss in shift invariance.

## References

- [1] A. VanderLugt, *IEEE Trans. Inf. Th.*, **IT-10** 139 (1964)
- [2] D. Casasent *Appl. Opt.*, **23** 1620 (1984)
- [3] A. Lohmann and C. Thum *JOSA*, **23** 1503 (1984)
- [4] F. Rossblatt *Principles of Neurodynamics: Perceptrons and the Theory of Brain Mechanisms* (Spartan Books, Washington D.C. 1961)

- [5] J. Yu, F. Mok, and D. Psaltis *submitted to Applied Optics*
- [6] S.I. Stepanov and V. D. Gural'nik *Sov. Tech. Phys. Lett.* ,8 49 (1982)
- [7] J. Yu and D. Psaltis *To be published*
- [8] C. Guest and C. Gaylord *Appl. Opt.*,19 1201 (1983)

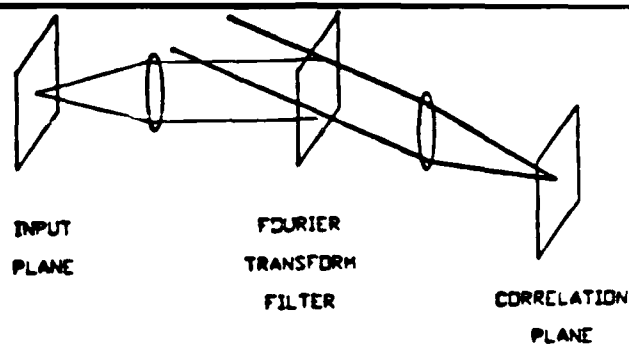


Fig VII.1 Vander Lugt correlator.

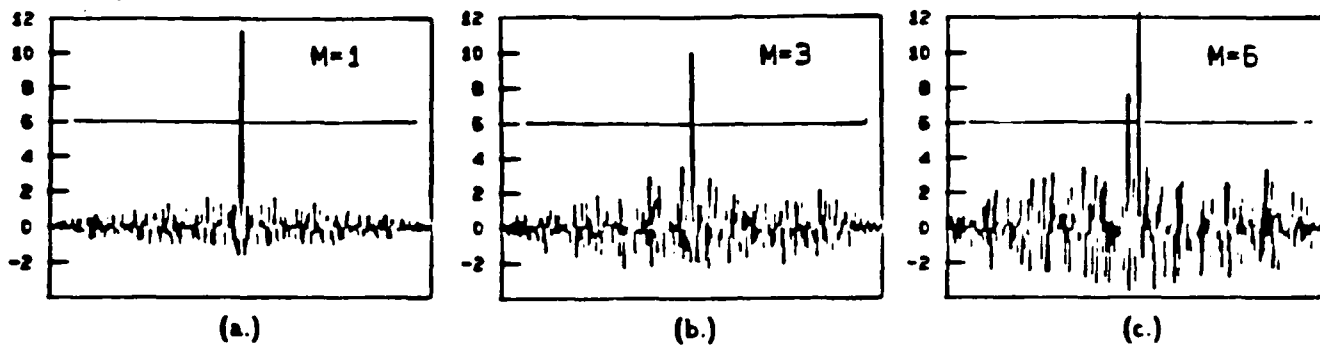


Fig VII.2 Digital correlations of a shift invariant filter.

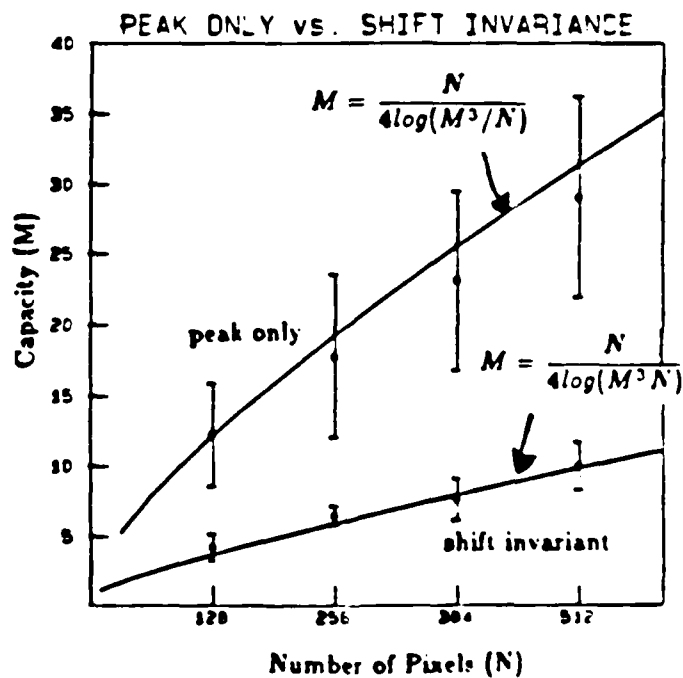


Fig VII.3 Capacity curves of the peak only and shift invariant filters.

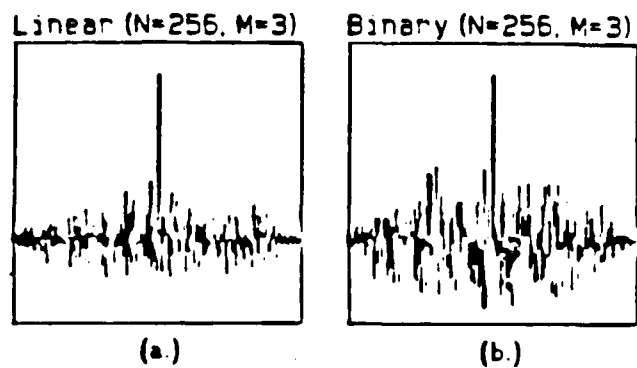


Fig VII.4 Digital correlations of linear and binary filters.

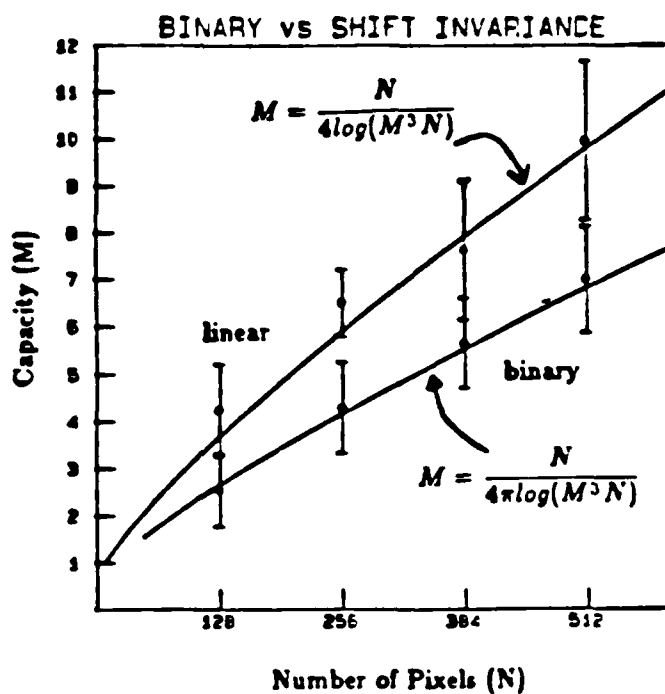


Fig VII.5 Capacity curves of shift invariant and binary filters.

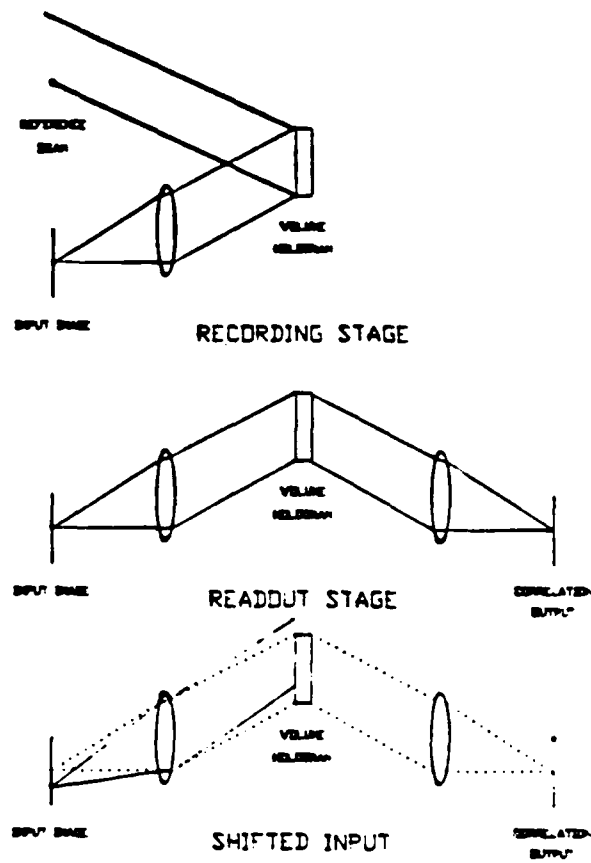


Fig VII.6 Recording and readout of a volume hologram.

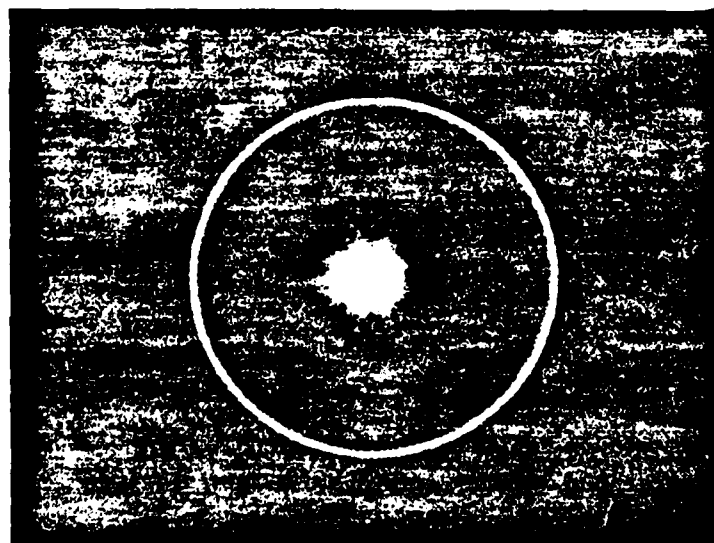


Fig VII.7 Digal autocorrelation of an "O".



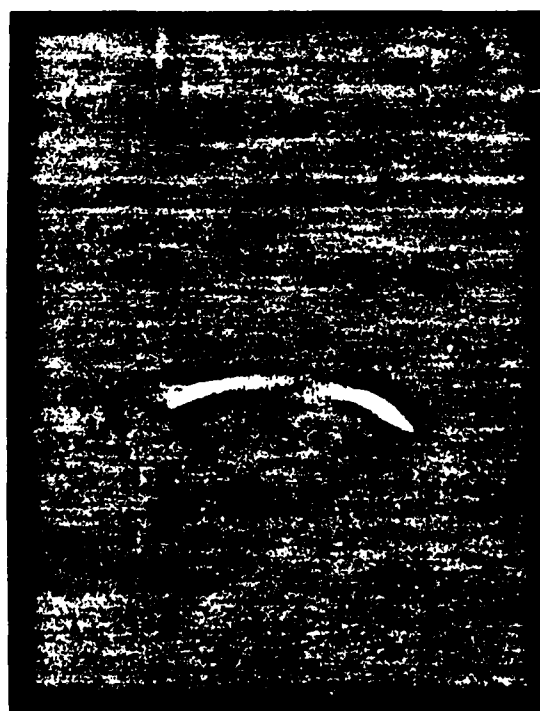
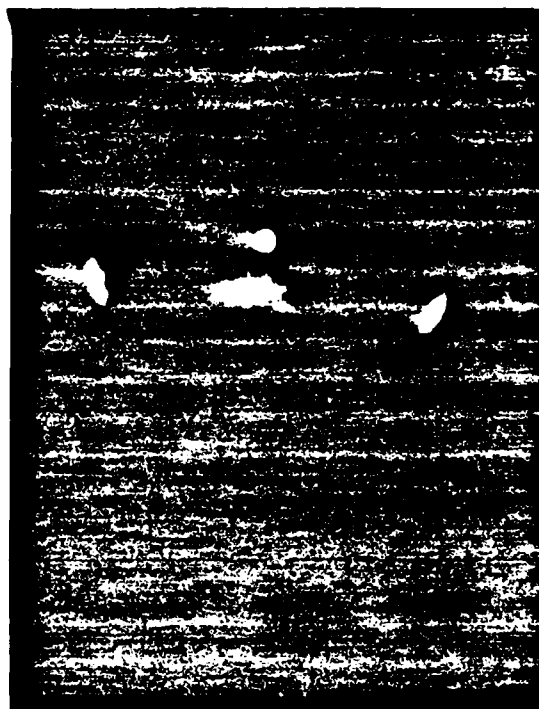
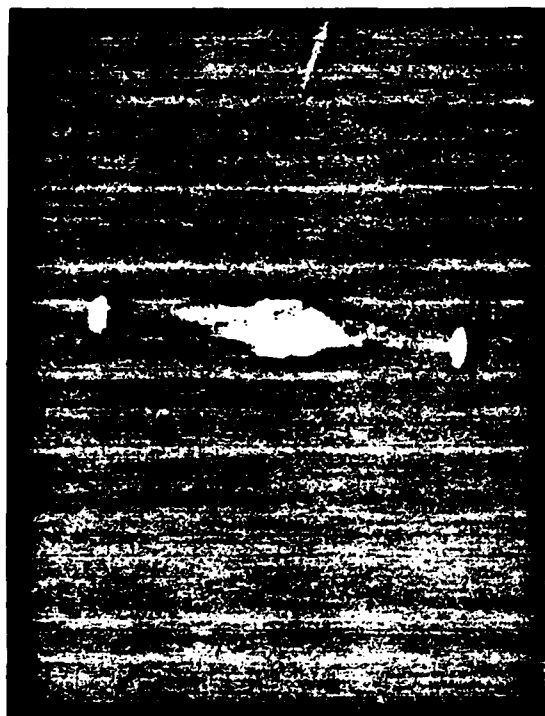
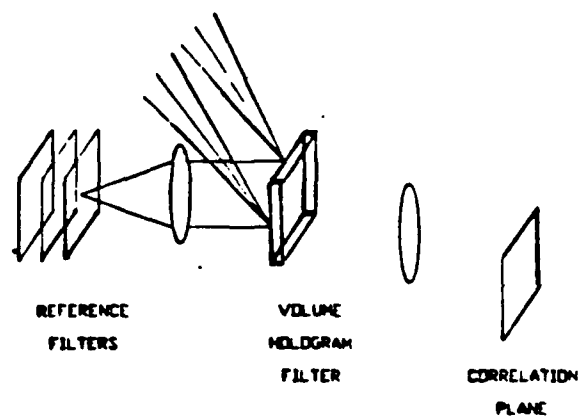
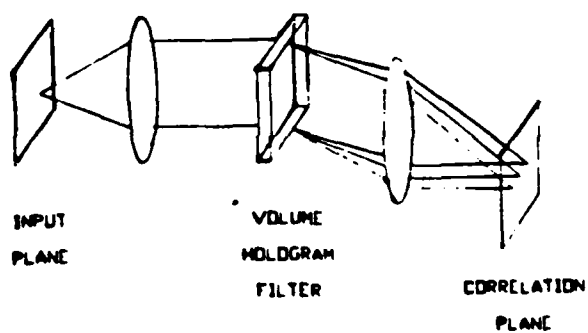


Fig VII.8 . Experimental outputs of volume Vander Lugt correlator



(a.)



(b.)

Fig VII.9 Recording and readout stage of the multi-class. categorization volume Vander Lugt correlator.

## VIII

### PHOTOREFRACTIVE INTEGRATED OPTICAL VECTOR MATRIX MULTIPLIER

#### VIII.1 Introduction

Vector matrix multiplication is central to a wide range of signal processing systems, including neural networks, large scale interconnection networks, and linear transformations. Bulk optical implementations of vector matrix multiplication are well developed and quite successful [10]. The classical optical vector matrix multiplier uses a cylindrical lens to expand a one dimensional array of light sources across a two dimensional spatial light modulator on which the matrix is recorded. A second, orthogonal, cylindrical lens focuses light from the SLM onto an array of detectors. Each element of this array receives light from each element in the input vector, modulated by the appropriate matrix element. This method of implementing vector matrix multiplication has been applied in a number of signal processing architectures.

Despite the success of these devices, the implementation of vector matrix multipliers in integrated optics offers certain advantages which are difficult to achieve in bulk. Integrated devices are typically much smaller and lighter than their bulk counterparts. Fabrication of a large number of identical integrated devices is relatively easy due to the advanced state of photolithography. In addition, integration leaves the dimension out of the integrated plane free for optical control of the matrix interconnecting vectors in the guided plane. In bulk devices dynamic control of this matrix may be relatively difficult. In this paper we propose implementing a vector matrix multiplier in integrated optics using photorefractive holography in the volume of the waveguide. A schematic architecture for this device is shown in figure VIII.1. A vector is input through a channel waveguide array integrated on a suitable substrate. Light from these channels is collimated by an integrated lens [7] before reading out a matrix of holographic gratings formed in a slab waveguiding region. The diffracted vector is refocused into an output channel waveguide array. This architecture performs vector matrix multiplication with as many degrees of freedom as the bulk architecture by utilizing the Bragg selectivity of volume holograms to substitute for one dimension of the bulk spatial light modulator.

#### VIII.2 Matrix Implementation via Integrated Volume Holograms

Vector matrix multiplication using diffraction gratings may be described via coupled wave equations in Fourier space. The electric field vector  $\vec{E}(\vec{r})$  may be described at any plane along the optical axis of the system in terms of a complete set of guided and unguided modes of the slab waveguide. Letting  $A_\nu(\vec{k})$  represent the component of  $\vec{E}(\vec{r})$  in the mode

$\nu$  at spatial frequency  $\vec{k}$  we may express  $\vec{E}(\vec{r})$  as

$$\vec{E}(\vec{r}) = \int \int \int \sum_{\nu} A_{\nu}(\vec{k}) \vec{\mathcal{E}}_{\nu}(\vec{k}, \vec{r}) d\vec{k} \quad (\text{VIII.1})$$

$\vec{\mathcal{E}}_{\nu}(\vec{k}, \vec{r})$  is the field distribution for the mode  $\nu$  at spatial frequency  $\vec{k}$ . The effect on  $\vec{E}(\vec{r})$  of the hologram recorded in the volume of the slab may be described by substituting (VIII.1) into the Helmholtz equation and applying the slowly varying envelope approximation. From this approach we obtain

$$\int \int \int \sum_{\nu} \frac{\partial A_{\nu}(\vec{k})}{\partial z} j k_{\nu z} \frac{\partial \vec{\mathcal{E}}_{\nu}(\vec{k}, \vec{r})}{\partial z} d\vec{k} = \sum_{\vec{k}_g} \Delta k^2(\vec{K}_g, \vec{r}) \int \int \int \sum_{\nu} A_{\nu}(\vec{k}) \vec{\mathcal{E}}_{\nu}(\vec{k}, \vec{r}) d\vec{k} \quad (\text{VIII.2})$$

where  $\Delta k^2(\vec{K}_g, \vec{r})$  is proportional to the holographic perturbation to the dielectric constant at spatial frequency  $\vec{K}_g$ . By applying the orthogonality condition

$$\int \int \int \vec{\mathcal{E}}_{\nu}(\vec{k}, \vec{r}) \cdot \vec{\mathcal{E}}_{\nu'}^*(\vec{k}', \vec{r}) d\vec{r} = \delta_{\nu\nu'} \delta(\vec{k} - \vec{k}') \quad (\text{VIII.3})$$

Equation (VIII.2) may be reduced to

$$\frac{\partial A_{\nu}(\vec{k}_1)}{\partial z} = -j \sum_{\nu} \sum_{\vec{K}_g} \kappa_{\nu \vec{K}_g} A_{\nu}(\vec{k}_2) \quad (\text{VIII.4})$$

where

$$\vec{k}_1 - \vec{k}_2 = \vec{K}_g \quad (\text{VIII.5})$$

and

$$\kappa_{\nu \vec{K}_g} = \frac{1}{k_{\nu z}} \int \int \int \Delta k^2(\vec{K}_g, \vec{r}) \vec{\mathcal{E}}_{\nu}(\vec{k}_p - \vec{K}_g, \vec{r}) \cdot \vec{\mathcal{E}}_{\nu_p}^*(\vec{k}_p, \vec{r}) d\vec{r} \quad (\text{VIII.6})$$

In deriving equation (VIII.4) we have ignored the finite nature of the hologram. Equation (VIII.4) may be expressed

$$\frac{\partial \vec{A}}{\partial z} = \vec{H} \vec{A} \quad (\text{VIII.7})$$

Each  $A_{\nu}(\vec{k}_1)$  with  $\vec{k}_1$  satisfying equation (VIII.5) forms a component of  $\vec{A}$ . The components  $\vec{H}$  are given by

$$\vec{H}(\vec{k}_1, \vec{k}_2) = \kappa_{\nu(\vec{k}_1 - \vec{k}_2)} \quad (\text{VIII.8})$$

The solution to equation (VIII.7) is  $\vec{A} = \exp(\vec{H}z) \vec{A}_0$ . If all of the eigenvalues of  $\vec{H}$  satisfy  $|\lambda|L \ll 1$  where  $L$  is the length of the holographic interaction region then we find that

$$\vec{A} = (I + \vec{H}L) \vec{A}_0 \quad (\text{VIII.9})$$

Thus a Fourier hologram written in the slab waveguide may perform a vector matrix multiplication taking each Fourier component of the incident field to each component of the output field. Under suitable conditions of mutual incoherence of the stored gratings and the fields vector matrix multiplication may also be shown to occur between the incident and output intensities.

In the architecture of figure VIII.1 each Fourier component of the field incident on the the volume hologram corresponds to the field in a single channel of the input waveguide array. Similarly, each Fourier component of the field diffracted from the hologram corresponds to the field in a single channel of the output waveguide array. Since the hologram performs vector matrix multiplication between the incident and diffracted fields, the system as a whole performs vector matrix multiplication between the vector of field amplitudes in each input channel and the matrix of Fourier grating amplitudes in the volume hologram. Each component of the output vector is represented by a field amplitude in an output channel. Crosstalk, i.e. diffraction of one input channel by a grating corresponding to another input channel, and second order diffraction, are avoided by the Bragg wavevector matching condition given in equation (VIII.5). As mentioned above,  $\vec{K}_g$  is the grating wavevector.  $\vec{k}_1$  and  $\vec{k}_2$  are constrained to lie on the normal surface. Since in an integrated geometry  $\vec{k}_1$  and  $\vec{k}_2$  are further constrained to the integrated plane, wavevectors satisfying the Bragg condition for a given  $\vec{K}_g$  are unique for an integrated hologram. Figure VIII.2 shows graphically the relationship between the input vector, the output vector and the interconnection matrix. Each component of the input vector corresponds to a wavevector with an end point on the normal surface at the lower right. Each component of the output wavevector corresponds to a wavevector with and endpoint on the normal surface at the upper right. Each component of the interconnection matrix corresponds to a vector joining the endpoints of an input component and an output component on the normal surface. As long as each input and output wavevector differs by more than a vector of magnitude  $\frac{1}{L}$  from the nearest neighboring wavevector, the input and the output vectors may be fully interconnected without crosstalk.

The requirement that the components of the input and output vectors be separated by  $\frac{1}{L}$  arises from ambiguity in the grating wavevectors due to the finite volume of the hologram. This ambiguity limits the number,  $S$ , of independent interconnections which can be stored in a bulk volume hologram is limited to the number of resolvable spots in the volume, i.e.

$$S \approx \frac{V}{\lambda^3} \quad (VIII.10)$$

where  $V$  is the volume of the recording medium and  $\lambda$  is the wavelength of the readout light. Psaltis *et.al.*<sup>11</sup> have shown that this limitation on the number of interconnections between two image planes limits the spots used for complete and independent interconnection of two planes to fractal grids of dimension  $\frac{3}{2}$ . In the case of the integrated volume holograms limitations of this sort on the input and output vectors due not arise. It can be shown that the number,  $S'$ , of interconnections which can be stored in an integrated hologram is

limited by ambiguity in Fourier space to

$$S' = \frac{A}{\lambda^2} \quad (\text{VIII.11})$$

where  $A$  is the area of the interaction region. There are of course further limits on  $S'$  arising from the finite bandwidth of the photorefractive response and the finite apertures of the optical system, but these limitations contribute only a scaling factor independent of  $A$  and  $\lambda$ . It is interesting to note that the integrated volume holographic vector matrix multiplier implements linear transformations with the same number of degrees of freedom as the bulk device using a two dimensional mask.

### VIII.3 Recording the Matrix

We now turn to the question of how the hologram representing  $\bar{H}$  may be recorded. Photorefractive effects offer a particularly simple and flexible approach. The photorefractive effect is a mechanism by which volume gratings may be created in waveguiding crystals such as  $\text{LiNbO}_3$ , GaAs and  $\text{SBN}^{2,3,4,5}$ . Photorefractive gratings arise from the electrooptical modulation of the refractive index by the space charge field arising from the inhomogeneous charge distribution induced by the intensity distribution of the write beams. The amplitude of the photorefractive perturbation is proportional to the modulation depth,  $M$ , of the optical intensity. The diffraction efficiency of the resulting hologram is proportional to the square of the perturbation, i.e. to  $M^2$ , and to the length of the interaction region. While the amplitude of the index perturbation which may be achieved in this way is small, the diffraction efficiency of photorefractive holograms is often large because of the volume nature of the perturbation region. The advantages of photorefractive gratings in the application described here are that they can be written with high resolution in real time with no substrate preparation or development steps, that they are erasable and modifiable, that writing photorefractive gratings does not add a bias to the mean index of refraction, and that the high sensitivity of the photorefractive effect to changes in wavelength allows the gratings to be written optically with short wavelengths and readout at longer wavelengths beyond the threshold for writing.

In order to have full independent control of the interconnection matrix it is necessary to separate the process of writing the hologram from the read-out process. This may be done by utilizing the rotational degeneracy of volume holograms. Since the right hand side of equation (VIII.5) is unchanged by rotations about  $\vec{K}_g$ , an infinite set of coupled pairs  $\vec{k}_1$  and  $\vec{k}_2$  may be generated by rotating the normal surface about the grating wavevector. This degeneracy in the Bragg condition allows us to write gratings in integrated waveguides with unguided light (radiation modes) which may be readout by guided beams. If we include in our analysis a change of the magnitudes of the optical wavevectors due the transition from guided to unguided beams and a difference in the wavelengths of the write and read beams, then it may be shown that guided beams at wavelengths beyond the threshold of the photorefractive response may be diffracted by holograms written by

unguided light at a shorter wavelength. This arrangement allows us to take advantage of the long interaction lengths, high beam intensities, and compact construction of integrated devices while avoiding optical damage and photorefractive scattering due to the readout beams. Since we have all the degrees of freedom of bulk optics in positioning the write beams, we will be able to describe below a simple method for writing with a single exposure a hologram which completely and independently interconnects every resolvable spot at the input to the waveguide with every resolvable spot at the output.

Vector matrix multiplication is performed in the architecture we are proposing by using  $n_1 n_2$  gratings to map  $n_1$  input frequencies to  $n_2$  output frequencies. Each grating may be associated with a pair of radiation modes by rotating the input and output beams about the grating vector. Figure VIII.3(a) is a wave matching diagram which graphically shows the Bragg matching condition as a requirement that the end points on the normal surface of coupled optical wavevectors be joined by the grating wavevector. Figure VIII.3(b) shows a pair of unguided optical beams which may be associated with this wavevector. Figure VIII.3(c) shows a second pair of optical beams generated upon rotation about a second wavevector coupling one of the original guided beams with a third guided beam. As can be seen in figure VIII.3(d) the unguided wavevectors into which the guided beam is rotated are different for the two different grating wavevectors. This simple graphical demonstration points out a problem which can be shown to hold in general in the architecture we are proposing, which is that as many as  $2n_1 n_2$  distinct radiation modes must be available to write the  $n_1 n_2$  gratings coupling  $n_1 + n_2$  guided modes. One means of presenting all these radiation modes simultaneously in each write cycle might be to use a second volume hologram to store the  $2n_1 n_2$  beams.

The amplitude of a photorefractive index perturbation is proportional to the modulation depth of the writing beams. For the case of writing with  $n_1 n_2$  beams of approximately equal intensities, the modulation depth of each grating will be proportional to  $(n_1 n_2)^{-1}$ . The modulation depths of the individual gratings are also proportional to  $(n_1 n_2)^{-1}$  for sequential writing if the asymmetry between the erase and write times is not large. By using the architecture of figure VIII.4 it is possible to reduce this factor to  $(\sqrt{n_1 n_2})^{-1}$  by writing all the gratings with a single reference beam. In this geometry the modulation depth of the  $(ij)^{th}$  grating is

$$M_{ij} = \frac{\sqrt{I_{ij} I_R}}{I_R + N \langle I_{ij} \rangle} \quad (VIII.12)$$

Where  $I_{ij}$  and  $I_R$  are the intensities of the  $(ij)^{th}$  write beam and of the reference respectively.  $\langle I_{ij} \rangle$  is the mean value of the write beam intensities. The expected value of  $M_{ij}$  has a maxima of  $(2\sqrt{(n_1 n_2)})^{-1}$  when  $\langle I_{ij} \rangle = \frac{I_R}{\sqrt{(n_1 n_2)}}$ .

A problem with the architecture shown in figure VIII.4 arises from the fact that it is not possible to write an interconnection matrix in the plane using a single reference while still satisfying the Bragg condition for each interconnection. This problem may be overcome by taking advantage of the fact that the interaction region of the hologram is very thin out of the plane of the waveguide. If the modes coupled by a given grating are well guided then the coupling efficiency is insensitive to Bragg mismatch out of the

waveguiding plane if the phase of the grating remains constant within the coupling region. This fact allows us to have a Bragg mismatch out of the plane of the waveguide. This concept is illustrated in figure VIII.5. In figure VIII.5(a) we show a set of fringes for a grating written with  $\vec{K}_g$  confined to the surface of the waveguide. Note that the phase of the grating is constant along the vertical direction. In figure VIII.5(b)  $\vec{K}_g$  is not confined to the waveguiding plane and the phase of the grating is not constant along the vertical direction. However, since the interaction region for well confined modes includes only the waveguide itself, high diffraction efficiencies may be achieved between guided modes if the phase of the grating is constant in the vertical direction in a region approximately limited to the waveguide itself. This condition may be expressed in the form

$$(\vec{K}_g)_x d \ll 1 \quad (VIII.13)$$

where  $d$  is the thickness of the interaction region. Since  $d$  may be very small for a optical waveguide, we find that our architecture will tolerate a fairly large Bragg mismatch out of the waveguiding plane. This allows us to write the full interconnection matrix with a single reference as shown in figure VIII.4.

It is still necessary to fabricate the mask T in such a way that Bragg matching in the plane of the waveguide is achieved for each interconnection. The Fourier lens  $L_1$  is aligned so that a pixel on its optical axis is collimated such that

$$\kappa_{00x} = K_x; \kappa_{00y} = K_y = 0; \kappa_{00z} = -K_z \quad (VIII.14)$$

where  $\vec{\kappa}_{00}$  and  $\vec{K}$  are the wavevectors of the collimated beam and of the reference respectively. The requirement that the grating produced by the reference and the light from pixel  $ij$  be the grating that connects the  $i^{th}$  input channel and the  $j^{th}$  output may be expressed  $\vec{\kappa}_{ij} = \vec{K} - \vec{k}_{ij}$ . Since  $\vec{k}_{ij}$  has no component out of the plane of the waveguide, the  $\hat{e}_x$  component of this equation is satisfied if, as we saw above,

$$(\vec{K} - \vec{\kappa}_{ij})_x \ll \frac{1}{d} \quad (VIII.15)$$

In the paraxial approximation this requirement becomes  $\frac{\rho}{F} \ll \sqrt{\frac{\lambda}{d}}$  where  $\rho$  is the greatest distance from the optical axis of a pixel on T. Having satisfied this constraint, the  $\hat{e}_y$  and  $\hat{e}_z$  components of the phase matching equation may be satisfied by properly placing the pixels on the mask. An example of a suitable mask for a four by four device with a 400  $\mu m$  separation between channels is shown in figure VIII.6 We have assumed a lens of focal length 25cm between the mask and the waveguide and integrated lenses of focal length 1cm. The angle between the writing beams is assumed to be three degrees.

#### VIII.4 Experimental Results and Discussion

We have written photorefractive gratings in single mode titanium indiffused slab waveguides on nominally pure y cut LiNbO<sub>3</sub>. The gratings were written using unguided



light at 488 nm from an Ar<sup>+</sup> laser. The red HeNe line was used for readout. The grating wave vectors were nearly parallel to the c axis to make use of the  $r_{33}$  electrooptic coefficient and the photovoltaic field. Optical propagation was along  $\hat{e}_y$  for the write beams and along  $\hat{e}_x$  for the guided read beams. The effective index for the guided HeNe mode was 2.248, while the extraordinary index of the substrate at 488 nm is about 2.6. Thus, between the write and read beams there was an expansion of the angle between the beams Bragg matched to a particular grating by a factor of about 1.5. Small angles were used because our waveguide was not guiding along  $\hat{e}_z$ . We have obtained coupling efficiencies of up to 4.5% between guided modes of interaction lengths of about 1 cm. We have also been successful at coupling a single guided mode into two two diffracted modes, though we have not yet implemented the mask scheme described above to achieve multibeam coupling with high efficiency. Photographs of zero and first order spots diffracted from the end of the waveguide in the one and two grating cases are shown in figure VIII.7. In two grating case both gratings were written with a single reference beam. Both are slightly Bragg mismatched for readout.

Various problems arise in the implementation of the architecture we have proposed. Two specific problems concern the depletion of the pump beams and the implementation of the matrix in grating amplitudes. Since the interaction region for integrated volume holograms may be very long, the coupling efficiency of these holograms may be quite high. In the depleted pumps regime the accuracy to which the device represents a true vector matrix multiplier will be compromised. The extent to which this is a problem depends upon the application envisioned. Since the amplitude of each grating is linear in modulation depth, which is a nonlinear function of the total background intensity, it is only possible in a statistical sense to associate a given grating amplitude with a specific transmittance in the writing mask. For small scale applications both of these problems may be surmounted by considering the expected signals from each channel. For larger scale applications, the application must be tolerant to these nonlinearities. Optical neural computers<sup>8</sup> are one such application.

A third problem arises from the effect of titanium on the photorefractive properties of LiNbO<sub>3</sub>. Glass *et. al.* found that Ti doping increases the dark conductivity of LiNbO<sub>3</sub>, thereby reducing the grating storage time<sup>5</sup>. In our waveguides we found grating lifetimes of several days under continuous guided readout with about 50  $\mu W$ . One method of increasing this lifetime might be to use proton exchanged waveguides<sup>9</sup>. In applications where storage time is not a concern, GaAs or SBN might be used as a substrate.

### VIII.5 conclusion

In conclusion, we have proposed an architecture using coupling from a set of input channel waveguides to a set of output channels using multiwave photorefractive mixing in a slab waveguide to implement vector matrix multiplication. We have demonstrated the feasibility of out of plane photorefractive deflection of guided beams. By using out of plane beams to address the nonlinearity we are able to combine the holographic capabilities of

photorefractive crystals with the capabilities of integrated optics.

### References

- [1] C.S. Tsai, *IEEE Trans. Circuits and Systems* CAS-26,1074(1979)
- [2] R.P. Kenan, D.W. Vahey, N.F. Hartman, V.E. Wood, C.M. Verber, *Opt. Eng.* 15,12(1976)
- [3] O.V. Kandidova, V.V. Lemanov, B.V. Sukharev, *Sov. Phys. Tech. Phys.* 29,1019 (1984)
- [4] W.S. Goruk, P.J. Vella, R. Normandin, G.I. Stegeman, *Appl. Opt.* 20,4024(1981)
- [5] A.M. Glass, I.P. Kaminow, A.A. Ballman, D.H. Olson, *Appl. Opt.* 19,276(1980)
- [6] N.V. Kukhtarev, V.B. Markov, S.G. Odulov, M.S. Soskin V.L. Vinetskii, *Ferroelectrics* 22,949(1979)
- [7] D.Y. Zang, C.S. Tsai, *Appl. Opt.* 25,2264,(1986)
- [8] D. Psaltis and N. Farhat, *Opt. Lett.* 10,98(1985)
- [9] J.L. Jackel, C.E. Rice, J.J. Veselka, *Appl. Phys. Lett.* 41,607(1982)
- [10] J. Goodman, A.R. Dias, and I.M. Woody, *Opt. Lett.* 2,1(1978)
- [11] D. Psaltis, J. Yu, X. G. Gu, and H. Lee, Second Topical Meeting on Optical Computing, Incline Village, Nevada, March 16-18,1987

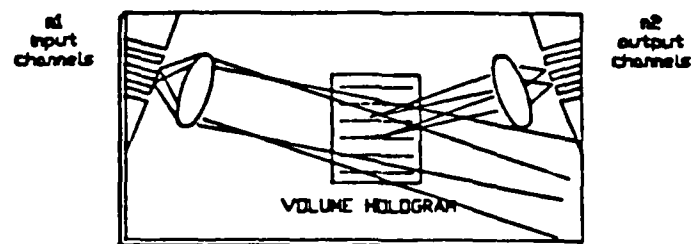


Fig VIII.1 Integrated optical matrix vector architecture.

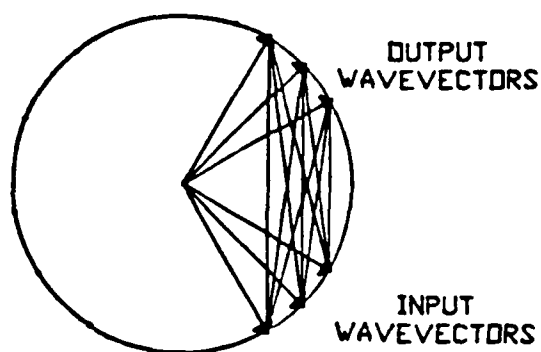


Fig VIII.2 Wavematching between the input, the output, and the interconnection matrix.

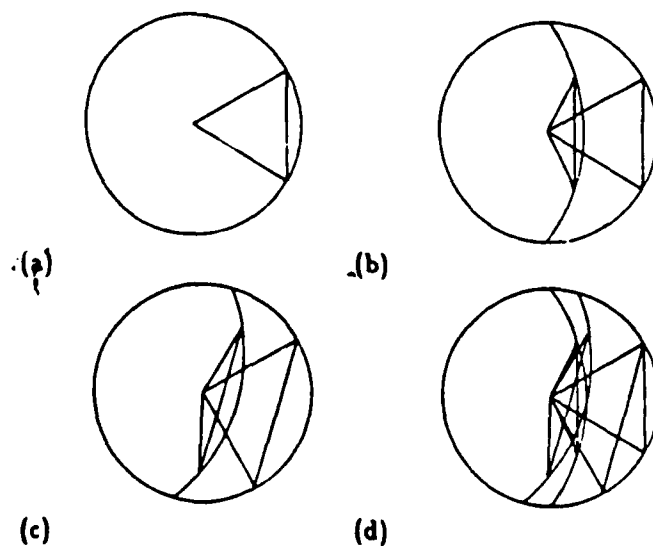


Fig VIII.3 Rotational degeneracies of Bragg matched holograms.

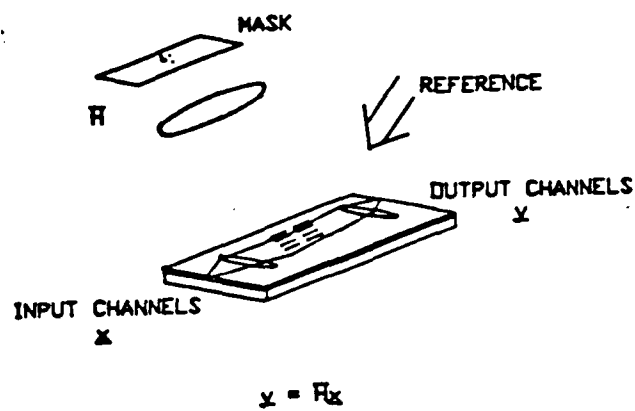


Fig VIII.4 Recording with unguided light and a single reference.

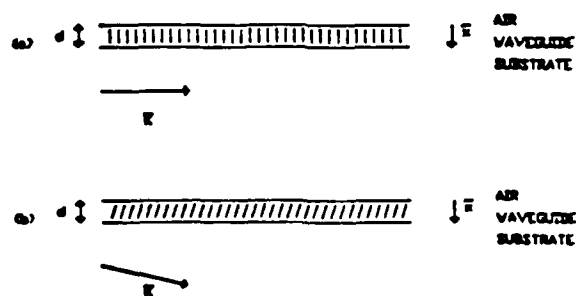


Fig VIII.5 Bragg mismatch out of the guiding plane.

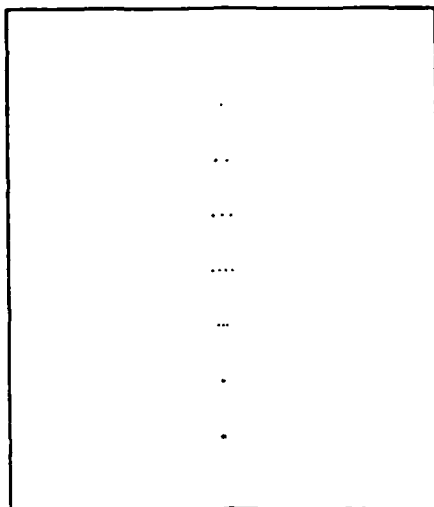


Fig VIII.6 Mask for recording a 4 x 4 matrix.

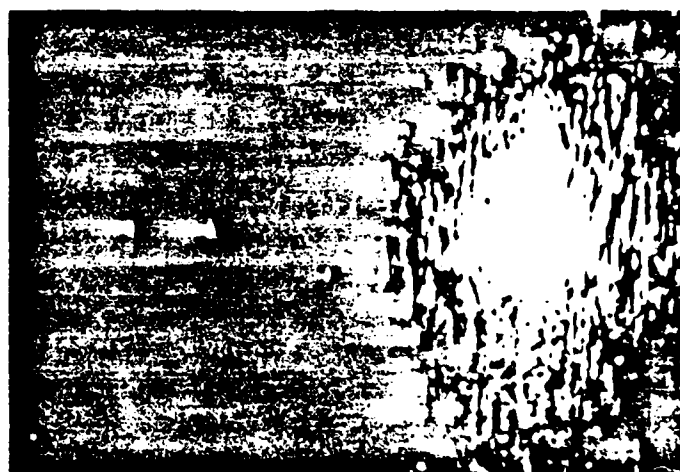


Fig VIII.7 Diffracted and undiffracted beams in  $\text{LiNbO}_3$   
 One grating. Two gratings.